Draft version October 9, 2002
Preprint typeset using LATEX style emulateapj v. 26/01/00

THEORETICAL SPECTRA AND ATMOSPHERES OF EXTRASOLAR GIANT PLANETS

David Sudarsky[1], Adam Burrows[1], & Ivan Hubeny[2,3]

Draft version October 9, 2002

ABSTRACT

We present a comprehensive theory of the spectra and atmospheres of irradiated extrasolar giant planets. We explore the dependences on stellar type, orbital distance, cloud characteristics, planet mass, and surface gravity. Phase-averaged spectra for specific known extrasolar giant planets that span a wide range of the relevant parameters are calculated, plotted, and discussed. The connection between atmospheric composition and emergent spectrum is explored in detail. Furthermore, we calculate the effect of stellar insolation on brown dwarfs. We review a variety of representative observational techniques and programs for their potential for direct detection, in light of our theoretical expectations, and we calculate planet-to-star flux ratios as a function of wavelength. Our results suggest which spectral features are most diagnostic of giant planet atmospheres and reveal the best bands in which to image planets of whatever physical and orbital characteristics.

Subject headings: planetary systems—binaries: general—planets and satellites: general—stars: low-mass, brown dwarfs—radiative transfer—molecular processes—infrared: stars

1. INTRODUCTION

In the last seven years, more than 100 extrasolar giant planets (EGPs) have been discovered by precision radial-velocity measurements of the telltale wobble of their central stars[4], and their discovery constitutes a major turning point in both planetary science and astronomy. The unanticipated variety of these extrasolar planetary systems (most completely unlike our own) is drawing an increasing fraction of the world's astronomers into the technological, theoretical, and observational programs designed to study and understand them in more detail.

Because the indirect Doppler technique does not reveal the inclination (i) of the planet's orbit, only the minimum or projected mass of the planet ($M_p\sin(i)$) can be inferred. Currently, the $M_p\sin(i)$s for the known EGPs range from less than half a Saturn mass to over 10 Jupiter masses (M_J). One object, HD 209458b, transits its primary, revealing its edge-on orbit and, hence, its mass of $0.69M_J$. However, with the majority of EGPs we are not so fortunate and accurate astrometric measurements will be needed to obtain orbital inclinations.

The orbital distances (semi-major axes) of the known EGPs cover the wide range from 0.038 AU to ~5.5 AU, a range that is expected to expand outward as detection techniques and instrumentation improve. Orbital eccentricities are near zero for close-in objects, as expected due to the tidal dissipation of their orbits. But for EGPs at larger orbital distances, eccentricities are spread from ~0.03 to ~0.9. The most eccentric known EGP, HD 80606b, has an eccentricity of 0.927.

The central stars around which giant planets have been found range from main sequence spectral type F7 to M4, but due to the biased nature of the radial-velocity searches most are of spectral type G or K. The metallicities of the primaries vary significantly, with [Fe/H] ranging from ~ -0.6 to +0.4; the majority are above solar metallicity ([Fe/H] = 0).

Although the radial-velocity programs have launched the modern study of EGPs, it is only by making direct measurements of the planet's spectrum that its physical characteristics can be fully characterized. Hence, the next stage after the initial ground-breaking Doppler campaigns in the study of EGPs will be their direct imaging and spectroscopic measurement. This paper has been written to support this burgeoning effort. The theoretical modeling of EGP atmospheres is important for at least two major reasons. First, since the emergent spectra of EGPs are determined by the chemistry and physics of their outer atmospheres, when direct detection of EGPs is achieved and spectra are obtained, theoretical models will be essential in the interpretation of the data and in the extraction of essential physical information such as radius, gravity, temperature, and composition. Second—and this is the more pressing of the two—theoretical spectral models are important in guiding current and upcoming direct EGP searches. Observers need to know which regions of the spectrum provide the greatest chance for detection, while avoiding those regions in which attempts are likely to be futile.

A host of exciting ground-based and space-based missions for the detection, characterization, and imaging of EGPs are well underway or under serious consideration (§8). Ground-based interferometric endeavors include astrometry with the VLT Interferometer (Paresce 2001), astrometry and differential phase methods with the Keck Interferometer (van Belle & Vasisht 1998; Akeson & Swain 2000), and nulling interferometry with the LBT Interferometer (Hinz 2001). Ground-based

[1]Department of Astronomy and Steward Observatory, The University of Arizona, Tucson, AZ 85721
[2]NASA Goddard Space Flight Center, Greenbelt, MD 20771
[3]NOAO, Tucson, AZ 85726
[4]see J. Schneider's Extrasolar Planet Encyclopaedia at http://www.obspm.fr/encycl/encycl.html for an up-to-date compilation

differential direct imaging with ARIES on the MMT (Freed et al. 2002) and with TRIDENT (Marois 2002) will attempt to "subtract out" starlight by differencing images in two or more narrow bands in which only the planetary spectrum is expected to differ substantially. Such imaging techniques may work well in conjunction with adaptive optics systems on large ground-based telescopes.

EGP masses themselves, rather than just lower limits, can be determined if transits are detected. Many ground-based transit surveys are in progress, such as STARE (Brown & Charbonneau 1999), OGLE (Udalski et al. 2002), and TEMPEST (Baliber & Cochran 2001). Space-based instruments, such as Kepler (Koch et al. 1998), MOST (Matthews et al. 2001), COROT (Antonello & Ruiz), and MONS (Christensen-Dalsgaard 2000) will be able to detect transits with very high photometric precision. Additionally, such sensitive instruments should be able to discern reflected light from EGPs that do *not* transit their primaries, depending upon the details of the planetary phase functions. The eventual microarcsecond astrometry of the Space Interferometry Mission (SIM) (Unwin & Shao 2000) could reveal the orbital inclinations and, hence, the masses of virtually all known EGPs within the next decade. Perhaps of even greater import are space-based coronagraphic imaging missions, which may include *Eclipse* (Trauger et al. 2000; Trauger et al. 2001), the Jovian Planet Finder (Clampin et al. 2001), the Extra-Solar Planet Imager (Melnick et al. 2001), and NIRcam on the NGST (Rieke et al. 2002; Boccaletti 1999). Such advanced instruments are specifically designed for high-contrast imaging and/or spectrophotometry of EGPs. These missions should provide fundamental EGP atmospheric data, which in combination with theoretical models is certain to advance our understanding of these systems.

While there are many similarities with brown dwarfs, external stellar irradiation can have an overwhelming influence on EGP atmospheres, particularly for the very close-in objects, while most known brown dwarfs experience little external radiation. At the very least, the heating of an EGP atmosphere by such irradiation alters its equilibrium chemical composition and, hence, its emergent spectrum. Furthermore, the short-wavelength spectrum of an EGP will differ from that of a brown dwarf due to the reflection of starlight by condensates in its outer atmosphere and/or due to Rayleigh scattering, phenomena largely responsible for the visible and near-infrared spectra of the giant (and other) planets of our Solar System. While one cannot cleanly split the emergent spectrum of an EGP into reflected light and emitted light, the vast majority of the flux (F) in the visible region for an EGP of moderate to large orbital distance is reflected starlight. Distant EGPs are not hot enough to emit large thermal fluxes in this region of the spectrum.

Early investigations of EGP atmospheres and spectra neglected thermal emission and concentrated on albedo and reflection spectra for a range of EGP compositions, using planar radiative transfer codes. Marley et al. (1999) used temperature-pressure (T-P) profiles of isolated brown dwarfs, while Sudarsky et al. (2000) used both isolated and more nearly isothermal profiles to bracket the effects of compositional differences on the albedo and reflection spectra of EGPs. Albedo and reflection models provide useful spectral information for the full range of EGPs, although they are most accurate for objects at moderate to large orbital distances.

The move toward fully self-consistent atmosphere models of close-in EGPs was begun by Seager & Sasselov (1999) and Goukenleuque et al. (2000) using modified planar stellar atmosphere codes to model 51 Peg b. With incoming fluxes at both boundaries (the outer due to the central star and the inner due to the internal luminosity of the EGP), the T-P profile is adjusted iteratively until the net flux at every depth zone is the same (or nearly so). Relative to a brown dwarf atmosphere of similar temperature, the resulting profile is more isothermal due to outer atmospheric heating by the incident stellar flux. Seager & Sasselov explored the differences between cloud-free and dusty atmospheres and used basic equilibrium gas abundances without the alkali metals. A similar approach was taken by Goukenleque et al., except that their deep silicate cloud layer acted as a reflecting layer at the lower boundary; radiative processes within and below the cloud were not considered.

Additional self-consistent modeling of EGPs was completed by Seager, Whitney, and Sasselov (2000, SWS) and Barman, Hauschildt, and Allard (2001, BHA). SWS used a planar atmosphere code to model close-in EGPs, as in their previous work, but they also produced theoretical optical photometric light curves and polarization curves using phase functions from their separate 3-D Monte Carlo calculations. The effects of various condensates and particle sizes on the variability were investigated. BHA used an atmosphere code to model a range of EGP orbital distances from generic close-in objects to those at 1 AU. Both cloud-free and dusty atmospheric compositions were explored. Both groups assumed condensate layers with infinite scale heights (i.e. extending vertically to the lowest pressures of their models). Such models provide upper limits to the effects of condensates on the emergent spectra of EGPs, and along with the cloud-free models, they likely bracket the actual emergent spectra.

Unlike brown dwarfs, whose temperatures are not expected to vary significantly as a function of latitude or longitude, EGPs have a day side and a night side. Hence, an EGP atmospheric T-P profile may be a strong function of the angle from the substellar point, particularly for slow-rotating or close-in objects. This dependence will be a function of the planet's rotational period, although a proper understanding would require a radiative-hydrodynamic treatment, since winds will transport material from the higher-temperature day side to the night side of the planet (Cho et al. 2002; Showman & Guillot 2002). While such complex meteorology is beyond the scope of the present work, it is possible to compute the equilibrium temperature ($\mathrm{T_{eq}}$) of the planet, the effective temperature it would have in the *absence* of an intrinsic luminosity (inner boundary flux), based on a few parameters: the stellar luminosity (L_*), the Bond albedo of the planet (A_B), and the orbital distance of the planet (a). The result is:

$$T_{\rm eq} = \left[\frac{(1\text{-}A_B)L_*}{16\pi\sigma a^2 f}\right]^{1/4} \tag{1}$$

where σ is the Stefan-Boltzmann constant and the factor f is equal to unity for re-emission by the planet over its entire surface or equal to 0.5 for re-emission from only the illuminated hemisphere (Saumon et al. 1996). This factor may tend toward unity for a planet that is rotating very quickly if the heat is well redistributed. For a slow rotator, this factor might be closer to 0.5 since re-radiation from the day side would be significantly greater than that from the night side.

The spectra of EGPs strongly depend upon their outer atmospheric chemical compositions, which in turn depend upon the run of temperature and pressure with atmospheric depth. Because of qualitative similarities in the compositions and spectra of objects within several broad $T_{\rm eq}$ ranges, EGPs fall naturally into groups, or composition classes (Sudarsky et al. 2000). Since $T_{\rm eq}$ is a function of stellar luminosity and orbital distance (eq. 1), an EGP's class will depend upon these quantities as well. Such a classification scheme, however preliminary, brings a degree of order to the rich variety of EGP systems known to exist today.

A "Jovian" class of EGPs (Class I) exists at low temperatures ($\lesssim$ 150 K). Such planets are characterized by tropospheric ammonia clouds and strong gaseous methane absorption and include Jupiter and Saturn themselves. Somewhat warmer Class II, or "water class" EGPs are affected by condensed H_2O, as well as water and methane vapor. When the outer atmosphere of an EGP is too hot for water to condense, radiation generally penetrates more deeply. In these objects, designated Class III, "clear" or "gaseous," due to a lack of condensation in their outer atmospheres, ro-vibrational molecular absorption is very effective. In those EGPs with exceedingly small orbital distance and outer atmospheric temperatures in excess of $\sim$900 K (Class IV), strongly pressure-broadened resonance lines of sodium and potassium are expected to dominate the visible spectrum, while molecular absorption in the infrared remains strong. The very hot Class V EGPs orbit even closer to their primaries ($\sim$0.05 AU) than Class IV EGPs. These extremely close-in "roasters" are hot enough and/or have a low enough surface gravity that silicate and/or iron clouds condense high in the outer atmosphere and can have substantial effects on the reflected spectrum.

The present work is a detailed study of EGP atmospheres and spectra, including individual models representative of the full range of systems known today. Using a self-consistent planar atmosphere code (Hubeny & Lanz 1995) along with the latest atomic and molecular cross sections, cloud models, Mie theory treatment of grain scattering and absorption, and incident stellar fluxes (Kurucz 1994) (themselves a function of orbital distance), we produce an extensive set of theoretical EGP model atmospheres and emergent spectra.

In §2, we begin our study of EGP spectra and atmospheres with a discussion of atmosphere modeling, including numerical techniques and assumptions. In §3, we review some basic equilibrium chemistry and explore the compositions of EGPs, discussing gas-phase species as well as condensates. In §4, we discuss some of the relevant absorption and scattering opacities. Section 5 begins our presentation of EGP model atmospheres and spectra. In particular, this section defines and describes the five different classes of EGPs, from the cold Class I Jovian-types to the hot "roasters" with orbital periods of only a few days, and presents their generic temperature-pressure structures and emergent spectra. In §6, we present some systematic results as a function of orbital distance, inner flux boundary condition, surface gravity, and cloud particle size. This section provides a sense of the overall parameter dependences of the irradiated EGP spectra and atmospheres. Section 7 is an extensive discussion of a number of representative, known EGP systems. Atmosphere models, emergent spectra, and planet-to-star flux ratios, of central importance to any campaign to detect EGPs directly, are provided. This is followed in §8 by a discussion of current and future ground-based and space-based missions, in light of our theoretical results. We conclude in §9 with a summary of our most important findings.

2. NUMERICAL TECHNIQUES FOR MODELING EXTRASOLAR GIANT PLANETS

Numerical atmosphere modeling entails the combination of a radiative transfer technique with atmospheric structure and boundary constraints. Because the atmospheric temperature-pressure structure is almost always strongly coupled to the transfer of radiation, most methods converge on a self-consistent solution through an iterative process. The minimum requirements for a converged model include the satisfaction of hydrostatic equilibrium and a constant net flux of radiation throughout the atmosphere (constant to within some very small fraction; we choose 0.1%).

To calculate fully consistent, radiative equilibrium atmospheres and spectra we have employed the computer program TLUSTY (Hubeny 1988; Hubeny & Lanz 1995). TLUSTY uses the very efficient Complete Linearization/Accelerated Lambda Iteration (CL/ALI) hybrid method (Hubeny & Lanz 1995) that combines the advantages of Complete Linearization (Auer & Mihalas 1969), where only a few iterations are needed to obtain a converged model, with the ALI scheme's modest time requirements per iteration (Hubeny 1992).

TLUSTY allows for several radiative transfer formal solvers - the original Feautrier method (Feautrier 1964; Mihalas 1978), the 4-th order variant (Auer 1976), and the Discontinuous Finite Element (DFE) scheme (Castor, Dykema, & Klein 1992). However, we have found that for irradiated EGPs the DFE method is preferable. In the case of strong irradiation, the Feautrier scheme can often lead to negative emergent fluxes at the shortest wavelengths. This is because the Feautrier method does not evaluate the specific intensity $I(\nu,\mu)$ itself, but rather its symmetric part, $j(\nu,\mu) = [I(\nu,\mu) + I(\nu,\text{-}\mu)]/2$. At the surface, the emergent flux is evaluated as

$$H^{\rm out}(\nu) = \int_0^1 j(\nu,\mu)\mu\, d\mu \text{-} (1/2)\int_0^1 I^{\rm ext}(\nu,\text{-}\mu)\mu\, d\mu] \equiv \int_0^1 j(\nu,\mu)\mu\, d\mu \text{-} \qquad (2)$$

If the thermal source function at the surface, $S_\nu(0)$, is very small compared to the incoming radiation, the emergent flux is given as a difference between two quantities of almost the same value; the difference thus becomes quite inaccurate. If the ratio $S_\nu(0)/I^{\rm ext}(\nu)$ is smaller than machine accuracy (roughly 10^{-15}), which may indeed happen at optical wavelengths for EGPs irradiated by a solar-type star, in evaluating $j(\nu,\mu)$ using the Feautrier scheme the difference is completely dominated by rounding errors. In contrast, the DFE method is a first-order method that evaluates the specific intensity $I(\nu,\mu)$ directly and is not vulnerable to such rounding errors.

Because the outer atmospheres of brown dwarfs and EGPs are thin compared with the radii of these objects, we use a planar geometry for modeling both isolated and irradiated objects. A one-dimensional planar atmosphere code is the simplest means for the self-consistent modeling of EGPs. Unlike an isolated brown dwarf, it is likely that the atmospheric temperature-pressure structure of an EGP will vary substantially as a function of latitude and longitude. While a planar code cannot account for such variation, an approximate means of accounting for the different amounts of external flux received by a planet along its surface is to take a suitable average. No such adjustment would be necessary if it were a plane that was being irradiated. In that case, the total power received by the plane would simply be $\pi R^2 F$, where F is the incident flux and R is the radius of the plane (or disk). If this same flux were received instead by a hemisphere, the energy would be distributed unevenly over an area of $2\pi R^2$. In this case, the average energy received per unit area would be $F/2$, not F. When using a planar code, one can account for this difference by weighting the incident flux by a factor of $1/2$. Finally, if we want the average energy per time per unit area received by the full sphere (i.e. giving equal weighting to the night side of the planet), the adjustment is $F/4$. Such "redistribution" over the full sphere may be appropriate for a very fast rotator. Unless stated otherwise, in this work we choose to redistribute the incident energy over the front hemisphere of the planet only. Some researches have chosen to redistribute over the full sphere, while others have chosen not to redistribute at all. We will point out these differences when comparing our models with those of others. Furthermore, the spectra we show are the so-called "phase-averaged" spectra for which we distribute uniformly in solid angle the total energy reradiated and comimg from the inner boundary. In this way, energy *in* equals energy *out* and energy is conserved. The phase functions, however, are not calculated and we defer this to another paper. Since the variation with phase is generally smaller than the variation from model to model (SWS) and as a function of wavelength, and since the inclination angles of the orbits of most known EGPs are not known, given our goal of mapping out the entire model space for irradiated EGPs, the choice of phase-averaged spectra is convenient and sensible.

There is a rich history of stellar atmosphere modeling, and these same basic techniques are used for EGPs and brown dwarfs. But unlike most stars, save the latest M-dwarfs, the outer atmospheres of substellar objects commonly contain condensed species, such as grains in relatively hot objects or water or ammonia clouds in cool EGPs. The usual treatment of the scattering of radiation in stellar atmospheres assumes forward-backward scattering symmetry (and often simply isotropic scattering), but condensates in EGPs and brown dwarfs typically scatter strongly in the forward direction. Relative to isotropic scattering, forward scattering reduces the albedo of an atmosphere, because on average more scattering events would be required for a photon to emerge from the atmosphere before being absorbed. A useful approximation that allows one to maintain symmetric scattering numerically is to account for the asymmetry in the scattering of radiation by reducing the actual scattering cross section by $1-g$, where g is the averaged cosine of the scattering angle. In an optically thick medium, this so-called "transport cross section" mimics the effects of asymmetric scattering quite well (Sudarsky et al. 2000) and we use it in the calculations we present in this work.

3. ATMOSPHERIC COMPOSITIONS

The emergent spectra of EGPs are determined mainly by their outer atmospheric chemical compositions. But unlike stars, whose atmospheres are dominated by gaseous species (grain formation occurs only in the coolest M dwarfs) most EGPs also contain condensed species that contribute substantially to the opacities. Some condensates, such as water ice or iron grains, are formed homogeneously (i.e. from a single species), while the formation of others such as forsterite or gehlenite is heterogeneous, resulting in the depletion of several gas-phase species. The largely unknown meteorology in EGP atmospheres and condensate sedimentation, or "rainout," makes the depth-dependent composition modeling of EGPs a difficult task.

Any method useful in determining compositions of EGP atmospheres must be capable of treating the gaseous, liquid, and solid phase species simultaneously. Additionally, the rainout of species must be handled appropriately, because the removal of a given species to deeper layers by such sedimentation can alter chemical abundances drastically. We use results from the chemical equilibrium code of Burrows and Sharp (1999), which includes a prescription to account for the rainout of species in a gravitational field. Our fiducial models assume an Anders and Grevesse (1989) solar composition of 27 elements (H, He, Li, C, N, O, F, Ne, Na, Mg, Al, Si, P, S, Cl, Ar, K, Ca, Ti, V, Cr, Mn, Fe, Co, Ni, Rb, Cs), resulting in approximately 300 molecular gas-phase species and over 100 condensates. From this large set of species, only some have the requisite abundances to have significant effects on the emergent spectra and/or temperature-pressure (T-P) structure.

3.1. Chemical Abundances in EGPs and Brown Dwarfs

The equilibrium gas-phase and condensed-phase abundances of species at a given pressure, temperature, and elemental composition are obtained by minimizing the total free energy of the system. The abundances of most species are highly dependent on temperature, as well as moderately dependent on pressure. As an example, consider the balance of CO and methane, the dominant equilibrium forms of carbon that are governed by the process:

$$CO + 3H_2 \longleftrightarrow H_2O + CH_4. \tag{3}$$

For exothermic processes, such as this one, an increase in temperature at a given pressure favors the reactants, so equilibrium favors CO over CH_4 with increasing temperature. But at increased pressure (for a fixed temperature), the side of the reaction with fewer molecules is favored (Le Chatelier's Principle), which results in a greater CH_4 abundance at the expense of CO. The analogous process that governs N_2 and NH_3 abundances, the dominant equilibrium forms of nitrogen, is

$$N_2 + 3H_2 \longleftrightarrow 2NH_3. \tag{4}$$

At high temperatures, N_2 is favored, but the equilibrium shifts toward NH_3 with increasing pressure (cf. the Haber process).

These temperature and pressure dependences have direct implications for the atmospheric compositions of EGPs and brown dwarfs. In brown dwarfs, CH_4 is the primary carrier of carbon (number fraction: $\sim 6 \times 10^{-4}$) in the outer atmosphere, but a transition to CO occurs at depth, due to increasing temperature. Similarly, the outer atmospheres of EGPs at large orbital distances tend to be dominated by methane, due to their low atmospheric temperatures. In contrast, in the low-pressure outer atmospheres of close-in EGPs ($\sim$ 0.05 AU), CO is dominant due to strong irradiation (and heating) by the central star. Analogous transitions between NH_3 and N_2 as the dominant carrier of nitrogen ($\sim 2 \times 10^{-4}$) occur as well, but at lower temperatures than those for CH_4 and CO.

At the temperatures and pressures of EGPs and brown dwarfs, H_2O is the main reservoir of oxygen and is the third most abundant species, with a mixing ratio of $\sim 10^{-3}$, behind H_2 ($\sim$ 0.83) and He ($\sim$ 0.16). The H_2O abundance is reduced somewhat at high atmospheric temperatures because CO competes for oxygen (eq. 3) and because silicates form.

TiO and VO, important molecular species in the atmospheres of M dwarfs and some brown dwarfs, form at temperatures greater than $\sim$2000 K, as do CrH and FeH. The alkali metals persist to much lower temperatures ($\sim$ 1000 K) and sodium and potassium can be particularly important both in brown dwarfs and in the hotter of the EGP classes. Although their abundances are relatively low, Na ($\lesssim 3 \times 10^{-6}$) and K ($\lesssim 2 \times 10^{-7}$) are strong absorbers in the visible region of the spectrum. For most EGPs and brown dwarfs, the Na and K abundances are negligible in the outermost atmosphere, but at depth the mixing ratios of both can rise rapidly. In the case of a strongly-irradiated, close-in ($\sim$0.05 AU) EGP, Na and K abundances can reach their maximum even at the lowest atmospheric pressures. The other alkali metals, lithium, rubidium, and cesium, are present in EGPs and brown dwarfs as well, albeit in lower abundance. Sulfur appears in the form of H_2S at low-to-moderate abundance over a large range in temperature and pressure, while phosphorus is in the form of PH_3.

3.2. Condensation and Rainout

The condensation and gravitational settling of species results in compositions that differ significantly from those for true equilibrium. Condensation sequesters most of the heavier elements, such as silicon, magnesium, calcium, aluminum, and iron, in compounds that settle, or rain out, leaving the upper atmosphere depleted of species that would otherwise contribute to the molecular chemistry. Condensates are very important in their own right as well, often providing substantial absorption and scattering opacity in the visible and infrared spectral regions.

Some of the more refractory species expected to exist in EGP (and brown dwarf) atmospheres are calcium-aluminum compounds, such as $Ca_2Al_2SiO_7$ (gehlenite), and aluminum oxides, such as Al_2O_3 (corundum). Since both calcium and aluminum are less abundant than silicon or oxygen, the formation and gravitational settling of these condensates should consume most of the calcium and aluminum, thereby depleting the upper atmosphere of these metals. The atmospheric temperature and pressure at which this occurs depends on the details of the particular T-P profile. For a given mass, the T-P profile of an irradiated object (as opposed to an isolated object) will intersect the condensation curve of the refractory species at a lower temperature and pressure, so the condensate will settle higher (at lower pressure) in the atmosphere.

Another refractory species, TiO, can condense into the calcium titanates (Lodders 2002) and/or into titanium oxides in EGP atmospheres. Iron is expected to condense mainly in a homogeneous manner rather than as FeS or some other heterogeneous species, because the condensation temperature for pure iron is quite high ($\sim$1500-2300 K, depending significantly on pressure). In contrast, the homogeneous condensation of VO is unlikely because vanadium condenses into solid solution with titanium-bearing condensates (Lodders 2002).

The silicates are somewhat less refractory, so in general, they will appear higher in the atmosphere (i.e. at lower temperature and pressure). The exact composition of the silicates is unknown, although some common species include $MgSiO_3$ (enstatite) and Mg_2SiO_4 (forsterite). Of these two possibilites, forsterite is more likely to exist in EGP and brown dwarf atmospheres because it has a higher condensation temperature and so will consume most of the magnesium, the limiting element. And although Mg_2AlO_4 (magnesium-aluminum spinel) condenses at even higher temperatures, it is unlikely to form in abundance because most of the aluminum will be consumed by the formation of corundum and/or other aluminum compounds. In brown dwarf and giant planet atmospheres, forsterite will condense within the $\sim$ 1500-2000 K range, depending upon atmospheric pressure. We should mention that forsterite and enstatite are only two species in the olivine ($Mg_xFe_{1-x}SiO_3$) and pyroxene ($Mg_{2x}Fe_{2-2x}SiO_4$) sequences, respectively. The optical properties of other such species have been explored by Dorschner et al. (1995). If iron has not been fully removed by homogeneous condensation and rain out—and it is unlikely that homogeneous condensation will consume all the iron—then some of these iron-bearing species are likely to form.

The alkali metal abundances are higher in a rainout scenario than they are in the true equilibrium case. In the true equilibrium case, $NaAlSi_3O_8$ (high albite) and $KAlSi_3O_8$ (high sanidine) can condense, lowering the gas-phase abundance of sodium and potassium (Burrows & Sharp 1999). But in the more realistic rainout scenario, the aluminum is consumed by other species that condense at higher temperature, such as $Ca_2Al_2SiO_7$ (gehlenite). Gravitational settling then removes the aluminum from the upper atmosphere, thereby inhibiting the formation of sodium- and potassium-bearing condensates.

At cooler temperatures ($\sim$700-1100 K), sulfide and chloride condensates are expected to sequester the alkali metals. Sodium will end up in Na_2S and/or NaCl (Lodders 1999), while potassium is likely to be in the form of KCl. Due to the low abundances of the alkalis, thick clouds are unlikely, but "cirrus-like" layers are certainly possible.

At lower temperatures, H_2O will condense homogeneously for atmospheric temperatures below $\sim$250 K. Hence, many EGPs at large orbital distances will contain water clouds, as will cool brown dwarfs. Even if only a small fraction of H_2O condenses, as governed by the degree of supersaturation (Cooper et al. 2002), the high abundance of H_2O and its large reflectivity in ice or liquid form indicates that condensed H_2O is important to the emergent spectra of EGPs.

At very low temperatures ($\sim$ 150-200 K), NH_3 and NH_4SH condense. NH_4SH condenses at somewhat higher temperatures than ammonia, so a layer of this heterogeneous material is expected to appear between a water cloud and an ammonia cloud in cold EGPs. Such is the case for the standard model of Jupiter. However, we do not model an NH_4SH layer because the optical constants for this material over a broad wavelength range are not available.

4. OPACITIES

The total gaseous absorption opacities are calculated by weighting the atomic and molecular opacity of each species by its abundance, all as a function of temperature and pressure. The resulting product is a large opacity table within which interpolation can yield the frequency-dependent total opacity at any point in the EGP or brown dwarf atmosphere.

Because both the gaseous abundances and their opacities vary substantially with temperature and pressure, the spectral region that dominates the opacity will differ for objects of different temperatures. To illustrate this fact, Figure 1 shows the P = 1 bar total gas opacity at two very different temperatures, 200 K and 1600 K. For a hot atmosphere, the visible region is overwhelmed by the sodium and potassium resonance lines, yet for a cool atmosphere, the visible is canvassed by weak methane absorption. These visible opacities (in cm^2 g^{-1}) differ by up to several orders of magnitude, but there are also spectral regions in the near infrared where the opacity of the cool atmosphere is greater than that of the hot atmosphere. In general, the bulk of the outgoing flux ultimately will find its way out of the object between the peaks in the opacity.

4.1. Rayleigh Scattering

Rayleigh scattering is a conservative scattering process by atoms and molecules. Although strong in the ultraviolet/blue, the scattering cross sections quickly fade toward the red region of the spectrum ($\propto \lambda^{-4}$). Rayleigh scattering has little effect on the spectra of isolated brown dwarfs, but irradiated EGPs reflect a fraction of the incident intensity in the ultraviolet/blue.

The Rayleigh scattering cross sections are derived from polarizabilities, which are in turn derived from refractive indices:

$$\sigma_{Ray} = \frac{8}{3}\pi k^4 \left(\frac{n\text{-}1}{2\pi L_0}\right)^2 , \quad (5)$$

where k is the wavenumber ($2\pi/\lambda$) and L_0 is Loschmidt's number, the number of molecules per cubic centimeter at STP ($= 2.687\times10^{19}$).

4.2. Scattering and Absorption by Condensates in EGP Atmospheres

Condensed species in substellar objects range from ammonia ice in low temperature EGPs to silcate, iron, and aluminum compounds at high temperatures. Some of the condensates relevant to EGP atmospheres include NH_3 ($\lesssim$ 150–200 K), NH_4SH ($\lesssim$ 200 K), H_2O ($\lesssim$ 250–300 K), low-abundance sulfides and chlorides ($\lesssim$ 700–1100 K), silicates such as Mg_2SiO_4 and/or $MgSiO_3$ ($\lesssim$ 1600–2000 K), iron or iron-rich compounds ($\lesssim$ 1700–2200 K), and aluminum or calcium compounds ($\lesssim$ 1700–2200$^+$ K). Additionally, photochemical processes in the upper atmosphere due to irradiation by a central star can produce non-equilibrium condensates. Stratospheric hazes may be composed of polyacetylene (Bar-Nun et al. 1988) and other aerosols. Chromophores, those non-equilibrium species which cause the coloration of Jupiter and Saturn, might include P_4 (Noy et al. 1981) or organic species similar to Titan tholin (Khare & Sagan 1984). Brown Dwarf atmospheres can contain a similar host of silicate, iron, and aluminum compounds. However, only the lowest temperature brown dwarfs will contain condensed water, since the temperatures are simply too high in most objects.

Condensates can have large effects on the emergent spectra of EGPs and brown dwarfs. The optical properties of most condensates are relatively featureless in comparison with molecular bands and atomic lines. Hence, the presence of condensates tends to "gray" the spectrum by shallowing the troughs and lowering the spectral peaks, providing opacity at the wavelengths at which the radiation would otherwise escape. In EGPs, condensates are the principal source of scattering of incident irradiation, and if located in the outer atmosphere, their presence increases the reflected flux in the visible and near-infrared regions of the spectrum. One exception is the presence of non-equilibrium photochemical species with absorptive optical properties in the UV/blue, a region of the spectrum that in the absence of these species can be quite reflective due to the Rayleigh scattering of incident radiation. It is such compounds that are thought to be responsible for the absorption in the blue in Jupiter and Saturn and their consequent reddish coloration.

Of course, those condensates that are higher in the atmosphere generally will have a greater effect on emergent spectra than those that reside more deeply, unless the high condensed layer is very optically thin. The presence and location of a particular condensed species is determined largely by an object's T-P profile, and by the tendency of the condensate to settle (rainout) to a depth in the atmosphere near the region where the T-P profile crosses the condensation curve (Burrows & Sharp 1999). Hence, a given low-temperature EGP atmosphere ($T_{eq} \lesssim$ 150 K) might consist of an ammonia cloud deck high in the troposphere and a water cloud deck somewhat deeper, with purely gaseous regions above, beneath, and between the clouds. Similarly, a higher-temperature atmosphere (T_{eq} $\sim$1200 K) might consist of a tropospheric silicate cloud deck above a deeper iron cloud deck. Depending upon the wavelength region and the amount of condensate in the upper cloud, the presence of deeper clouds may or may not have a recognizable effect on the emergent spectrum. If for a given wavelength the cloud deck resides at $\tau_\lambda \gg 1$, it will have little effect on the emergent spectrum.

The scattering and absorption of electromagnetic radiation by condensed species in planetary and brown dwarf atmospheres is a very complex problem. The scattering properties of ices, grains, and droplets of various sizes, shapes, and compositions cannot be described accurately by simple means. Most often, these scattering properties are approximated by Mie Theory, which describes the solution of Maxwell's equations inside and outside a homogeneous sphere with a given complex refractive index.

The principal condensates to which we have applied the Mie theory (roughly in order of increasing condensation temperature) include NH_3 ice, H_2O ice and liquid, $MgSiO_3$ (enstatite), Mg_2SiO_4 (forsterite), $MgAl_2O_4$ (magnesium-aluminum spinel), iron, Al_2O_3 (corundum), and $Ca_2Al_2SiO_7$ (gehlenite).

The optical constants (complex indices of refraction) for ammonia ice, H_2O ice, and H_2O liquid were obtained from Martonchik et al. (1984), and Warren (1984 and 1991), respectively. The constants for enstatite, magnesium-aluminum spinel, iron, and corundum were obtained from Dorschner et al. (1995), Tropf & Thomas (1990), and Gervais (1990), respectively. The indices for iron were provided by Aigen Li (private communication, 2002). Those for forsterite shortward of $\sim$33 μm were taken from Scott & Duley (1996); longward of this wavelength, the indices were provided by Aigen Li. For gehlenite, the real index was taken from Burshtein et al. (1993) and an absorbance spectrum (Rossman & Taran) was used to derive the imaginary index.

Some of these condensates have relatively strong absorption features. H_2O ice has broad absorption features at $\sim$ 1.5, 2, and 3, and 4.5 μm. Those of water in liquid form mirror these quite well, with only small displacements, mainly to shorter wavelengths. The silicates, $MgSi_2O_4$ and $MgSiO_3$ have broad features near 10 and $\sim$ 20 μm and at $\lesssim$ 0.2 and 0.35 μm, respectively. $MgAl_2O_4$ absorbs strongly only in the infrared, and especially around 15 and 20 μm. Ammonia ice, a principal condensate at low temperatures, exhibits little relative absorption in the blue and visible spectral regions. However, it can provide absorption in the infrared, with particular strength near 2.0, 2.25, 3, 4.3, 6.2, 9.5 micorns.

P_4 and tholin are chromophore candidates for the coloration of Jupiter and Saturn, due to their large imaginary indices of refraction in the ultraviolet/blue and their plausibility of production. A somewhat yellowish allotrope of phosphorus, P_4 was produced in the laboratory by Noy et al. (1981) by ultraviolet irradiation of an H_2/PH_3 gaseous mixture. It is believed that this same process may be responsible for its production in Jupiter. Tholin is a dark-reddish organic solid (composed of over 75 compounds) synthesized by Khare and Sagan (1984) by irradiation of gases in a simulated Titan atmosphere. A tholin-like solid may be produced similarly in giant planet atmospheres. Polyacetylenes, polymers of C_2H_2, were investigated by Bar-Nun et al. (1988) and likely are an optically dominant species in the photochemical stratospheric hazes of the Solar System giant planets, where hydrocarbons are abundant (Edgington et al. 1998; Noll et al. 1986). Due to uncertainties concerning their production in EGPs, we do not include P_4, tholin, polyacetylenes, or other nonequilibrium species in our baseline models.

Cloud particle sizes are not easily modeled and are a strong function of the unknown meteorology in EGP atmospheres. Inferred particle sizes in Solar System giant planet atmospheres can guide the construction of EGP models, although they range widely from fractions of a micron to tens of microns.

We have investigated various particle size distributions. A commonly used distribution is

$$n(a) \propto \left(\frac{a}{a_0}\right)^6 \exp\left[-6\left(\frac{a}{a_0}\right)\right], \qquad (6)$$

which reproduces the distribution in cumulus water clouds in Earth's atmosphere fairly well if the peak of the distribution is $a_0 \sim 4$ μm (Deirmendjian 1964; Deirmendjian 1969).

In the present work, we use this cloud distribution with various modal particle sizes. Our fiducial modal particle radius for water and ammonia is 5 μm, as inferred from Deirmendjian (1964) and measurements of Jupiter's atmosphere. For grains such as silicates and iron, our fiducial modal particle size is 10 μm, a value in broad agreement with recent cloud models for EGPs and brown dwarfs (Cooper et al. 2002; Ackerman & Marley 2001).

5. SPECTRA AND ATMOSPHERIC PROFILES FOR THE DIFFERENT COMPOSITION CLASSES OF EXTRASOLAR GIANT PLANETS

Due to qualitative similarities in the compositions and spectra of objects within several broad atmospheric temperature ranges, EGPs fall naturally into groups, or "composition classes"(Sudarsky et al. 2000). Figure 2 depicts sample temperature-pressure structures for Classes I through V. Also shown are the condensation curves for the principal condensates, ammonia, water, forsterite (a representative silicate), and iron. The intersection of a T-P profile with a condensation curve indicates the approximate position of the base of a condensate cloud. (For clarity, the T-P profiles of cloud-free models are shown.) The Class I profile intersects the ammonia condensation curve at roughly one bar. At greater pressures, the temperature is too high for ammonia condensation to occur. This profile also intersects the water condensation curve at nearly 10 bars, indicating the presence of water clouds at this depth. Of course, a whole variety of Class I objects with differing T-P profiles will exist, and the ammonia and water condensation curves will be intersected at different pressures for each object, but by definition Class I EGPs have an ammonia cloud that is well above a water cloud. The warmer Class II profile crosses only the water condensation curve, indicating the existence of a water cloud in the upper atmosphere. Classes IV and V intersect the silicate and iron condensation curves, but at quite different pressures. Figure 2 is a general guide to the T-P structures and approximate positions of the various principal condensate clouds in the atmospheres of a full range of EGPs.

5.1. Jovian Class I EGPs

Class I EGPs orbit at distances of at least a few AU from their central stars. With $T_{eq} \lesssim 150$ K, the spectrum of such a cool, Jovian-like gas giant at 10 parsecs is shown in Figure 3. Methane and ammonia are the dominant gaseous species, because at these low temperatures, carbon is predominantly in the form of CH_4 rather than CO, and nitrogen is in NH_3, as opposed to N_2. The visible and near-infrared spectrum is comprised mostly of reflected stellar light, since such an object is far too cool to emit significant thermal radiation at short wavelengths. This reflection is provided mostly by the upper ammonia cloud, with some additional contribution in the blue due to Rayleigh scattering. Some ammonia ice absorption features are also indicated in Figure 3 by the $\{NH_3\}$ symbols; for ammonia ice, the imaginary index of refraction is rather large at $\sim$1.5, 1.65, 2, and 2.2 μm. The upper atmosphere is largely depleted of H_2O, which has condensed and settled into a cloud layer at several bars pressure. Provided that the upper ammonia cloud is optically thick (here we assumed a particle size distribution peaked at 5 microns, with a condensate abundance at 10% of the total ammonia abundance), one should not expect to see substantial effects due to gaseous or condensed H_2O in the visible or near infrared emergent spectrum.

In our present-day Solar System, both Jupiter and Saturn are Class I objects, but it is important to note that not all EGPs orbiting at several AU will be Class I planets. Young and/or massive objects may have high enough inner flux temperatures (defined as $(F/\sigma)^{1/4}$ for an object in *isolation*) that ammonia will remain in gaseous form. Therefore, those hotter objects will be Class II (or even Class III).

5.2. Water Class II EGPs

Class II EGPs generally orbit at a distances of $\sim$1 to 2 AU, or somewhat farther out for an object orbiting an early-type central star. Outer atmospheric temperatures ($\lesssim$ 250 K) are below that of the water condensation curve, producing a tropospheric cloud layer of H_2O. Figure 4 shows an example spectrum of a Class II EGP. Reflection in the visible and near-infrared is provided primarily by the water cloud, which we have assumed to be comprised of a particle size distribution peaked at 5 microns. While scattering by this H_2O condensate layer elevates the emergent spectrum, the spectrum is dominated by the gaseous absorption features of water, methane, and to a lesser extent, ammonia.

5.3. Gaseous Class III EGPs

Class III EGPs are too warm to contain condensed H_2O, but are too cool for silicate or iron grains to exist in their outer atmospheres. In the absence of principle condensates, we label this class the "gaseous" or "clear" class. Typically orbiting at distances less than about 1 AU, such objects have equilibrium temperatures between $\sim$ 350 K and 800 K. Although an isolated object with $T_{eq} \sim 350$ K is likely to contain water clouds, stellar irradiation keeps the temperature of a Class III EGP high enough that its profile never reaches the condensation curve.

A purely gaseous EGP is expected to have a very low albedo (Sudarsky et al. 2000). Rayleigh scattering does have an impact in the blue and visible regions of the spectrum, but the majority of the spectrum is made up almost entirely of absorption and emission. Figure 5 shows an example spectrum of a Class III EGP. Gaseous water and methane absorption are strong, while ammonia absorption is weaker than for a Class II. The alkali metals, particularly the sodium and potassium resonance lines at $\sim$ 0.6 μm and $\sim$ 0.77 μm, respectively, appear with modest intensity. Due to the absence of clouds, the incident radiation penetrates deeply between the near-infrared ro-vibrational absorption bands. Here, collision-induced absorption (CIA) by H_2, a continuum absorption that is strong near $\sim$0.8, 1.2, and 2.4 μm, keeps the flux peaks lower than they would be otherwise.

The slope of the visible spectrum is a combined consequence of the λ^{-4} dependence of Rayleigh scattering and the incident stellar spectrum. The later the stellar spectral type, the flatter the slope will be if the spectral energy distribution of the star falls off rapidly with decreasing wavelength.

Figure 6 provides a comparison of the T-P structure of a Class III model with that of a cloud-free brown dwarf of the same gravity and integrated emergent flux. As expected, the EGP profile is more isothermal in the outer atmosphere, while it is somewhat cooler than the brown dwarf deeper in the atmosphere. Figure 7 depicts the emergent spectra associated with these profiles out to 30 μm. By construction, both integrated emergent fluxes are identical, but the individual spectral energy distributions differ significantly. Most striking is the visible region. Here, Rayleigh scattering of the incident radiation keeps the EGP flux high relative to that of the brown dwarf. Only modest sodium and potassium lines appear in the EGP spectrum, compared with very strong lines for the brown dwarf. This fact is not due to a dominance of Rayleigh scattering cross sections; the alkali cross sections are actually much larger. Rather, the equilibrium abundances of the alkalis are very low in the outermost atmospheres of both the EGP and the brown dwarf. The alkali absorption in a brown dwarf of this effective temperature occurs at pressures of $\gtrsim$ 1 bar, but the strong impinging radiation on the EGP in the visible region is reflected by Rayleigh scattering higher in the atmosphere, producing emergent flux in the visible, before this pressure region is well probed. So although alkali absorption occurs in both objects at moderate pressures, strong alkali absorption is seen only in the emergent spectrum of the brown dwarf. This is not the case if the outer atmosphere is at higher temperature, as for Class IV objects.

In the near-infrared, the peak-to-trough variations in the molecular absorption are greater in the brown dwarf than in the Class III EGP, which is expected due to the more isothermal profile of the EGP. In the case of the brown dwarf, more flux escapes in the Z, J, and to a lesser degree, the H band. But beyond the K band, the EGP infrared flux is somewhat higher.

5.4. Close-In Class IV EGPs

The close-in Class IV EGPs are those orbiting their stars well within the distance at which Mercury orbits the Sun. Many are roughly 0.1-0.2 AU from their central stars, or even closer for late-type stars. Giant planets at such small orbital distances are quite exotic by the standards of our Solar System, and their spectra are as well. With atmospheric temperatures in the 1000 K range, the alkali metal abundances increase substantially and CO takes up much of the carbon in the low-pressure outer atmosphere.

Figure 8 shows a Class IV EGP spectrum. Perhaps most striking is the strong absorption due to the sodium (0.59 μm) and potassium (0.77 μm) resonance lines. These lines are strongly pressure-broadened and clearly dominate the visible spectral region. Also present are the lithium ($\sim$

0.67 μm), rubidium ($\sim$ 0.78, 0.795 μm; not labeled), and cesium doublets ($\sim$ 0.85, 0.895 μm; not labeled).

CO absorption is very strong in the 4.4-5.0 micron region, as well as at $\sim$ 2.3 μm. This comes at the expense of methane, which competes for carbon. However, methane absorption is still apparent, particularly the 3.3-μm ν_3 fundamental feature. Although methane absorption is weaker, water absorption remains very strong, and, as for Class III objects, H_2 CIA absorption affects the near-infrared. At these high temperatures, N_2 takes up most of the nitrogen, so ammonia abundances are very low.

Silicate and iron clouds do form, but too deeply ($\gtrsim$ 10 bars) to affect the emergent spectrum significantly. Figure 9 shows the effect of a silicate cloud on the T-P profile. Despite the changes in the T-P structure at depth, the emergent spectrum is nearly identical to the cloud-free model. Both spectra are shown in Figure 10.

The very strong alkali absorption shown here is likely an upper limit since the neutral alkali abundances could be reduced somewhat by ionizing ultraviolet flux or scattering by low-abundance, nonequilibrium photochemical products. In any event, strong alkali lines are expected to be prominent features of close-in Class IV EGPs.

5.5. Class V Roasters

The hottest of all EGPs are the extremely close-in Class V EGPs, or "roasters." These objects orbit their stars around 0.05 AU. The first EGP discovered, 51 Pegasi b, is a good example of a roaster. Many of these objects have equilibrium temperatures that rival hot brown dwarfs ($\gtrsim$ 1400 K). Silicate and iron clouds can form quite high in the atmospheres of these EGPs, especially for low-mass, low-gravity roasters, and they have significant effects on the emergent spectra.

Figure 11 shows the emergent spectrum of a Class V roaster. Like Class IV EGPs, Class V objects have strong alkali metal absorption lines, although their strengths can be reduced somewhat due to reflection by condensates at altitude, and/or if the outer atmosphere becomes isothermal. Water and CO absorption remain strong, but unlike Class IV objects, where some methane absorption is seen, methane features in the visible and near infrared are either very weak or nonexistent, even at the 3.3-μm fundamental band.

The presence of high clouds in Class V EGPs results in smaller wavelength-dependent flux variations relative to Class IV EGPs. This is mainly a result of cloud opacity blocking the flux windows between the molecular absorption features, thereby reducing the flux peaks. As a result, the absorption troughs are not as deep, since some of the blocked flux escapes in these spectral regions. Additionally, clouds reflect some of the incident stellar radiation, increasing the incident flux where the scattering opacity is high, a phenomenon that tends to be more noticeable in the vicinity of the gaseous absorption troughs.

6. GENERIC MODEL SEQUENCE FROM 5 AU TO 0.05 AU AND PARAMETER STUDIES

A generic sequence of EGP models at various orbital distances from a given primary can be very instructive. For simplicity, we produce a cloud-free sequence, and the inner boundary flux is set equal to that of an isolated object with $T_{\rm eff}$ = 125 K. The resulting EGP models are compared with a model of an isolated EGP/brown dwarf with the same inner boundary flux (i.e., effective temperature) and gravity (3×10^3 cm s^{-2}).

Figure 12 illustrates the effects of irradiation on the temperature-pressure structure of an EGP at various distances, from 5 AU to 0.05 AU from a G0V primary. Even at a distance of 5 AU, the stellar irradiation significantly alters the T-P profile of the planet relative to the isolated object, and this effect becomes quite extreme for objects closer than $\sim$1 AU.

Figure 13 shows the emergent spectra of these models, including that for the isolated object. From high to low atmospheric temperature, one can see certain atomic and molecular features appear and disappear. For the objects orbiting most closely to the primary, the alkali absorption lines in the visible are strong, as are the CO features at 2.3 μm and $\sim$4.4 to 5 μm. But as the EGP is moved away from the primary, the alkali lines weaken, giving way to Rayleigh scattering by the gaseous species high in the atmosphere, where the alkali abundances are negligible. The CO features quickly weaken as well, while methane absorption becomes quite strong, particularly at 3.3 μm. Water absorption remains strong for the full model set, which is not surprising considering its high abundance throughout a very broad range of temperatures and pressures.

It is clear from Figure 13 that for wavelengths greater than $\sim$ 0.8 μm and larger orbital distances the emergent spectrum of an EGP approaches that of an isolated object with the same inner boundary flux. However, this is not true in the visible region of the spectrum. Here, reflection of the incident stellar radiation keeps the emergent flux from matching the very low flux of the isolated object.

Figure 14 shows spectra for the same run of distances, but with an inner boundary flux associated with an effective temperature of not 125 K, but 500 K. This model sequence mimics the expected behavior for an irradiated low-mass ($\sim$3 $M_{\rm J}$), young ($\sim 10^8$ yr) brown dwarf, and is very similar to that of a higher-mass, older brown dwarf (e.g., 10^9 yr/15 $M_{\rm J}$ or 10^{10} yr/35 $M_{\rm J}$). As in Fig. 13, Rayleigh scattering is responsible for the elevated flux in the optical, but exterior to $\sim$0.5 AU in the near- and mid-infrared the flux becomes independent of orbital distance. The comparison between Figs. 14 and 13 is dramatic. Again, in general the infrared flux becomes independent of the EGP/brown dwarf's orbital distance once this distance is great enough that the object's internal luminosity begins to dominate the emergent spectrum.

The planet-to-star flux contrast as a function of wavelength is of central importance in any campaign to detect EGPs directly. We plot in Fig. 15 these planetary phase-averaged, planet-to-star flux ratios for the models of Figure 13. It is important to stress that these are generic, cloud-free models, which assume a central star of type G0V and an inner flux that corresponds to an effective temperature of 125 K. Nevertheless, Fig. 15 illustrates clearly the generic dependence of the planet-to-star contrast on orbital distance. For a very close-in object, the flux ratio varies from $\lesssim 10^{-5}$ in the visible to $\lesssim 10^{-3}$ in the 3.8-4.0 μm region. In almost all cases, this ratio becomes smaller at all wavelengths with increasing orbital distance (as expected from the a^{-2} diminution of stellar flux at the planet). However, for orbital distances between ~0.1 and 0.2 AU and in the 4.4 to 4.8 μm wavelength range, CO's absorption strength wanes with increasing distance and the associated decrease in atmospheric temperature. This temporarily buoys the flux in the M band until the CO has been replaced by CH_4. Nevertheless, the M band between 4.0 and 5.0 μm is always a relatively bright region of the spectrum in which to probe for EGP's, irradiated or otherwise.

For a low inner boundary flux and cloud-free atmospheres, the EGP contrast ratio in the near infrared plummets and can reach values of 10^{-10} to 10^{-15}. The corresponding ratio in the visible approaches 10^{-9} to 10^{-10} (again, for cloud-free atmospheres). However, since the flux in the Rayleigh-Jeans tail is proportional to T_{eq}, not T_{eq}^4, and $T_{eq} \propto a^{-1/2}$, the planetary flux in the mid- and far-infrared does not decrease as fast. This makes the planet-to-star contrasts in the mid-IR wavelengths longward of ~10 μm quite high and suggests that mid-IR searches could be quite profitable.

6.1. Effects of Inner Boundary Flux

Above we studied the effect of varying the outer boundary flux, while holding the inner boundary flux constant. In this section, we'll explore just the opposite, holding the outer boundary flux constant while varying the inner boundary flux.

Without evolutionary models, it is not possible to know the correct inner boundary flux when modeling the atmospheres of EGPs. This inner boundary flux fixes the *net* flux at the surface (not to be confused with the emergent flux, the outward flux at the surface), so long as there are no sources or sinks throughout the atmosphere. That is, integrated over all frequencies, the net flux at every depth zone is constant. For an isolated object with no incident radiation, the emergent flux is equivalent to this net flux. (This, of course, is not true for irradiated objects such as EGPs.)

When modeling atmospheres of EGPs without evolutionary models, one must make reasonable assumptions about the inner boundary. One may choose an inner boundary flux based on the evolutionary models of isolated objects (Burrows et al. 1997). Such a choice would provide the correct intrinsic luminosity of the EGP in isolation, assuming its mass and age are known. While this may provide a good approximation in some cases, such an approach ignores the fact that the interior and atmosphere are inexorably coupled, and so an incident flux will affect the interior and the evolution of the object as a whole (Burrows et al. 2000). For heavily irradiated objects, strong horizontal winds are expected, and it has been suggested recently that even a small vertical component can transport kinetic energy to the interior, acting as an additional heat source (Guillot & Showman 2002).

Since deciding upon the inner boundary condition for an atmosphere model is obviously not a trivial task, it is important to explore the variation in the emergent spectrum and T-P structure as a function of the inner boundary flux. Using a Class IV EGP model (a cloud-free version of 55 Cancri b), we investigate the effects of varying this flux by up to 5 orders of magnitude. Figure 16 shows the EGP T-P structures for inner boundary fluxes ($= \sigma T_{\rm eff}{}^4$) corresponding to $T_{\rm eff}=$ 1000 K (top curve), 750 K, 500 K, 300 K, 150 K, and 50 K (bottom curve). The dashed portions of the curves indicate the convective regions. At pressures greater than ~ 1 bar, each of these profiles is substantially different. Clearly, the T-P structure in the deepest regions is determined by the chosen inner flux. However, at pressures of less than a bar, only the 1000 K and 750 K models deviate significantly from those with lower temperature inner boundary fluxes.

The emergent spectra associated with these models are depicted in Figure 17. The lowest curves (300 K, 150 K, and 50 K; overlapping at the bottom) are nearly identical, indicating that below 300 K, the inner boundary condition ceases to have any noticeable effect on the emergent spectrum of an object as hot as Class IV. The 500 K boundary model is also very close to these lower temperature models at most, but not all wavelengths, with the most significant deviations appearing in the flux peaks between ~ 0.8 and 1.4 μm. The 750 K and 1000 K models have higher fluxes than the other models at most wavelengths. Still, the ~ 5 dex increase in the inner boundary flux between the 50 K model and the 1000 K model translates to well under a 1 dex difference in the emergent spectrum at most wavelengths.

6.2. Effects of Surface Gravity

Since only the minimum masses of most EGPs are known, and their radii are given only by theoretical models, the surface gravities of EGPs are problematic. In this subsection, we explore the dependence of the T-P structure and emergent spectrum on surface gravity, which is an input to the atmosphere models.

An estimate of the minimum surface gravity for most objects can be made by assuming a radius close to that of Jupiter, or more accurately, obtaining the radius from evolutionary models of isolated objects. Statistically speaking, upper limits can be estimated crudely by noting that the actual mass of an EGP should rarely be more than a factor of 3 or 4 greater than its $M_p \sin(i)$. Otherwise a clearly disproportionate number of detected EGPs would be nearly face-on. But no degree of certainty for a given EGP can be claimed without accurate astrometry or the fortuitous transit of a primary by the EGP. The only certain case presently known is HD 209458b. As a low-mass roaster, HD 209458b has a particularly low surface gravity (~1 g). For the majority of EGPs, regardless of their proximity to their central star, surface gravities are rather poorly constrained. Hence, a parameter study on gravity is useful.

Using a Class III EGP model, we vary the surface gravity from 10^3 to 3×10^5 cm s^{-2} (large) in steps of 1/2 dex. Figure 18 depicts the resulting T-P profiles. (The top curve is the lowest gravity model.) Increasing the gravity by 1/2 dex increases the pressure at a given atmospheric temperature by roughly 1/2 dex as well, as one could estimate from hydrostatic equilibrium. Of course, since compositions and opacities vary with pressure and temperature, this problem is not merely one of hydrostatic equilibrium, but such simple arguments hold reasonably well. Since the surface gravity varies roughly in concert with the mass (the radius does not vary too strongly with mass), a 1/2 dex uncertainty in the mass of an EGP might correspond to the differences between two adjacent T-P profiles in Figure 18.

The associated emergent spectra for these models are shown in Figure 19. For these Class III models, an increase in gravity results in a general decrease in flux shortward of ~2.2 μm, and an increase longward. Additionally, a larger gravity tends to reduce the peak-to-trough variations throughout the spectrum. While there certainly are some large differences between the 10^3 and 3×10^5 cm s^{-2} (a massive brown dwarf) models, a 1/2-dex difference in surface gravity produces a relatively small difference in the emergent spectrum.

6.3. Effects of Condensate Particle Size

The scattering and absorption of radiation by condensates is a wavelength-dependent function of particle size. Here, we vary the median particle size for a water cloud size distribution to investigate the effects on the emergent spectrum of the Class II EGP, ϵ Eridani b.

Our fiducial median particle size for ϵ Eridani is 5 μm. For two other models, we use median sizes of 0.5 μm and 50 μm. The effects on the visible and near-infrared emergent spectrum are shown in Figure 20 along with a cloud-free spectrum of the planet (bottom curve). The 0.5-μm model (top curve) produces the most reflection, followed by the 5-μm model, and then the 50-μm model. The cloud-free model visible and near-infrared fluxes are substantially lower because Rayleigh scattering alone provides limited reflection with increasing wavelength. In the visible, the three cloudy models differ by less than a factor of 2 at any given wavelength. However, in the infrared J and H bands the variation is significantly larger, with the 0.5-μm and 50-μm models differing by roughly an order of magnitude. The effects out to 30 μm are depicted in Figure 21. The cloudy models simply do not differ much beyond the near-infrared. However, each of the cloudy models does differ from the cloud-free model in the 4-5 μm opacity window by up to two orders of magnitude. The clouds act to close off the opacity window, blocking radiation from the deeper atmosphere, which can escape through this window in the cloud-free case. This is reminiscent of Jupiter, in which ammonia clouds block the M band flux, which emerges only through the clear gaps between the cloud bands.

In general, different condensate particle sizes will translate into significant differences at some wavelengths. However, such differences are unlikely to rival the differences between cloud-free and cloudy EGP models.

7. SPECIFIC THEORETICAL MODELS FOR KNOWN EGP SYSTEMS

Models of specific EGP systems will prove to be invaluable both to inform observational surveys and in the interpretation of the resulting data. Like any subfield of astrophysics, the accuracy and improvement of EGP models will in part depend upon the availability of observational data to constrain the rich variety of consistent theoretical models that are possible. At this early stage, assumptions must be made with respect to metallicities, gravities, inner boundary fluxes, cloud scale heights, cloud particle sizes, etc. When modeling a specific EGP system with some well-measured parameters (semimajor axis, stellar spectral type, etc.), we choose one set of values based on the available data. (We explored the effects on the emergent spectra and T-P structures of variations in some of these parameters in §5.) Some aspects, such as cloud patchiness and atmospheric winds, are not tackled in the current modeling effort. Furthermore, we do not attempt to model the complex photochemistry of nonequilibrium species that are likely produced by the ultraviolet irradiation of molecules in the outermost atmospheres of EGPs.

To date, there are roughly 100 known EGPs. We model a representative sample of these that encompasses a full range of EGP atmospheric temperatures and angular separations. A broad set of Kurucz model stellar spectra (Kurucz 1994) is utilized to simulate the central stellar spectrum for each planetary system modeled. These spectra are scaled and normalized using the measured effective temperatures and gravities of the actual stars (Santos et al. 2001; Ryan 2001).

For the purpose of modeling the atmospheres and emergent spectra of these objects, the mass and age determine the intrinsic luminosity and, hence, the inner boundary flux. Unfortunately, we know neither the actual planetary masses nor the ages of most of the EGPs discovered to date. We do know the minimum planetary masses, as given by the radial velocity method ($M_p\sin(i)$), but we do not know the orbital inclination (i) for most systems. Only with a transit (*e.g.* HD 209458b) or an astrometric measurement (*e.g.*, ϵ Eridani, Gatewood 2000) can we discern the inclination and mass. The ages are difficult as well. Detailed spectroscopy of the central star may result in an estimated age, but such work has yet to be completed for most systems. The inner boundary is of little consequence to the emergent spectra of closely orbiting EGPs so long as the inner flux corresponds to $T_{\rm eff}\lesssim500$ K, but it can be quite important in the modeling of planets with larger orbital distances. We use $M_p\sin(i)$ and, where available, estimates of the primary's age along with evolutionary models (Burrows et al. 1997) as guides to our chosen inner boundary fluxes. In all cases, we'll state what inner boundary condition is used.

7.1. The Upsilon Andromeda System

The Upsilon Andromeda system (Butler et al. 1999) is currently known to be comprised of three EGPs in orbit around an F8 main sequence star of distance $\sim$ 13.5 parsecs. The innermost planet (υ And b) has an $M_p\sin(i)$ of $0.71M_{\rm J}$ and is in a roughly circular orbit ($e\sim0.03$) about its primary at only 0.059 AU. υ And c is somewhat more massive ($M_p\sin(i)$ = 2.11 $M_{\rm J}$) and has an elliptical orbit ($e\sim0.2$) with a semimajor axis of 0.83 AU. With $M_p\sin(i)$ = $4.61M_{\rm J}$, υ And d is even more massive and has a semimajor axis of 2.50 AU. It has a significant eccentricity of $\sim$ 0.4, so its periastron is actually 1.5 AU and its apastron is 3.5 AU. Since we do not currently know the inclinations of their orbits, we know only the minimum masses of these planets. However, if we assume that the orbits are roughly coplanar, as indicated by our own solar system and the theory of planet formation, the ratios of the $M_p\sin(i)$ are also the ratios of the planetary masses.

The emergent model spectra for the planets in the Upsilon Andromeda system, along with an estimated spectrum of the primary (a scaled Kurucz model stellar spectrum), are shown in the upper panel of Figure 22. The

T-P profiles of these planets are depicted in Figure 23.

Upsilon And b is a Class V "roaster" with silicate and iron clouds high in the atmosphere. We choose a cloud particle size distribution that is peaked at 10 microns for both forsterite and iron. Each of these clouds has a vertical extent of one pressure scale height. The iron cloud base resides at ∼20 mbar, while the forsterite condenses at slightly lower pressures (∼10 mbar). Given the prescribed vertical extents of these clouds, they overlap spatially. At pressures where the condensation curves of forsterite and iron are relatively close, as in this case, one might reasonably argue that a number of species from the olivine sequence, in addition to forsterite, could form (as discussed in §3.2). For this reference model of υ And b, we do not include such species. The mixing ratio of the condensed forsterite is set equal to the elemental mixing ratio of magnesium ($\sim 3.2\times10^{-5}$). Similarly for the iron cloud, the condensate is assumed to consume all the iron (mixing ratio $\sim 5.4\times10^{-5}$).

The lower panel of Figure 24 is a comparison of the T-P profile of a cloud-free version of υ And b (thin curve) with that of our fiducial model (thick curve). Both models have a lower boundary flux equal to that of an isolated object with $T_{\rm eff}=$ 500 K and a surface gravity of 3×10^3 cm s^{-2}. The primary effect of removing the clouds is a somewhat lower temperature in the outer atmosphere (P $\lesssim$ 0.1 bar) and a slightly hotter atmosphere deeper (P $\gtrsim$ 0.1 bar). At large depth, in the convective region (P $\gtrsim$ 50 bars), these high clouds appear to have essentially no effect. A comparison of the fiducial spectrum (thick curve) and cloud-free spectrum (thin curve) is depicted in upper panel of Figure 24. The removal of the clouds results in a wider variation from peak to trough throughout most of the spectrum. This is expected to be the case because condensates produce relatively gray extinction in comparison with strongly wavelength-dependent gaseous absorption. In this same vein, the removal of the clouds somewhat deepens the sodium resonance line.

While the presence of clouds in υ And b (and other roasters) has significant effects on its T-P structure and emergent spectrum, these effects are not so drastic as those predicted in hot EGPs by some researchers, such as Barman, Hauschildt, & Allard (2001, BHA). The main differences are the vertical extent of the clouds and the cloud particle sizes. Our clouds have a finite scale height like those observed in Earth's atmosphere and in the atmospheres of other planets in our Solar System. BHA use a "dusty" model in which the condensates extend to the lowest pressure of their atmosphere model, an assumption that was also made by SWS. Furthermore, BHA assume that a large number of condensates form at these very low pressures, including (in addition to forsterite and iron) enstatite, spinel, diopside, akermanite, and others. As detailed in §3.2, some of these species should not form because one or more of their elements will be consumed by a condensate that forms at higher temperature. Furthermore, gravitational settling should prevent any such species from remaining suspended at such low pressures (∼ 1-10 microbars). BHA suggest that the nature of their treatment of clouds provides an upper limit to the effect of clouds in EGP atmospheres.

The other difference between our cloud layers and those of BHA is approximately two orders of magnitude in the cloud particle sizes. BHA assume an interstellar size distribution. We have been guided in our choice of particle size (10 μm) by the work of Cooper et al. (2002) and Ackerman and Marley (2001).

Upsilon And c is a Class III EGP. That is, no principal condensates are expected to appear in its outer atmosphere. Since it is more massive than υ And b, we have chosen a higher surface gravity of 10^4 cm s^{-2}. Using evolutionary models (Burrows et al. 1997) as a guide, we have chosen an inner boundary flux to be equivalent to that of an isolated of object with $T_{\rm eff}=$ 200 K. Its much larger orbital distance and lack of condensates to reflect incident radiation result in a flux that is a few-to-several orders of magnitude lower than that of υ And b. However, in the 4-5 μm region, a lack of opacity reduces this difference to only 1-2 dex.

Upsilon And d contains condensed H_2O in its outer atmosphere, and so it is a Class II EGP. It's $M_p\sin(i)$ is roughly twice that of υ And c, so we have chosen a surface gravity of 2×10^4 cm s^{-2} and a lower boundary flux of $T_{\rm eff}=$ 250 K. Its semimajor axis is three times that of υ And c, yet its flux at Earth is actually larger at some wavelengths shortward of 2 microns. This due to the fact that scattering by the condensate reduces the depths of the molecular absorption features. In the windows between these features, υ And c still has the higher flux. The rather large eccentricity ($e\sim0.4$) of υ And d means that its atmospheric temperature will vary from periastron to apastron. At periastron, it is likely that its outer atmospheric temperature will be too high for water to condense, rendering υ And d a Class III object, like υ And c. At apastron, the water clouds of our fiducial model will reside somewhat deeper and will have a greater column and optical depth.

The lower panel of Figure 22 shows the visible and near-infrared phase-averaged contrast between the planetary and stellar fluxes for υ And b, c, and d. Again, this quantity is an average of the planetary flux emerging into all solid angles divided by the stellar flux (uniform in solid angle) at the same distance from the system. In each case, a planetary radius equal to that of Jupiter is assumed. For υ And b, the planet-to-star flux ratio is greater near 4 μm, where it approaches 3×10^{-4}. For comparison, it is worse than 10^{-5} throughout the visible. For υ And c and d, the planet-to-star flux ratio is greatest in the $\sim$ 4.1 to 4.8 μm range, where it is $\sim10^{-5}$ and 3×10^{-6}, respectively. Elsewhere, it is below 10^{-6} (below 10^{-8} throughout most of the visible). Since these numbers are based on a phase-averaged ratio, they are a bit pessimistic compared with what one would expect to observe at full phase, which could improve the ratios by over a factor of two, depending upon the details of the planetary phase function (Seager et al. 2000). Note that due to the large $M_p\sin(i)$ of υ And d and the correspondingly higher inner boundary flux, its spectrum in the near-IR Z, J, H, and K bands is brighter than that of an old, lower-mass EGP at the same distance (see §6 and Figs. 13 and 14).

7.2. The Transiting Planet, HD 209458b

HD 209458b was discovered by the usual radial velocity method (Henry et al. 2000; Mazeh et al. 2000) to be orbiting with a semi-major axis of only 0.045 AU ($e\approx0$)

around a G0V star, but subsequent dramatic photometry (Charbonneau et al. 2000; Henry et al. 2000) revealed that it transits its primary. At the time of this writing, HD 209458b is still the only transiting EGP certain to exist (there are several candidates currently under analysis). However, transits should not be very rare for Class V roasters. A transit will be observed if the inclination of a planet's orbit (i) is greater than $\cos^{-1}[(R_* + R_p)/a]$, where R_* is the stellar radius, R_p is the planetary radius, and a is the orbital distance of the planet. For roasters like HD 209458b, this corresponds to an inclination greater than ~84 degrees. HD 209458b-like systems with a random distribution of inclinations on the sky should transit approximately 10% of the time [5]. Of course, such a fortunate orientation immediately reveals the mass of the planet. A good estimate of the radius of the planet can be obtained from the photometric transit depth, since the percentage decrease in the stellar flux is approximately given by $(R_p/R_*)^2$. With a mass of $0.69 M_{\rm J}$ (Mazeh et al. 2000; Cody & Sasselov 2002) and a radius of $1.35 R_{\rm J}$, HD 209458b has a surface gravity of $\sim$ 980 cm s^{-2}.

A Class V roaster, the atmosphere of HD 209458b is expected to have high silicate and iron clouds with bases at $\sim$ 5-10 mbar. Our fiducial model has a surface gravity of 980 cm s^{-2} and an inner boundary flux corresponding to $T_{\rm eff}$= 500 K. Figure 25 depicts our HD 209458b model spectrum and an assumed spectrum for the primary (a scaled Kurucz model; upper panel). Additionally, the phase-averaged planet-to-star flux ratio is shown in the lower panel of this figure. The T-P profile of HD 209458b is depicted in Figure 26. As with υ And b, the planet-to-star flux ratio is large near 4 μm, where for HD 209458b it approaches 10^{-3}. The sodium and potassium absorption keeps the ratio low in the visible, but between the resonance lines ($\sim$ 0.7 μm) the ratio is approximately 3×10^{-5}, as it is blueward of the sodium line near 0.4 μm. One caveat is that nonequilibrium photochemical products (not included in these calculations) might absorb strongly in the ultraviolet and blue regions of the spectrum (cf. Jupiter), so the contrast at such short wavelengths is quite uncertain for HD 209458b and other roasters.

Recent landmark observations of the HD 209458b transit by Charbonneau et al. (2002) in the vicinity of the Na-D doublet reveal a photometric dimming in this region of the spectrum relative to adjacent bands. This has been interpreted as the first detection of sodium in the atmosphere of an EGP (and, importantly, the first detection of an EGP atmosphere) and it is in general accord with theoretical predictions (Hubbard et al. 2001; Seager & Sasselov 2000). However, the level of absorption inferred is less than what one would expect from basic theoretical models that assume a solar abundance of sodium in neutral form and no clouds. It should be pointed out that the transit spectrum and the emergent phase-averaged spectrum are in general different. The transit spectrum samples to a greater degree the characteristics of the planetary limb and terminator. The emergent spectrum is a whole-body quantity. As a result, differences between transit spectra for different models do not translate into corresponding differences in the phase-averaged emergent spectrum.

In their model for HD 209458b, BHA assume that heavy metals such as Mg, Ca, and Al exist in gaseous form in its outermost atmosphere. Their justification for the presence of these metal gases at low pressures is their particularly hot T-P profile, which is above the condensation temperatures of forsterite, enstatite, gehlenite, and other condensates that would sequester and rain out these metals if the outer atmosphere were somewhat cooler. In fact, our fiducial model for HD 209458b is several hundred degrees Kelvin cooler in the outermost atmosphere, leading us to conclude that when account is taken of the condensation and rainout of metal-rich refractories, the outer atmosphere should indeed be cooler and clear of these metals. In this regard, our general model results jibe with the work of others on close-in EGPs (Seager et al. 2000; Goukenleuque et al. 2000).

7.3. Orbiting a Cool Star: The GJ 876 System

The GJ 876 system (a.k.a. Gliese 876)(Marcy et al. 1998; Delfosse et al. 1998) is comprised of two planets orbiting at 0.13 AU and 0.21 AU about a late main sequence star of spectral type M4. The more massive and first of the two planets discovered, GJ 876 b ($M_p \sin(i) = 1.89 M_{\rm J}$), has the wider orbit (with $e \approx 0.10$), while GJ 876 c ($M_p \sin(i) = 0.56 M_{\rm J}$) has the more eccentric orbit ($e \approx 0.27$).

GJ 876b and c are both Class III planets because their temperatures are too cool for a silicate layer to appear in the troposphere, but too hot for H_2O to condense. The result of such a "clear" atmosphere is a strongly wavelength-dependent emergent spectrum, which is governed largely by the gaseous molecular absorption bands of water, methane, and ammonia. Given their similarities in composition, GJ 876b and c are expected to have very similar spectra. The factor of $\sim$ 3 difference in their $M_p \sin(i)$ implies somewhat different surface gravities and lower boundary fluxes, but both objects are close enough to their star that the T-P structure in their outer atmospheres is determined more strongly by the stellar irradiation than by their intrinsic luminosities.

For GJ 876b, we use an inner boundary flux corresponding to $T_{\rm eff}$= 150 K and a surface gravity of 6×10^3 cm s^{-2}. For GJ 876c, we use an inner boundary flux corresponding to $T_{\rm eff}$= 100 K and a surface gravity 1/3 that of GJ 876b, or 2×10^3 cm s^{-2}. The emergent spectra of the two planets, along with an assumed spectrum of the primary (a scaled Kurucz model stellar spectrum), are shown in Figure 27 (upper panel). Figure 26 depicts the planetary T-P profiles. Given their similarities in composition, GJ 876b and c are expected to have very similar emergent spectra. One caveat is that, while the T-P profile of GJ 876b never crosses the water condensation curve, it does come within $\sim$ 10 K of it near about 1 mbar. Given somewhat lower incident irradiation than that of our scaled Kurucz model for GJ 876, or given an observation of GJ 876b at apastron, some water condensation may occur in its outermost atmosphere, rendering it a Class II EGP. However, we retain the Class-III designation for our fiducial model of GJ 876 b for its given semimajor axis and any reasonable range in surface gravity or lower boundary flux. The lower panel of Figure 27 depicts the phase-averaged planet-to-star flux

[5]The integrated probability for a system to be between 0 and i degrees ($P[0^o,i]$) is just 1-cos(i), while $P[i,90^o] = \cos(i)$.

ratios for GJ 876b and c. For both planets, this ratio peaks near 4.4 μm, where it reaches a value of $\sim 10^{-5}$. In contrast, in the visible region, the M-dwarf primary flux overpowers that of either planet by a factor of at least 10^8.

7.4. 51 Pegasi b and Tau Bootes b

In 1995, Mayor & Queloz discovered the first EGP, 51 Pegasi b ($M_p \sin(i) = 0.45\ M_J$), via the radial velocity method. The discovery of such a planet around another star would alone cause a great deal of excitement in the astronomical community, but the fact that its orbital period was only 4.23 days at a minuscule 0.05 AU was nothing less than astonishing. Perhaps the fact that this planet orbited a solar-type star made the observation even more dubious to some. After all, this is a much different beast than the giant planets of the Solar System we know. The 51 Peg b observation is not due merely to non-radial stellar pulsations (Gray 1997; Gray & Hatzes 1997), nor is the radial velocity variation due to a nearly face-on orbit of two identical stars (Black & Stepinski 2001; Stepinski & Black 2001). And although 51 Peg b remains to be detected directly, almost everyone in the astronomical community now accepts it and the other roasters as bona fide planets.

The τ Boo system (Butler et al. 1997) gained popularity when Cameron et al. (1999) claimed a detection in reflected light near 0.48 μm. This detection was not confirmed by Charbonneau et al. (2000), who constrained the albedo to be low in this region ($\lesssim 0.3$ assuming a phase function and a highly inclined orbit). If Cameron's detection were true, τ Boo b would have had an albedo as high as that of Jupiter in this region and a troubling radius of $\sim 1.8 M_J$ — troubling because such a large radius would be well out of bounds relative to theoretical models for a high gravity planet (Guillot et al. 1996; Burrows et al. 2000). This detection was later retracted by the authors, but τ Boo b remains a particularly interesting object because, with $M_p \sin(i) = 4.09\ M_J$, it is more massive than most of the other roasters known.

Since they orbit their primaries so closely, 51 Peg b and τ Boo b are both Class V roasters, but these systems do differ. 51 Peg b orbits a G2-2.5V Sun-like star at 0.05 AU, while τ Boo b orbits a hotter F7V star at 0.046 AU. Additionally, their projected masses differ by about a factor of 10.

As the prototype EGP, 51 Peg b has been modeled by a number of researchers (Seager & Sasselov 1998; Goukenleuque et al. 2000; BHA) and the model T-P structures and emergent spectra vary considerably. In all cases, a self-consistent planar atmosphere code is used. Perhaps the greatest difference is between the models of Goukenleuque et al. and BHA. Specifically, BHA's atmospheric temperature at P = 1 mbar is above 1650 K ("AMES-Cond" model; cloud-free), while that of the most analogous Goukenleuque et al. model is under 900 K. At P = 1 bar, the temperature of the BHA model is ~ 2000 K, while that of Goukenleuque is ~ 1400 K. To first order, this difference can be explained by the fact that Goukenleuque et al. redistribute the incident power over the surface of the full sphere (weighting the incident flux by a factor of 1/4, as described in §2), while BHA treat only the substellar point of the planetary atmosphere (no weighting of the incident flux).

In order to investigate the dependence of the T-P structure using our own models, we ran a cloud-free 51 Peg b model with no flux weighting, one with a weighting of 1/4, and one with a weighting of 1/2. The flux weighting of 1/2 corresponds to the irradiation of the day-side hemisphere only, the default weighting used in the present work. The resulting T-P profiles are depicted in Figure 28. For our 1/4-weighted model, the atmospheric temperature at 1 mbar is 965 K, and at 1 bar it is 1830 K. For our unweighted model, the temperature at 1 mbar is 1390 K, and at 1 bar it is 2370 K. So for our models, this difference in the flux weighting results in a 35% difference in the temperature at 1 mbar and a 25% difference at 1 bar. The difference between the Goukenleque et al. and BHA models at 1 mbar is 60%, while at 1 bar this difference is a more modest 35%. Hence, while differences in the incident flux weighting can in part explain the differences in the T-P structures of published models, such differences are not a complete explanation. Other less obvious differences must exist as well, such as atmospheric composition, opacities, incident flux (beyond the weighting issue), or the inner boundary condition implemented.

Our fiducial model of 51 Peg b has a silicate (forsterite) cloud base at 20 mbar and an iron cloud base at 30 mbar. we assume a cloud height of one pressure scale height, an inner boundary flux of $T_{\rm eff} = 500$ K, and a low surface gravity of 10^3 cm s^{-2}, due to the small $M_p \sin(i)$ (0.44 M_J) of 51 Peg b. In order to achieve numerical convergence of the 51 Peg b model, we found it necessary to attenuate the clouds to 10% of the elemental iron and magnesium abundances. This should be taken into account when comparing the T-P structure and emergent spectrum of 51 Peg b with those of other roasters, for which such an adjustment to the condensate concentration has not been made.

Tau Boo b (Butler et al. 1997) orbits at only 0.046 AU from a hot F7 main sequence star. For our fiducial τ Boo b model, we use a surface gravity of 10^4 cm s^{-2} (an order of magnitude larger than that used for 51 Peg b) and an inner boundary flux of $T_{\rm eff} = 500$ K. As can be seen in Figure 29, the T-P profiles of τ Boo b (both with and without clouds) and 51 Peg b are fairly similar, especially considering their very different surface gravities and primary spectral types. This can be explained quite simply: the same object orbiting a hotter star naturally would have a higher temperature at a given pressure, but on the other hand, hydrostatic equilibrium dictates that pressure increases with surface gravity. So in this case, the two effects work against each other, resulting in T-P profiles that are actually closer to each other in some regions than they would be if either the surface gravities of the two planets were the same, or if the planets orbited similar stars. Gravity and temperature also have implications for the positions of cloud decks in these and other atmospheres. A cloud deck will reside deeper in an atmosphere as surface gravity increases, but higher in an atmosphere with increasing temperature. For 51 Peg b and τ Boo b, the profiles are so close that they are coincident with the condensation curves at essentially the same pressures. As a result, these planets should condense clouds at very similar atmospheric pressures.

The atmosphere model of τ Boo b is particularly interesting because it has a convection zone at low pressures, toward the top of the forsterite cloud around 10 mbar. This is the only model for which such a low-pressure convective region has resulted, and it persists with either fine or coarse zoning within the cloud region. The strong incident flux from the primary (F7V at 0.046 AU) in combination with the opacity of the forsterite cloud results in a steep temperature gradient and, hence, the onset of convective energy transport, as depicted by the dashed portion of the T-P profile of τ Boo in Figure 29. The model spectra of τ Boo b and 51 Peg b, and their planet-to-star flux contrasts, are shown in Figure 30. These spectra are characteristic of those in Class V described in §5.5.

7.5. The 55 Cancri System and its Long-Period Planet

The 55 Cancri system is made up of at least two EGPs orbiting a G8 main sequence star. The inner planet (Butler et al. 1997) has a nearly circular orbit ($e \approx 0.03$) at 0.11 AU, with $M_p\sin(i) = 0.84 M_J$. The recently discovered outer planet (Marcy et al. 2002) is the first EGP found to orbit its primary at a distance greater than Jupiter's distance from the Sun. This object has a semimajor axis of $\sim$ 5.5 AU, an eccentricity of 0.16, and $M_p\sin(i)$ of $4.0 M_J$. The outer object has been designated, 55 Cancri d (rather than c), because judging by the radial velocity residuals, a third planet of sub-Jupiter mass may exist at 0.24 AU. Currently, Marcy et al. consider the existence of this third planet to be a good possibility, but not a firm detection because the additional periodicity may be due to rotating inhomogeneities on the stellar surface.

55 Cancri b is a Class IV planet. Our fiducial model of this EGP assumes a surface gravity of 3×10^3 cm s^{-2} and an inner boundary flux of $T_{\rm eff} = 500$ K. A silicate cloud resides at depth, with a base at 20 bars and a vertical extent of one pressure scale height. As detailed in §5.4, this deep cloud does not have a significant effect on the emergent visible and near-infrared fluxes of 55 Cnc b.

55 Cancri d is a Class II object. One might estimate that, with an orbital distance greater than that of Jupiter and a primary cooler than our Sun, 55 Cnc d would be a Jovian-like Class I object with ammonia clouds. However, because of its large minimum mass, such a planet will be intrinsically hotter than Jupiter, even for a relatively late age (Burrows et al. 1997). With a conservative inner boundary flux corresponding to $T_{\rm eff} = 150$ K, the atmosphere of 55 Cnc d is too warm for ammonia to condense.

Figure 31 depicts the spectra of 55 Cnc b and d and their planet-to-star flux contrasts, while Figure 32 shows the T-P profiles of these planets. The Class IV designation of 55 Cnc b is manifest, due to its strong sodium and potassium resonance features and the methane absorption at 3.3 μm. The spectrum of 55 Cnc d exhibits strong molecular absorption features in the visible and near-infrared, but a water cloud between $\sim$ 0.6 and 1.6 bars (one pressure scale height) reduces the strengths of these features considerably. Note that this water cloud is deeper and more optically thick than that in the atmosphere ofυ And d (§7.1) simply because the T-P profile of 55 Cnc d intersects the water condensation curve at significantly higher pressure. However, whether a water cloud is high and optically thin or relatively deep and optical thick, the basic result of an elevated visible and near-infrared spectrum holds.

Figure 33 shows the phase-averaged planet-to-star flux ratios for 55 Cnc b and d out to 30 microns. 55 Cnc d has an unusually large angular separation from its primary of $\sim 0.45''$, making it an enticing candidate for direct detection. A good bet may be between 4.2 and 4.8 μm, where there is little opacity and the planet-to-star flux ratio is better than 10^{-6}. Between $\sim$5 and 6 μm, the methane, water, and ammonia opacities strengthen, but beyond a strong methane band between $\sim$7 and 8 μm, the planet-to-flux ratio improves substantially. There are a number of striking differences between 55 Cnc b and d. In the visible region, the strong sodium and potassium lines of 55 Cnc b contrast with the methane-dominated spectrum of 55 Cnc d, whose continuum is provided by both Rayleigh scattering and scattering off condensed H_2O. In the near-infrared, the troughs and peaks of 55 Cnc d (due to gaseous H_2O and methane) vary more widely than those of 55 Cnc b. This effect can be explained largely by H_2O opacity differences at high and low temperatures. Additionally, the methane opacity is stronger in the lower-temperature 55 Cnc d due to a higher equilibrium abundance of this molecule. Between $\sim$ 4 and 5 microns, CO opacity in 55 Cnc b closes the gaping opacity window seen in the 55 Cnc d spectrum. Toward longer wavelengths, the 55 Cnc d planet-to-star flux ratio continues to increase through 30 μm, while that of 55 Cnc b is fairly flat.

7.6. Some Other EGPs of Interest

In addition to the systems chosen above, many more deserve specific attention due to their interesting orbital parameters, masses, primaries, and/or proximity. We model a few of these in the present work, including HD 114762b, ϵ Eridani b, and HD 83443b.

The massive HD 114762b (Latham et al. 1989) is often referred to as a brown dwarf, not a planet. It has a projected mass of $11 M_J$ (Marcy et al. 1998), and its mass has been estimated to be as high as $145 M_J$ (Han et al. 2001), which of course would make this object a low-mass star, but this result is quite controversial. Whatever its mass, HD 114762b orbits its F9V primary at a distance of $\sim$ 0.3 AU with an eccentricity of 0.335. The spectrum out to 5 μm of our fiducial HD 114762b model (inner boundary flux of 500 K, surface gravity of 10^5 cm s^{-2}) is shown in Figure 34.

Epsilon Eridani b is a controversial, but potentially very important, EGP because of its wide orbit around a star that is only 3.2 parsecs away from Earth. If it is real, its separation from its K2V primary is $\sim$ 1 arcsecond, significantly larger than that of any other known system. The radial velocity detection of ϵ Eri b (Hatzes et al. 2000) is considered marginal by many, but its orbital parameters are $M_p\sin(i) = 0.86\ M_J$, $a = 3.3$ AU, and $e \sim 0.61$, a very eccentric orbit. This system is probably under 1 Gyr of age (Greaves et al. 1998), indicating that ϵ Eri b is quite a bit warmer than Jupiter if its mass is $\sim 1 M_J$. Indeed, an astrometric study claimed a mass of 1.2 $\pm$0.33 M_J (Gatewood 2000). Using a fiducial lower boundary flux corresponding to $T_{\rm eff} = 170$ K and a gravity of 3×10^3 cm s^{-2}, ϵ Eri b is a Class II EGP. The resulting spectrum and planet to star flux ratio from 0.4 to 30 μm are shown in Figure 35. A water cloud resides at $\sim$1 bar pressure in ϵ Eri b's atmosphere, but given the large eccentricity of this EGP, the cloud will be deeper in the atmosphere at apastron and higher at periastron. Even at apastron, it is unlikely that the atmospheric temperature will be low enough for ammonia to condense. In fact, an atmosphere model for ϵ Eri b at 5.3 AU indicates that the T-P profile falls just short of the ammonia condensation curve.

HD 83443b (Mayor et al. 2000) is a Saturn-mass ($M_p\sin(i) = 0.35M_J$) planet with the smallest orbital distance of any EGP known to date. However, unlike most known roasters, HD 83443b orbits a later-type main sequence star (K0V). Therefore, despite its status as the most closely-orbiting roaster, it is a little cooler than its brethren. Because it is cooler, its silicate and iron clouds are somewhat deeper than in most roasters. In our fiducial model, the silicate (forsterite) cloud resides at $\sim$ 30 mbar and an iron cloud is located near 100 mbar. We use a lower boundary flux corresponding to $T_{\rm eff}$= 500 K and a gravity of 900 cm s^{-2}. Initially, due to radial velocity residuals, this system was believed to have another planet orbiting at 0.174 AU, with $M_p\sin(i) = 0.17M_J$. However, follow-up measurements failed to reveal such a planet (Bulter et al. 2002).

Figure 34 depicts the visible and near-infrared spectra of HD 83443b, HD 114762b, and ϵ Eri b, and their planet-to-star flux contrasts. The T-P profiles for each of these objects are given in Figure 36.

8. DETECTION AND IMAGING OF EGPS IN LIGHT OF THEORETICAL MODELS

A number of very innovative ground-based and space-based methods are now under development, or under serious consideration, to detect EGPs directly. Theoretical models have had and will continue to play an important role in guiding observational campaigns. This section reviews some of the many observational methods and their prospects for success in light of our theoretical models. Where available, instrumental sensitivities are used in combination with spectral models to reveal which of the currently known EGPs are likely to be detectable in the near term.

The central problem in direct imaging, photometric phase detection, and spectral separation methods is the huge contrast between the central star and its companion(s). The tiny planet-to-star flux ratios and minuscule angular separations require observers and instrumentalists to develop very clever detection methods. Space-based instrumentation has a clear advantage due to the absence atmospheric turbulence, but these missions are costly and will not be in operation for several years. Hence, a plethora of ground-based techniques are already in use or in the advanced stages of development. Many of these techniques are limited by the angular separation of the planet from the primary, whose maximum value is given by a/D, where D is the distance from the Earth. Table 1 lists the maximum angular separations at the Earth of the EGPs studied in this paper, along with those of others with the greatest separations. The objects on this list will be some of the most important targets during the coming decade of direct EGP research.

8.1. Spectral Separation Methods

The close-in EGPs, such as 51 Peg b or τ Boo b, are separated from their primaries by only 0.8–4 milliarcseconds. While direct imaging of such systems from the ground at any wavelength would be a great challenge, a radial-velocity-based spectral separation method is being used by some researchers (Cameron et al. 1999; Charbonneau et al. 2000). With knowledge of the radial velocity variation of the stellar absorption lines due the primary's orbit about the system's center of mass, one can also expect a time-dependent opposite shift of the component of the stellar spectrum that is reflected by the planet. By modeling and subtracting the radial velocity-dependent stellar spectrum, the reflected component of the stellar spectrum should be left in the noisy residuals. The great difficulty is the large contrast between the actual stellar spectrum and the reflected component.

The intensity of the reflected stellar component depends upon the albedo of the EGP, which for a Class V EGP tends to be highest in the visible region of the spectrum. At short enough wavelength (i.e., in the blue region of the spectrum), the thermal emission of even a Class V roaster is negligible. Hence, to a good approximation, all the flux in this region is reflected flux, so the wavelength dependence of the reflected stellar component can be derived by combining the stellar spectrum with the planetary albedo. According to our models, the phase-averaged planet-to-star flux ratio in this region is below 2×10^{-5} in all cases, and worse than 10^{-5} in some. When the planet is near full phase, these values may improve by a factor of 2-3, bringing the ratio into the vicinity of the detection limit of $\sim 0.5\text{-}1\times10^{-4}$ (Charbonneau et al. 2000; Cameron et al. 1999), although the velocity shift in the reflected component relative to the stellar spectrum approaches zero as the planet approaches opposition.

The difficulty of this method is illustrated by the false detection of τ Boo b, as discussed in §7.4. Yet, this technique may be our best hope for detecting a roaster in reflected light from the ground. Even if no detections are made, improvements in the accuracy of this method can provide upper limits to planetary albedos as a function of wavelength and orbital inclination, thereby putting soft contraints on the outer atmospheric compositions. However, the motivation and rationale for spectral separation methods will continue to be the detection of reflected light.

8.2. Ground-Based Differential Direct Imaging

Differential imaging entails the simultaneous imaging of a candidate system in two or more adjacent narrow band filters. The bandpasses are chosen so that at least one resides in a spectral region where a deep planetary absorption feature is expected, and another is situated in an adjacent opacity window, where the planet flux is predicted to be relatively large. However, the central star is bright in both bandpasses, so by imaging the candidate system and then differencing the two bandpass fluxes, one can subtract out the offending starlight, hopefully revealing the dim planet. Just how dim a planet can be detected depends on a number of parameters, including the angular separation, the telescope size, instrument design, filter bandpasses, and CCD efficiency.

One instrument design makes use of dual Wollaston prisms for image splitting using the Arizona Infrared Imager and Echelle Spectrograph (ARIES), the MMT 6.5-

meter telescope, and an adaptive optics (AO) secondary (Freed et al. 2002). With this set-up, on schedule for use in mid-2003, a 3σ detection in the H-band region is expected for an EGP-primary separation of $0.2''$ and planet-to-star flux ratio of $\sim 3\times10^{-6}$. For larger separations, the detectable flux ratio improves significantly. For example, at a $1''$ separation, the limit is $\sim 10^{-7}$ for a 2-hour exposure. These estimations are based on the placement of three narrow-band filters between 1.56 and 1.68 μm, toward the short-wavelength edge of a strong methane absorption feature. According to our models, none of the currently known EGPs will be detectable with this technique (given these sensitivities), since there are only a few with separations on the order of $\gtrsim 0.2''$ and their theoretical plant-to-star flux ratios are too low by 2-3 orders of magnitude. However, this method may succeed in discovering new, young Class III EGPs at 5-10^+ AU from their primaries.

Another similar instrument, TRIDENT, is optimized for the detection of EGPs with orbital distances greater than 5 AU in a narrow spectral region between 1.57 and 1.68 μm (Marois 2002). Using the CFHT 3.6-meter telescope with an AO system, a test observation was made of a faint companion $0.5''$ from its primary. In this case, the contrast ratio was $\sim 2\times10^{-4}$, a very easy detection relative to that of an EGP. However, this detection confirms that the basic technique does work, and plans to use this instrument on the Gemini 8.2-meter telescope are under way.

8.3. Transit Searches and Photometric Reflected Light Detection

EGPs that have highly inclined orbits from our vantage point have a high probability of transiting their stars. In particular, this is true of Class V roasters, for which the overall probability of a transit is approximately 10%, assuming a random distribution of orbital inclinations (§7.2). The resulting stellar photometric dimming of ∼1.5% is easily observable from the ground. This fact has led to an abundance of inexpensive ground-based transit searches far too numerous to discuss here. One such search, STARE (Brown & Charbonneau 1999), proved its worth with the detection of HD 209458b (see also Henry et al. 2002), the first and only verified transiting EGP to date. Like STARE, most other programs use small telescopes and monitor stars in an automated fashion. One search collaboration is OGLE (Udalski et al. 2002). Originally developed for the detection of optical gravitational lensing events in the galactic disk and bulge, OGLE has amassed an impressive collection of stellar light curves. Over 50,000 stars have been analyzed for variability due to a possible transiting planet (a light curve showing a flat-bottomed eclipse). For 42 of the stars, multiple transits were observed, and two of these may be close-in transiting EGPs given their short periods and photometric dimmings similar to that of HD 209458b (Udalski et al. 2002). Follow-up work, including a radial velocity determination of $M_p\sin(i)$ for these putative companions will be necessary to confirm their planetary nature.

In principle, one should be able to detect photometric variations for EGPs that do *not* transit their stars, due to differences in reflected light as a planet runs through its various orbital phases. The difficulty is that such variations are likely to be only a micromagnitude (μmag) to tens of micromagnitudes, depending upon the inclination of the orbit, the existence of high clouds, and their constituent condensates (Green et al. 2002; Seager et al. 2000). Such variations are too small to be observed from the ground, but several space-based missions are in the works, including MOST (Matthews et al. 2001), COROT (Antonello & Ruiz), MONS (Christensen-Dalsgaard 2000), and *Kepler* (Koch et al. 1998).

MOST is essentially complete and due for launch in April of 2003. This small, but very sensitive instrument, will be used for transit observations and for reflected light detection. MOST contains a 15-cm mirror and a single broad-band filter from 0.35 to 0.70 μm. An array of microlenses projects a large, stable image onto a CCD. Sensitivities are on the order of a few μmag, easily sufficient according to our models for the detection of Class V roasters with high enstatite clouds, which are quite reflective in the visible. However, if the clouds are buried and/or are composed of more highly absorbing species (such as forsterite), detection will be much more difficult. At the very least, MOST will constrain the outer atmospheric compositions of a number of close-in EGPs, but hopefully a few groundbreaking detections will be made.

COROT, scheduled for launch in 2005, will be capable of multicolor photometry. Its wide-field-of-view, 27.4-cm telescope is suitable for the simultaneous monitoring of many stars. Throughout its mission, 6,000-12,000 stars will be searched for transits by terrestrial and gas giant planets. Additionally, detections of reflected light from close-in nontransiting planets through blue and red bandpasses may be possible. Such observations could provide rudimentary color data for some EGP atmospheres.

Kepler has been selected as a NASA Discovery mission for the detection of transits by Earth-like planets, and it is scheduled for launch in 2006. A much larger instrument than MOST or COROT, Kepler has a 1.6-meter primary mirror and an array of 42 CCD detectors. It will monitor ∼100,000 stars in visible light for planetary transits. Hundreds of EGP transits are expected, and follow-up radial-velocity measurements will be possible for some of the closer systems. A determination of the planetary albedos of transiting planets should be possible by inferring a planetary radius from the transit depth, a semimajor axis from the period of the orbit, and the reflected light modulation between transits, because the fraction of reflected stellar light as a function of planetary phase can yield the albedo.

8.4. Interferometric Imaging

The precision of interferometry provides promising methods for the detection of EGPs. These include both astrometric and direct imaging techniques, which are being developed for both ground-based and space-based programs.

One of the most innovative methods is nulling interferometry, whereby the light from a star is strongly suppressed while that from a companion is not. A nulling interferometer is similar to a Michelson interferometer, except that the path lengths from a pair of collectors are purposely maintained at a difference of half a wavelength so that the light from the star interferes destructively. However, at a minuscule separation angle from the central star (perhaps at the position of a planetary companion), the phase relation for the incoming radiation is such that the light will interfere constructively. Moreover, the instrument can be tuned so that the peak of the constructive interference occurs at various angles from the central star.

The nulling of a star was tested successfully on the multiple-mirrored MMT telescope before its decommissioning and upgrade to a 6.5-meter telescope (Hinz et al. 2000). However, the successful detection of EGPs likely will be left to the Large Binocular Telescope Interferometer (LBTI), a twin 8.4-meter mirror common-mount telescope due to be operational by late 2005. Using the telescope's AO system along with a nulling beam combiner, which includes a dielectric material to correct for the color-dependence of light interference, at least a few of the currently known EGPs should be detectable according to our model spectra. An *image* of the field around a nulled star, not fringes, will be observable because the point spread function is broader than the transmission function due to the interferometer (Hinz 2001). In the infrared L$'$ Band ($\sim$ 3.6 μm), the LBTI sensitivity is expected to be 2.1 μJy for a 1-hour integration, and the M-band (4.5-5 μm) sensitivity should be 21 μJy for a 1-hour integration. A planet-star separation of $\gtrsim$0.03$''$ will be required (Hinz 2001). Optical wavelengths are not currently being considered for ground-based nulling due to the enormous difficulty of wavefront corrections at these shorter wavelengths.

Among the systems we have modeled, υ And c and d, 55 Cnc d, and ϵ Eri b all have sufficient angular separations from their primaries to be detected with the LBTI. In the L$'$ band, υ And c's average flux density is near 10 μJy, roughly a factor of five greater than the LBTI sensitivity for a 1-hour integration. Upsilon And d will be too dim in the L$'$ band by about an order of magnitude, but its M-band flux density of $\sim$ 20 μJy is comparable to the LBTI sensitivity in that wavelength region. υ And c's M-band flux density is approximately a factor of 5 greater. Although their angular separations are large, our ϵ Eridani b and 55 Cnc d models indicate that these objects will be too dim for imaging via nulling interferometry with the LBTI in either the L$'$ or M bands.

A nulling interferometer is one of two proposed designs for the Terrestrial Planet Finder (TPF), part of a very ambitious plan by NASA for the detection and spectroscopic measurement of Earth-sized planets. The LBTI will provide a ground-based test of the techniques that in principal can work even better outside of Earth's turbulent atmosphere. In addition to the characterization of terrestrial planets, TPF should provided unprecedented spectral data for EGP atmospheres. Launch is anticipated between 2012 and 2015.

Another innovative interferometric development is the differential phase method (Akeson & Swain 2000). Using the Keck Interferometer in the infrared, a faint companion might be detected by simultaneously measuring the fringe phase at two (or more) wavelengths at which the planet-to-star flux ratios are different. Because the primary and secondary sources provide different fractions of the total light received at each of two wavelengths, and because the fractional fringe separation depends on wavelength, a small phase difference will occur. With the twin 10-meter apertures of the Keck, a phase difference as small as 0.1 milliradian might be detectable (Akeson & Swain 2000). Due to their higher planet-to-star flux ratios, hot EGPs with temperatures of $\gtrsim$1000 K are favored by this technique. Of the currently known EGPs, most of the close-in Class V objects meet this criterion.

The differential phase signal in radians is roughly given by twice the difference of the planet-to-star flux ratios (Akeson 2002, private communication). This estimate holds for separations as small as $\sim$2 milliarcseconds. Using the H and K bands (Akeson & Swain 2000), the Class V roasters that we have modeled, such as 51 Peg b, τ Boo b, and υ And b, fall into the 0.1-0.2 milliradian phase-difference range using the H and K bands, the two bands emphasized by Akeson & Swain (2000), indicating that these roasters may be detectable by this method. In contrast, Class IV EGPs translate to well below 0.1 milliradians.

A recent test run on the Palomar Testbed Interferometer (PTI) revealed that the differential phase method may have some difficulties in ultimately reaching 0.1 milliradian accuracy, due to water vapor turbulence in Earth's atmosphere (Akeson et al. 2000). Some ideas for overcoming these difficulties are currently in the works. A refinement of the differential phase method is highly desirable, because if it does prove to be successful, not only detections, but low-resolution spectra of roasters may be obtained by applying it at various wavelengths.

8.5. Interferometric Astrometry

Another class of interferometric techniques for the discovery of new EGPs is high-accuracy, infrared astrometry. This approach would complement the radial-velocity method used for those EGPs currently known, providing orbital inclinations from which companion masses can be derived. The two major ground-based efforts now in development are the VLTI (Very Large Telescope Interferometer) and the Keck Interferometer (KIA). Astrometric interferometry is an indirect detection method in which the position of the central star is monitored as it orbits the system's center of mass. The reflex amplitude of the star is proportional to the mass and distance of the secondary ($a_* = a_p M_p/M_*$). Therefore, with a system such as τ Boo b, for which the planet-star angular separation is $\sim$2.7 milliarcseconds, the reflex motion of the F7V primary will be $\sim$11 microarcseconds, assuming a planetary mass of 5 $M_{\rm J}$ (the most massive of the Class V EGPs to date). Astrometric accuracies of $\sim$10 microarcseconds are expected for KIA and the VLTI. Hence, such precision will enable the measurement of planet masses and inclinations for the majority of Class I through Class IV EGP systems known today.

In the case of the VLTI, its auxiliary 1.8-meter telescopes will be dedicated to full-time interferometry, while the 8.2-meter telescopes will be used for interferometry only intermittently. Due to a baseline of up to 202 meters, very high accuracy will be possible. At 10 parsecs, a Jupiter could be detected at an orbital distance as small as 0.1 AU, and a 0.1 $M_{\rm J}$ object at 1 AU should be measurable as well (Paresce 2001). The Keck Interferometer, with a somewhat shorter baseline, is expected to have similar, though perhaps slightly inferior, resolving power (van Belle & Vasisht 1998).

The Space Interferometry Mission (SIM), scheduled for launch in 2009, is expected to achieve 1-microarcsecond astrometry, an accuracy that will enable the measurement of the orbits of all the EGP systems discovered to date. This 10-meter-baseline instrument could also act as an ideal space-based testbed for one of two possible designs for the larger TPF mission. GAIA, a European equivalent of SIM in terms of astrometric accuracy, is scheduled for launch between 2010 and 2012.

8.6. Coronagraphic Imaging

Coronagraphic imaging is a direct imaging method in which starlight is blocked by a specially-designed phase mask, or coronagraph. Without such a mask, the extremely faint image of an off-axis EGP would be washed out. Due to the difficulties of visible and near-infrared imaging from the ground, coronagraphic instruments suitable for EGP detection are space-based.

Eclipse is a 1.8-meter visible and near-infrared coronagraphic space telescope currently in development at Jet Propulsion Laboratory (Trauger et al. 2000; Trauger et al. 2001). Specifically designed for direct imaging of nearby ($\sim$15 pc) EGPs, this ambitious instrument will contain precision wavefront control technology to correct for even minute imperfections in the optical systems. *Eclipse* is expected to be 3 orders of magnitude better at reducing the scattered and diffracted starlight between 0.3 and a few arcseconds than any HST instrument (Trauger et al. 2000). Within $1''$ of an F or G star, *Eclipse* is being designed to achieve high-contrast imaging of 10^9 in a wide R-band filter (0.55-0.85 μm.); for angular separations of only 0.1–$0.3''$, imaging contrasts of 10^8 may be possible. ϵ Eri b, has a separation of $\sim 1''$ and a modeled R-band plant-to-star flux ratio of $\sim 3\times 10^{-9}$, making it a very likely candidate for direct imaging by *Eclipse*. With a separation of $\sim 0.45''$ and a planet-to-star ratio of $\sim 3\times 10^{-10}$, 55 Cnc d will be close to the detection limit, but it may be slightly too dim for direct R-band imaging.

The 6.5-meter Next Generation Space Telescope (NGST), scheduled for launch in 2010, will house the Near Infrared Camera (NIRCam), including a coronagraphic module. From 2 to 5 μm, the NIRCam coronagraph will be capable of 10^8–10^9 high-contrast imaging for planet-star separations of $\gtrsim 0.1''$ (Rieke et al. 2002). Tunable narrowband filter modules from $\sim$2.5 μm to 4.5 μm will allow for the low-resolution reconstruction of infrared EGP spectra (M. Rieke 2002, private communication). Of the detected EGPs that we have modeled, υ And d, 55 Cnc d, and ϵ Eri b all have sufficient angular separations and planet-to-star flux ratios to be imaged by NGST/NIRCam. According to our theoretical models, for υ And d, the most advantageous wavelength regions for imaging are the K band (2.2 μm) and the broad wavelength region between 3.6 and 5 μm. 55 Cnc d and ϵ Eri b have sufficient planet-to-star flux ratios for coronagraphic imaging within only the 4-5 μm opacity window.

The Extra-solar Planet Imager (ESPI) is a space telescope with a 1.5-meter square aperture and a custom mask (Melnick et al. 2001). The resulting diffraction pattern is cross-shaped rather than circular, and the telescope can be rotated so that a faint companion EGP appears between two edges of the pattern. The planet-star separation limit is expected to be in the $0.3''$ range. Hence, for many systems, Jupiter-like EGPs orbiting at a few AU or more may be detectable. Another space-based coronagraphic instrument of similar size is the Jovian Planet Finder (JPF), a 1.46-meter coronagraphic optical telescope that would be located on the International Space Station. The JPF would survey 50 of the closest stars for EGPs orbiting between 2 and 20 AU and would survey 2000 of the closest stars for more massive brown dwarf companions.

A visible coronagraphic instrument is also a design concept for TPF. If this path is chosen instead of the interferometric design, extremely precise optics will be required to image terrestrial planets. Even minute imperfections scatter light and degrade contrast, so an AO system will be used to correct the wavefront for such imperfections (as with *Eclipse*). Whichever concept is adopted, it is assured that any instrument designed to reveal information about terrestrial planets and their atmospheres will provide even more detailed information about the gas giants known today and the hundreds more that will be discovered in the coming years.

9. SUMMARY AND CONCLUSIONS

In this paper we have conducted an extensive exploration of spectral and atmospheric models of irradiated extrasolar giant planets. Our central purpose has been to provide a map to observers, as well as a comprehensive view of the theoretical possibilities. We have investigated the dependence of the phase-averaged emergent spectra on orbital distance, stellar type, the presence or absence of clouds, cloud particle sizes, surface gravity, and the inner flux boundary condition. Included are calculations for irradiated brown dwarfs, specific known EGP systems, a generic sequence around a G0V star, and our composition Classes I to V. In addition, we have reviewed representative direct detection techniques in the context of our theoretical models.

There are many overall, as well as specific, conclusions represented in the previous sections and a full summary of them here would be heavily redundant. Nevertheless, a small subset of the most salient points, in no particular order, is useful. They are that:

- the planet-to-star flux ratio is a very sensitive function of wavelength and orbital distance.

- EGP band fluxes are not strictly monotonic functions of orbital distance, nor are the Bond and geometric albedos.

- EGPs fall naturally into classes due to qualitative similarities in the compositions and spectra of objects within several broad atmospheric temperature ranges.

- the mid-infrared region of the spectrum from 10 to 30 μm has a favorable planet-to-star flux ratio, even for distant EGPs, and does not decay as fast as $1/a^2$.

- due to Rayleigh and/or grain scattering, the optical spectrum of an irradiated brown dwarf can be very much brighter than that of a brown dwarf in isolation, even when its near- and mid-infrared spectra remain relatively unaffected.
- the fluxes in the Z, J, H, and K bands of an EGP in a long-period orbit can be enhanced above baseline levels (normally determined by stellar irradiation and scattering alone), if the planet is either young or massive.
- there is a *relatively* bright feature within the 3.8 to 5 μm wavelength region for all irradiated EGPs, and in particular for the more distant EGPs (such as 55 Cnc d, ϵ Eridani, 47 UMa c, Gliese 777A, and υ And d).
- as a result of the progressive decrease in atmospheric CO abundance, the center of the 3.8 to 5.0 μm feature shifts systematically from shorter to longer wavelengths with increasing orbital distance (or decreasing stellar luminosity).
- Rayleigh and grain scattering elevate the optical and near-IR fluxes, but grain absorption depresses the mid-infrared fluxes (in particular in the "5-μm" band).
- increasing surface gravity slightly decreases the flux shortward of $\sim$2.2 μm, but also slightly increases it longward of $\sim$2.2 μm. The larger the gravity the smaller the peak-to-trough variations throughout the spectrum.
- the Na-D and K I resonance doublets are prominent features of the hottest, close-in EGPs (such as 51 Peg b, τ Boo b, HD209458b), but quickly wane in importance with increasing orbital distance.

Table 1 lists some of the most prominent near-term targets for direct detection, as well as all of the known EGPs for which we have provided theoretical spectra in this paper. Our models collectively span the variety of discovered systems with their wide range of orbital distances, stellar types, and M$_p$sin(i)s. However, much remains to be done, including calculating phase functions (SWS), exploring metallicity and abundance dependences, predicting the character of EGPs irradiated by stars of other spectral types and luminosity classes, incorporating 3D meteorology, and investigating the effects of NLTE and non-equilibrium chemistry. As a result, the theorist will be profitably engaged for the foreseeable future. However, the next major phase of EGP research should see the direct measurement of EGP photons, first at low spectral resolution, then higher. The many instruments, techniques, and telescopes being employed to detect EGPs directly, summarized in §8, suggest that we do not have long to wait before the theory we have presented here will be tested.

The authors are happy to thank Bill Hubbard, Jonathan Lunine, Jim Liebert, Aigen Li, Christopher Sharp, Drew Milsom, Maxim Volobuyev, Curtis Cooper, and Jonathan Fortney for fruitful conversations and help during the course of this work, as well as NASA for its financial support via grants NAG5-10760 and NAG5-10629.

REFERENCES

Ackerman, A., & Marley, M. S. 2001, ApJ, 556, 872
Akeson, R. L. & Swain, M. R. 2000, in From Giant Planets to Cool Stars, ed. C. A. Griffith & M. S. Marley, ASP Conference Series, 212, 300
Akeson, R. L., Swain, M. R., & Colavita, M. M 2000, in Interferometry in Optical Astronomy, ed. P. J. Lena, Proc. SPIE 4006, 321
Anders, E. & Grevesse, N. 1989, Geochim. Cosmochim. Acta, 53, 197
Antonello, E. & Ruiz, S. M. 2002, The Corot Mission, http://www.astrsp-mrs.fr/projects/corot/corotmission.ps
Auer, L.H. 1976, JQSRT, 16, 931
Auer, L.H., & Mihalas, D. 1969, ApJ, 158, 641
Baliber, N. R. & Cochran, W. D. 2001, AAS DPS, 40, 40.01
Barman, T. S., Hauschildt, P. H., & Allard, F. 2001, ApJ, 556, 885
Bar-Nun, A., Kleinfeld, I., &Ganor, E. 1988, J. Geophys. Res., 93, 8383
Black, D. C. & Stepinski, T. F. 2001, AAS DDA Meeting 32, 13.03
Boccaletti, A. 1999, The NGST Coronagraphic Mode Study, http://www.nasa.ngst.gov
Brown, T. M. & Charbonneau, D. 1999, BAAS, 31, 1534
Burrows, A., Marley, M., Hubbard, W. B., Lunine, J. I., Guillot, T., Saumon, D., Freedman, R., Sudarsky, D., & Sharp, C. 1997, ApJ, 491, 856
Burrows, A. & Sharp, C. M. 1999, ApJ, 512, 843
Burrows, A., Guillot, T., Hubbard, W. B., Marley, M. S., Saumon, D., Lunine, J. I., & Sudarsky, D. 2000, 534, 97
Burshtein, Z., Shimony, Y., & Levy, I. 1993, J. Opt. Soc. Am. A, 10, 2246
Butler, R. P., Marcy, G. W., Williams, E., Hauser, H. & Shirts, P. 1997, Astrophys. J. Letters , 474, L115
Butler, R. P, Marcy, G. W., Fischer, D. A., et al.1999, ApJ, 526, 916
Butler, R. P., Marcy, G. W., Vogt, S. S., Tinney, C., Jones, H., McCarthy, C., Penny, A., Apps, K., & Carter, B. 2002, ApJ(in press)
Cameron, A. C., Horne, K., Penny, A., & James, D. 1999, Nature, 402, 751
Castor, J. I., Dykema, P. G., & Klein, R. I. 1992, ApJ, 387, 561
Charbonneau, D., Brown, T. M., Latham, D. W., & Mayor, M. 2000, Astrophys. J. Letters , 529, L45
Charbonneau, D., Brown, T. M., Noyes, R. W., & Gilliland, R. L. 2002, ApJ, 568, 377
Cho, J. Y-K., Menou, K., Hansen, B. M. S., & Seager, S. 2002, submitted to Astrophys. J. Letters
Christensen-Dalsgaard, J. 2000, http://bigcat.obs.aau.dk/hans/mons/
Clampin, M., Ford, H. C., Illingworth, G., & Petro, L. 2001, AAS Meeting 199, 33.02
Cody, A. M. & Sasselov, D. D. 2002, ApJ, 569, 451
Cooper, C. S., Sudarsky, D., Milsom, J. A., Lunine, J. I., & Burrows, A. 2002, submitted to ApJ
Deirmendjian, D. 1964, Applied Optics, 3, 187
Deirmendjian, D. 1969, Electromagnetic Scattering on Spherical Polydispersions, (New York: Elsevier)
Delfosse, X., Forveille, T., Mayor, M., Perrier, C., Naef, D., & Queloz, D. 1998, A&A, 338, L67
Dorschner, J., Begemann, B., Henning, Th., Jager, C., and Mutschke, H. 1995, A&A, 300, 503
Edgington, S. G., Atreya, S. K. Trafton, L. M., Caldwell, J. J, Beebe, R. F., Simon, A. A., West, R. A., & Barnet, C. 1998, Icarus, 133, 192
Feautrier, P. 1964, C. R. Acad. Sci. Paris, 258, 3189
Freed, M. E., Close, L. M., & McCarthy, D. W. 2002, in Scientific Frontiers in Research on Extrasolar Planets, ed. D. Deming & S. Searger, in preparation
Gatewood, G. 2000, BAAS, 32, 32.01
Gervais, F. 1990, in Handbook of Optical Constants of Solids II, ed. E. D. Palik (Orlando: Academic), 766
Goukenleuque, C., Bezard, B., Joguet, B., Lellouch, E., & Freedman, R. 2000, Icarus, 143, 308
Gray, D. F. 1997, Nature, 385, 795
Gray, D. F. & Hatzes, A. P. 1997, ApJ, 490, 312

Greaves, J., Holland, W., Moriarty-Schiven G., et al. 1998, Astrophys. J. Letters , 506, L133
Green, D., Mathews, J., & Seager, S. 2002, in Scientific Frontiers in Research on Extrasolar Planets, ed. D. Deming & S. Searger, in preparation
Guillot, T., Burrows, A., Hubbard, W. B., Lunine, J. I., & Saumon, D. 1996, ApJ, 459, 35
Guillot, T. & Showman, A. P. 2002, A&A, 385, 156
Han, I., Black, D. C., & Gatewood, G., Astrophys. J. Letters , 548, L57
Hatzes, A., Cochran, W., McArthur, B., et al. 2000, Astrophys. J. Letters , 544, L145
Henry, G., Marcy, G. W., Butler, R. P., & Vogt, S. S. 2000, Astrophys. J. Letters , 529, L41
Hinz, P. M, Angel, J. R. P., Woolf, N. J., Hoffman, W. F., & McCarthy, D. W. 2000, in Interferometry in Optical Astronomy, ed. P. J. Lena, Proc. SPIE 4006, 349
Hinz, P. M. 2001, PhD Thesis, The University of Arizona
Hubbard, W. B., Fortney, J. F., Lunine, J. I., Burrows, A., Sudarsky, D., & Pinto, P. A. 2001, ApJ, 560, 413
Hubeny, I. 1988, Computer Physics Comm., 52, 103
Hubeny, I. 1992, in The Atmospheres of Early-Type Stars, ed. U. Heber & C. J. Jeffery, Lecture Notes in Phys. 401, (Berlin: Springer), 377
Hubeny, I. & Lanz, T. 1995, ApJ, 439, 875
Khare, B. N., Sagan, C. 1984, Icarus, 60, 127
Koch, D., Borucki, W., Webster, L., Dunham, E., Jenkins, J., Marrion, J., & Reitsema, H. 1998, SPIE Conference 3356: Space Telescopes and Instruments V, 599
Kurucz, R. 1994, Kurucz CD-ROM No. 19, (Cambridge: Smithsonian Astrophysical Observatory)
Latham, D. W., Stefanik, R. P., Mazeh, T., Mayor, M., & Burki, G. 1989, Nature, 339, 38
Lodders, K. 1999, ApJ, 519, 793
Lodders, K. 2002, submitted to ApJ
Marcy, G. W., Butler, R. P., Vogt, S. S, Fischer, D., & Lissauer J. J. 1998, Astrophys. J. Letters , 505, L147
Marcy, G. W., Butler, R. P., Fischer, D. A., Laughlin, G., Vogt, S. S., Henry, G. W., & Pourbaix, D. 2002, submitted to ApJ
Marley, M. S., Gelino, C., Stephens, D., Lunine J. I., & Freedman, R. 1999, Astrophys. J. Letters , 513, 879
Marois, C. 2002, in Scientific Frontiers in Research on Extrasolar Planets, ed. D. Deming & S. Searger, in preparation
Martonchik, J. V., Orton, G. S., & Appleby, J. F. 1984, Applied Optics, 23, 541
Matthews, J. M., Kuschnig, R., Walker, G. A. H. et al. in The Impact of Large-Scale Surveys on Pulsating Star Research, ed. L. Szabados & D. Kurtz, p. 74
Mayor, M. & Queloz, D. 1995, Nature, 378, 355
Mayor, M., Naef, D., Pepe, F., Queloz, D., Santos, N., Udry, S., & Burnet, M. 2000, in Planetary Systems in the Universe, IAU Symposium 202, eds. A Penny, P. Artymowicz, A.-M. Lagrange, & S. Russel, ASP Conference Series
Mazeh, T., Naef, D., Torres, G., et al. 2000, Astrophys. J. Letters , 532, L55
Melnick, G. J., Fischer, D., Geary, J. C. et al. 2001, AAS Meeting 199, 09.10
Mihalas, D. 1978, Stellar Atmospheres, 2nd Ed., (San Francisco: Freeman & Co.)
Mihalas, D. 1980, ApJ, 238, 1034
Noll, K. S., Knacke, R. F, Tokunaga, A. T., Lacy, J. H., Beck, S., & Serabyn, E. 1986, Icarus, 65, 257
Noy, M., Podolak, M. & Bar-Nun, A. 1981, J. Geophys. Res., 86, 11985
Paresce, F. 2001, Scientific Objectives of the VLTI Interferometer
Rieke, M., Beichman, C., Eisenstein, D., & Meyer, M. 2002, http://ircamera.as.arizona.edu/nircam/
Rossman, G. R. & Taran, M. N. 2001, American Mineralogist, 86, 896
Ryan, S. G. 2001, MNRAS(in press)
Santos, N. C., Israelian, G., and Mayor, M. 2001, A&A(in press)
Scott, A. & Duley, W. W. 1996, ApJS, 105, 401
Saumon, D., Hubbard, W.B., Burrows, A., Guillot, T., Lunine, J.I. and Chabrier, G. 1996, ApJ, 460, 993
Seager, S. & Sasselov, D. D. 1998, ApJ, 502, 157
Seager, S., Whitney, B. A, & Sasselov, D. D. 2000, ApJ, 540, 504
Seager, S. & Sasselov, D. D. 2000, ApJ, 537, 916
Showman, A. P. & Guillot, T. 2002, A&A, 385, 166
Stepinski, T. F. & Black, D. C. 2001, A&A, 371, 250
Sudarsky, D., Burrows, A., & Pinto, P. 2000, ApJ, 538, 885
Trafton, L. M. 1967, ApJ, 147, 765
Trauger, J., Backman, D., Brown, R. A. et al. 2000, AAS Meeting 197, 49.07
Trauger, J., Hull, A. B., & Redding, D. A. 2001, AAS Meeting 199, 86.04
Tropf, W. J. & Thomas, M. E. 1990, in Handbook of Optical Constants of Solids II, ed. E. D. Palik (Orlando: Academic), 883
Udalski, A., Paczynski, B., Zebrun, K., Szymanski, M., Kubiak, M., Soszynski, I., Szewczyk, O., Wyrzykowski, L. & Pietrzynski, G. 2002, The Optical Gravitational Lensing Experiment. Search for Planetary and Low-Luminosity Object Transits in the Galactic Disk. Results of 2001 Campaign, http://bulge.princeton.edu/~ogle
Unwin, S. C. & Shao, M. 2000, in Interferometry in Optical Astronomy, ed. P. J. Lena & A. Quirrenbach, 754
van Belle, G. & Vasisht, G. 1998, The Keck Interferometer Science Requirements Document, Revision 2.2, Jet Propulsion Laboratory
Warren, S. G. 1984, Applied Optics, 23, 8
Warren, S. G. 1991, in Handbook of Optical Constants of Solids II, ed. E. Palik (San Diego: Academic Press, Inc.), 236

Table 1
Interesting EGPs Listed by Angular Separation

EGP	separation ($''$)	star	a (AU)	d (pc)	P	Msin$i$ ($M_{\rm J}$)	e
ϵ Eri b	1.0	K2V	3.3	3.2	6.85 yrs.	0.86	0.61
55 Cnc d	0.44	G8V	5.9	13.4	14.7	4.05	0.16
47 UMa c	0.28	G0V	3.73	13.3	7.10	0.76	0.1
Gl 777A b	0.23	G6V	3.65	15.9	7.15	1.15	$\sim$0
υ And d	0.19	F8V	2.50	13.5	3.47	4.61	0.41
HD 39091b	0.16	G1IV	3.34	20.6	5.70	10.3	0.62
47 UMa b	0.16	G0V	2.09	13.3	2.98	2.54	0.06
γ Cephei b	0.15	K2V	1.8	11.8	2.5	1.25	$\sim$0
14 Her b	0.15	K0V	2.5	17	4.51	3.3	0.33
HD 216437b	0.10	G4V	2.7	26.5	3.54	2.1	0.34
HD 147513b	0.098	G3V	1.26	12.9	1.48	1.0	0.52
HD 33636b	0.094	G0V	2.7	28.7	4.43	7.71	0.41
HD 13507b	0.091	G0V	2.39	26.2	3.61	3.45	0.13
HD 168443c	0.087	G5V	2.87	33	4.76	17.1	0.23
HD 50554b	0.077	F8V	2.38	31.03	3.50	4.9	0.42
HD 106252b	0.070	G0V	2.61	37.44	4.11	6.81	0.54
HD 10697b	0.067	G5IV	2.0	30	2.99	6.59	0.12
υ And c	0.061	F8V	0.83	13.5	241 days	2.11	0.18
GJ 876b	0.045	M4V	0.21	4.72	61.0	1.89	0.1
GJ 876c	0.028	M4V	0.13	4.72	30.1	0.56	0.27
HD 114762b	0.013	F9V	0.35	28	84.0	11.0	0.34
55 Cnc b	8.2×10^{-3}	G8V	0.12	13.4	14.7	0.84	0.02
υ And b	4.4×10^{-3}	F8V	0.059	13.5	4.62	0.71	0.034
51 Peg b	3.4×10^{-3}	G2V	0.05	14.7	4.23	0.44	0.01
τ Boo b	3.3×10^{-3}	F7V	0.05	15	3.31	4.09	$\sim$0
HD 209458b	9.6×10^{-4}	G0V	0.045	47	3.52	0.69	$\sim$0
HD 83443b	8.7×10^{-4}	K0V	0.038	43.5	2.99	0.35	0.08

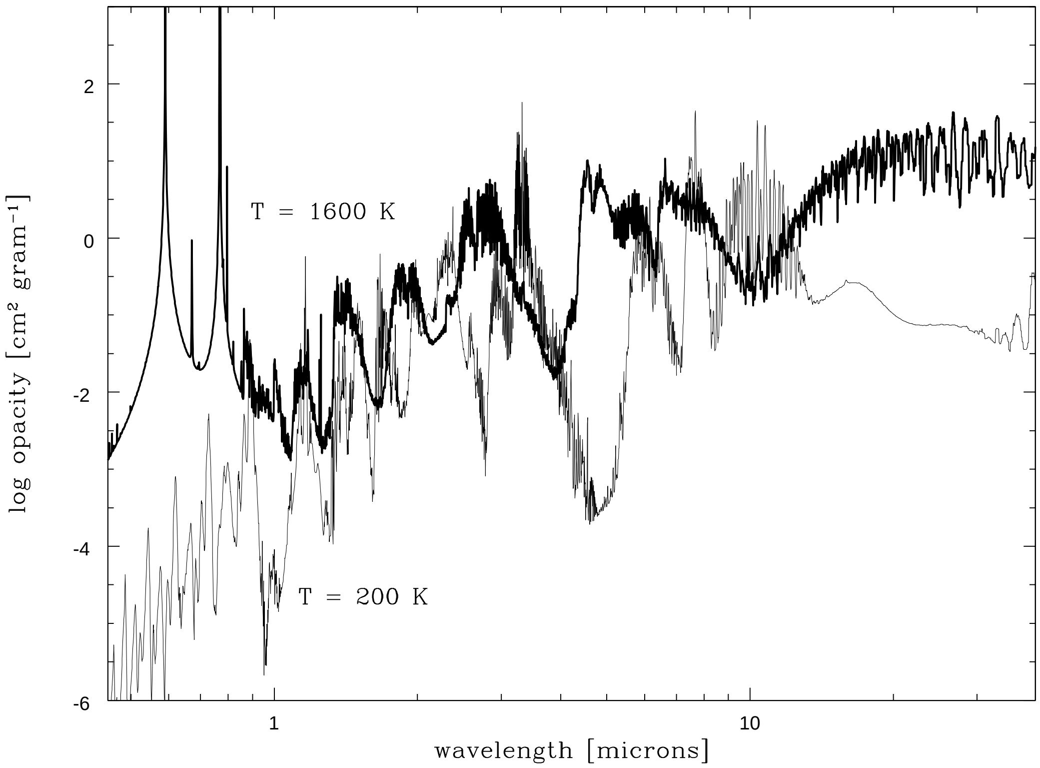

Fig. 1.— Depiction of the differences in total, abundance-weighted gaseous opacities in hot and cold EGP atmospheres at P = 1 bar. The opacity in the visible region of a hot atmosphere is up to several orders of magnitude larger than that of a relatively cold atmosphere. In contrast, there are regions in the infrared where the total opacity of the cold atmosphere is greater.

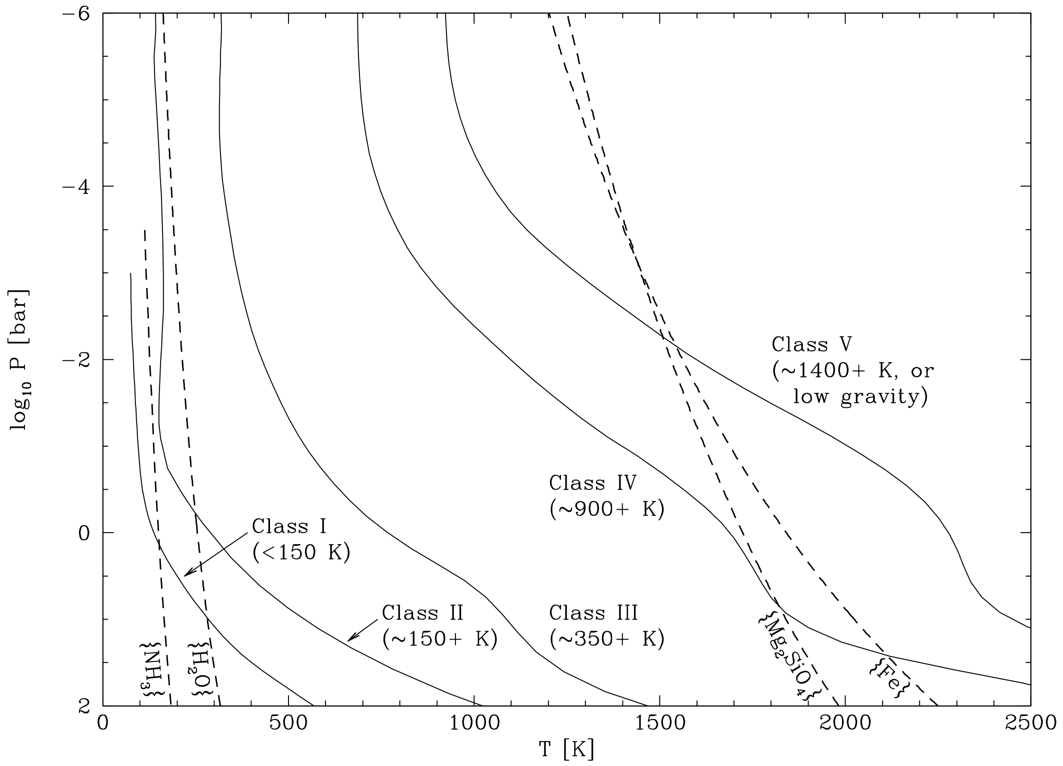

Fig. 2.— Temperature-Pressure (T-P) profiles of EGPs over the full range in effective temperature. The profiles shown represent the different EGP classes. The corresponding emergent spectra are depicted in Figures 3, 4, 5, 8, and 11. Condensation curves for four high-abundance condensates (ammonia, water, a silicate, and iron) are also shown. The intersection of these curves with the T-P profiles indicates the positions of cloud bases. (For clarity, cloud-free T-P profiles are shown here.)

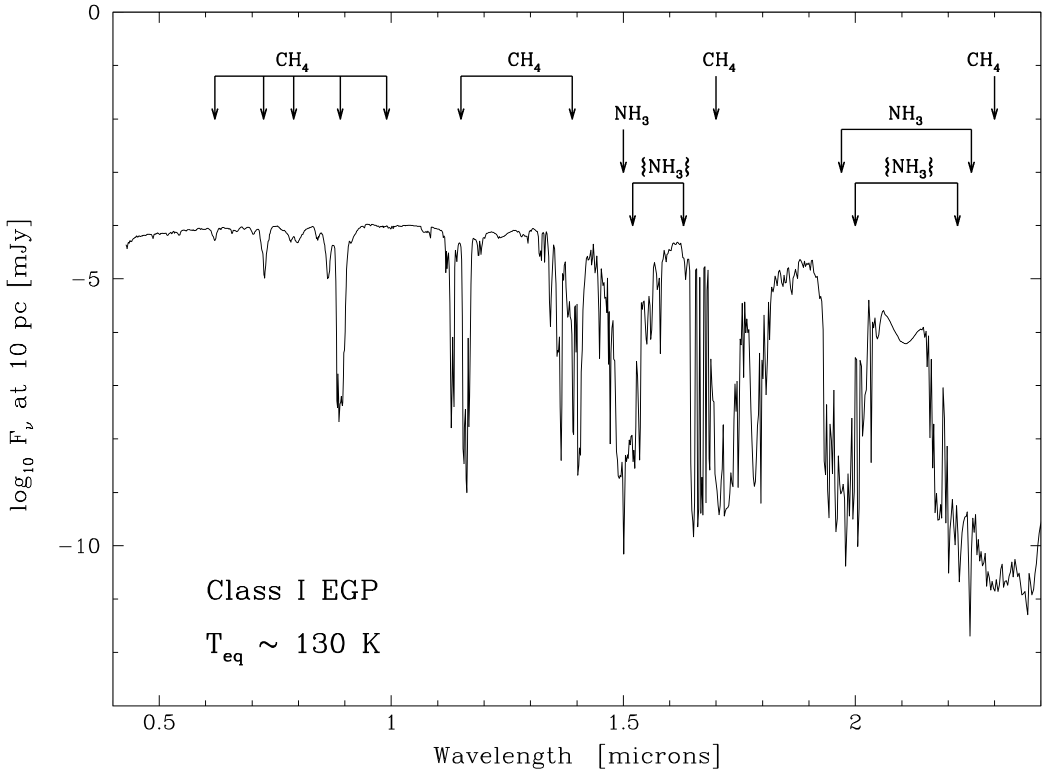

Fig. 3.— Emergent spectrum of a Class I ("Jovian"; $\sim$ 5 AU) EGP. The temperature in the outer atmosphere is cold enough ($\lesssim$ 150 K) that ammonia condenses into ice, which provides significant reflection. The upper troposphere is depleted of water, which is condensed into a cloud layer at a pressure of a few-to-several bars. Methane and ammonia absorption dominate the visible and near-infrared spectrum. Note that '$\{NH_3\}$' indicates a feature of condensed ammonia, while 'NH_3' indicates that of gaseous ammonia.

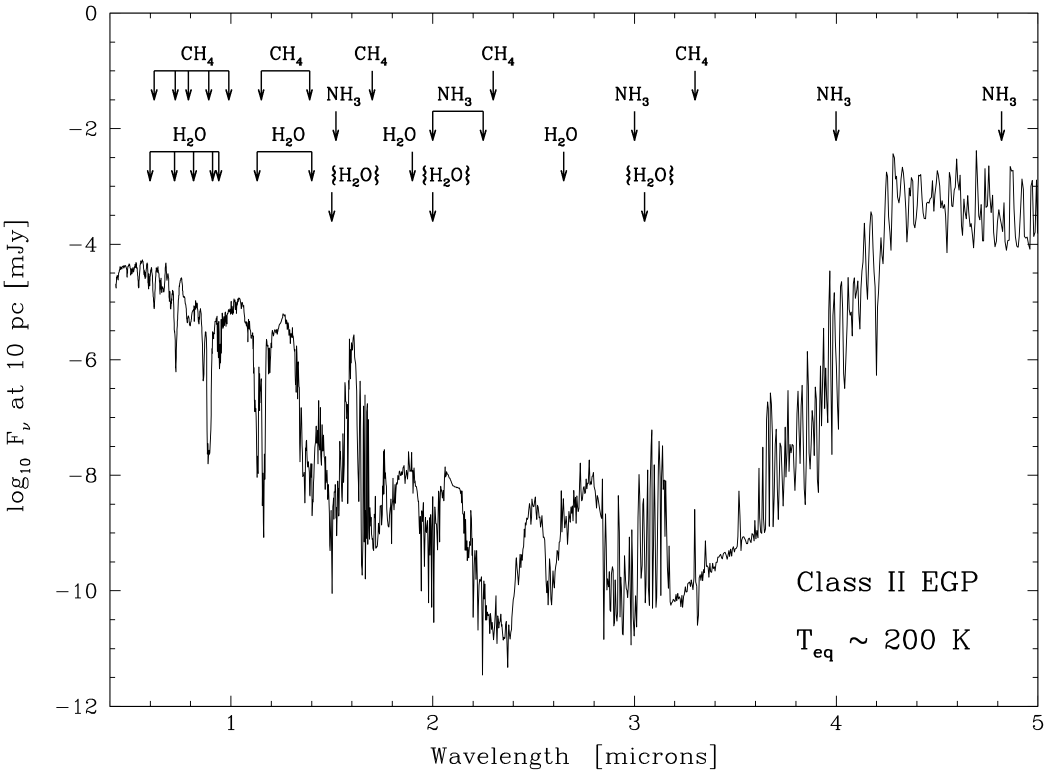

Fig. 4.— Emergent spectrum of a Class II ("water class"; ∼ 1-2 AU) EGP. A water cloud resides in the troposphere, but the temperature at every pressure is hot enough that ammonia remains in gaseous form. Reflection by water keeps the emergent flux higher than it would otherwise be in the visible and near-infrared. Gaseous absorption by methane, water, and ammonia produce strong spectral features. Note that '{H_2O}' indicates a feature of condensed water, while 'H_2O' indicates that of gaseous water.

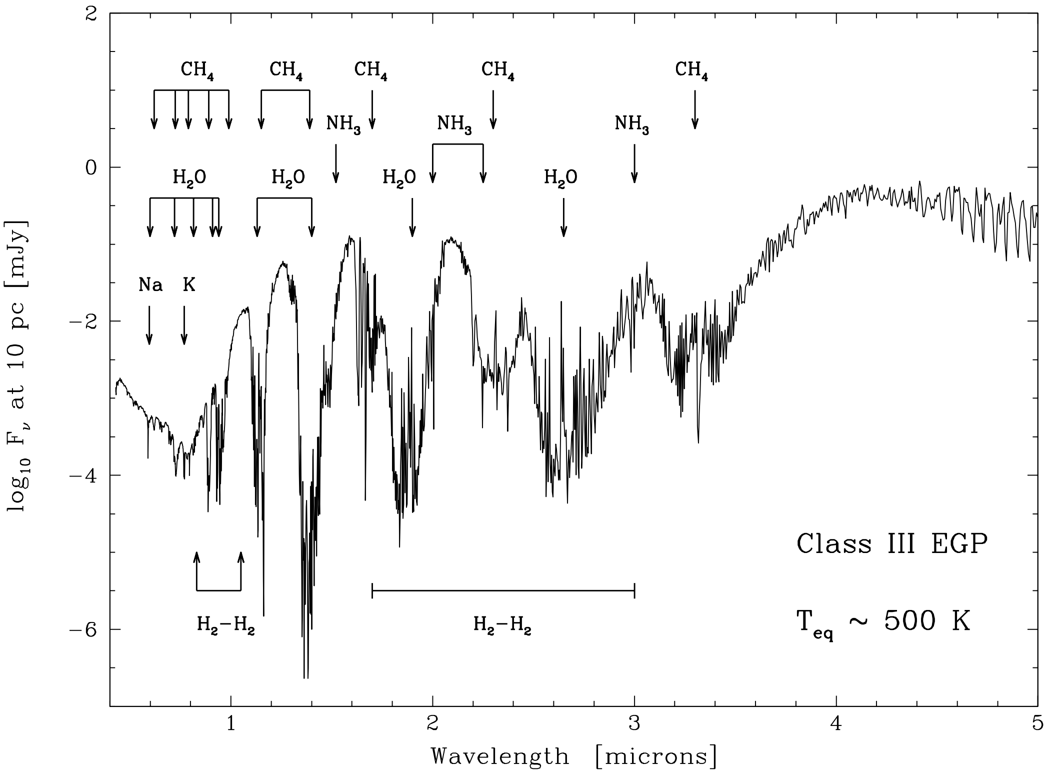

Fig. 5.— Emergent spectrum of a Class III ("clear"; $\sim$ 0.5 AU) EGP. These objects are too warm for water to condense, but too cold for a silicate layer to appear in the upper troposphere. In the absence of any high-abundance, principal condensates, the ro-vibrational molecular absorption features are very strong. Of particular importance are absorption by gaseous water, methane, and molecular hydrogen (collision-induced). Additionally, alkali metal lines appear in the visible.

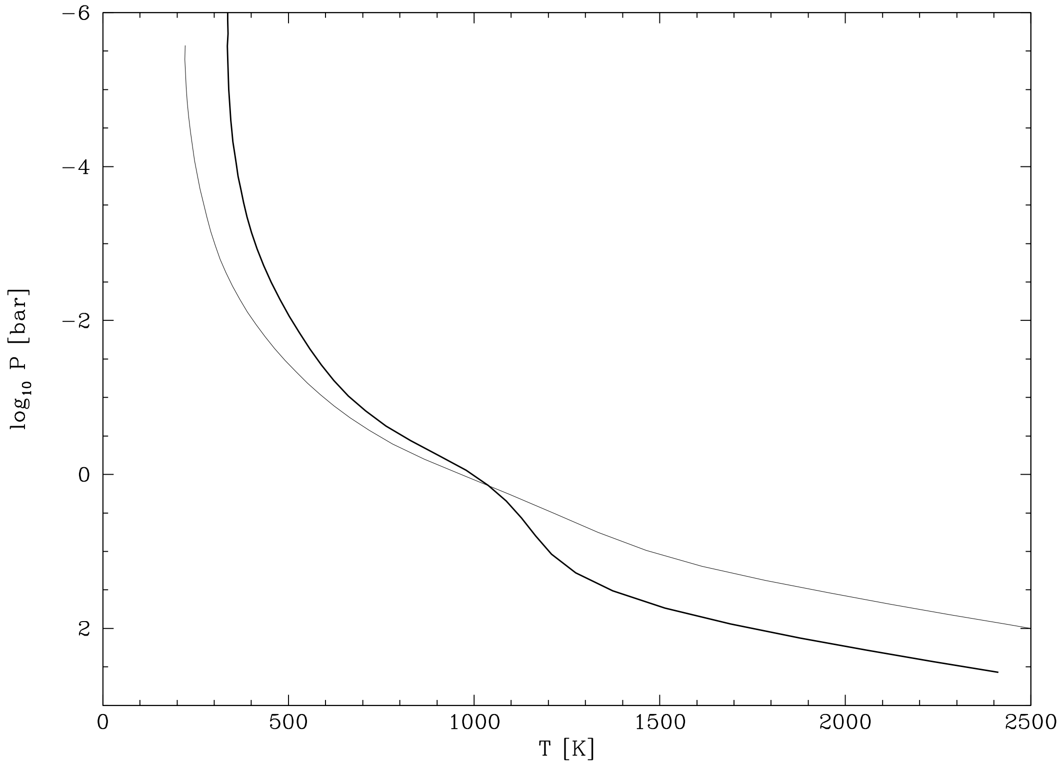

Fig. 6.— Comparison of the T-P structure of a Class III EGP (thick curve) with that of a brown dwarf (thin curve) with the same surface gravity and total integrated emergent flux. The outer atmosphere of the EGP is more isothermal due to irradiation by the primary.

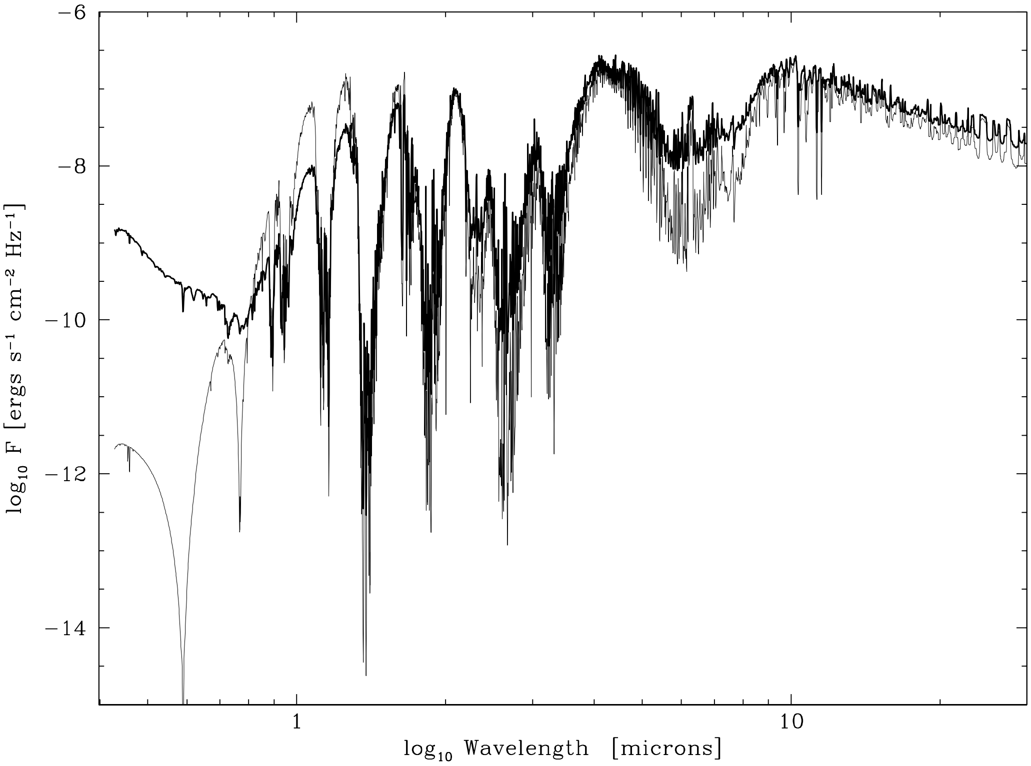

Fig. 7.— Comparison of the emergent spectrum of a Class III EGP (thick curve) with that of a cloud-free brown dwarf (thin curve) of the same surface gravity and integrated emergent flux. By construction, the fluxes are identical, but the spectral energy distributions differ significantly. (Fluxes shown are at the objects' surfaces.)

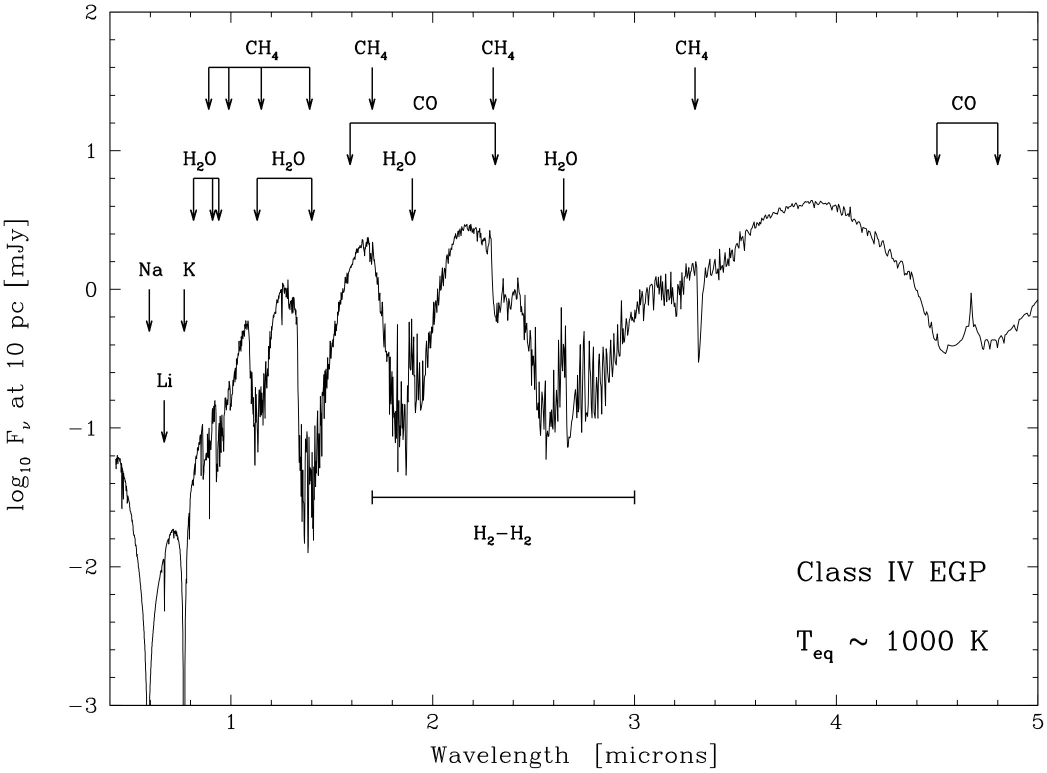

Fig. 8.— Emergent spectrum of a Class IV EGP (∼0.1 AU). The visible spectrum is dominated by strong pressure-broadened sodium and potassium resonance lines, while gaseous water, methane, and carbon monoxide absorption are strong in the infrared. Silicate and iron clouds exist at depth, but they have no significant effects on the visible and near-infrared emergent spectra.

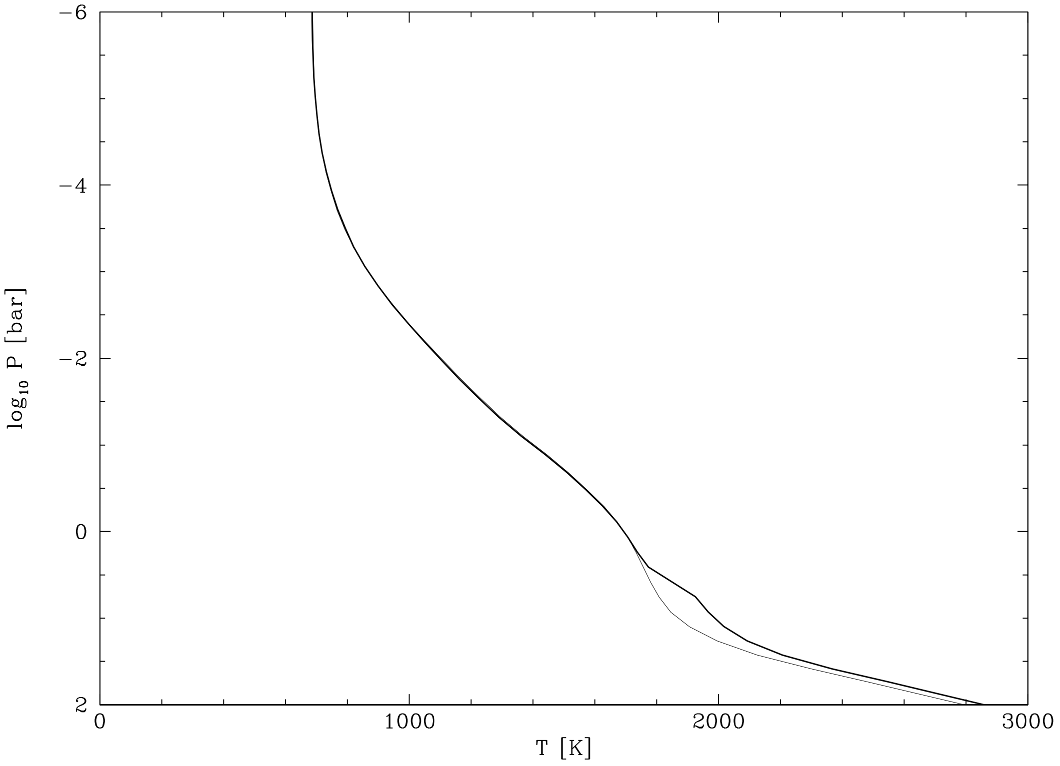

Fig. 9.— Effect of a deep silicate cloud on the T-P structure of a Class IV EGP. The resulting T-P profile (thick curve) differs from that of a cloud-free model (thin curve), but only at depth.

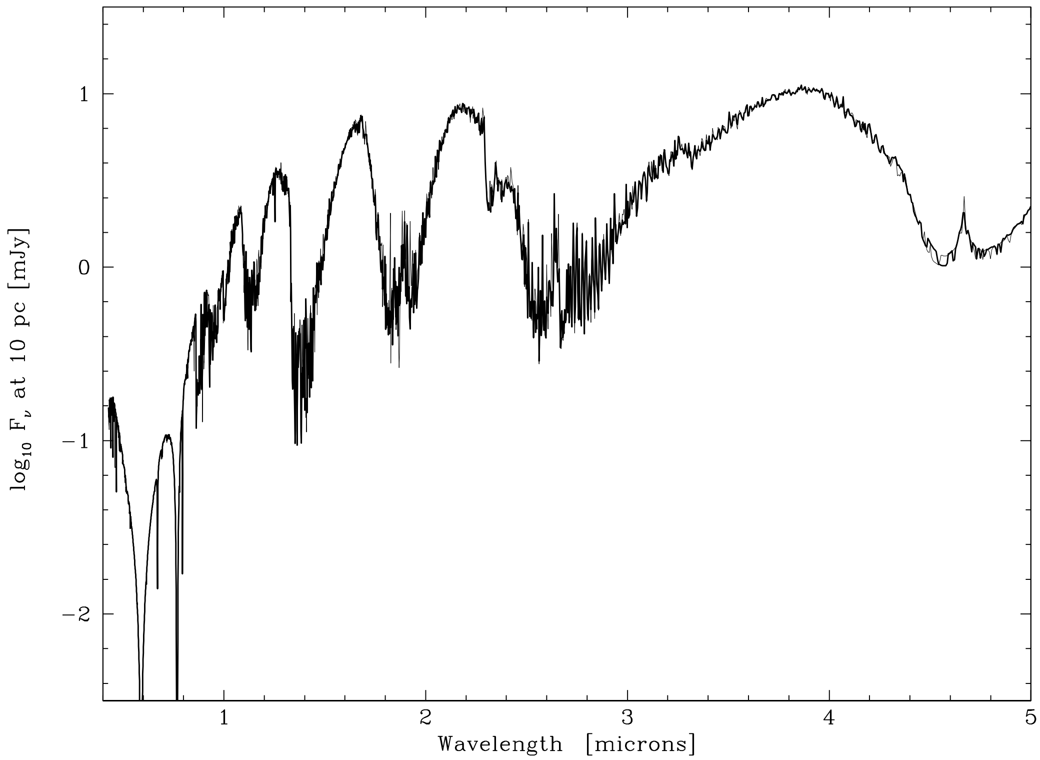

Fig. 10.— Emergent spectrum of a Class IV EGP with its deep silicate cloud (thick curve) relative to that of a cloud-free model (thin curve). Silicate clouds in Class IV EGPs form too deeply to have significant effects on their emergent spectra.

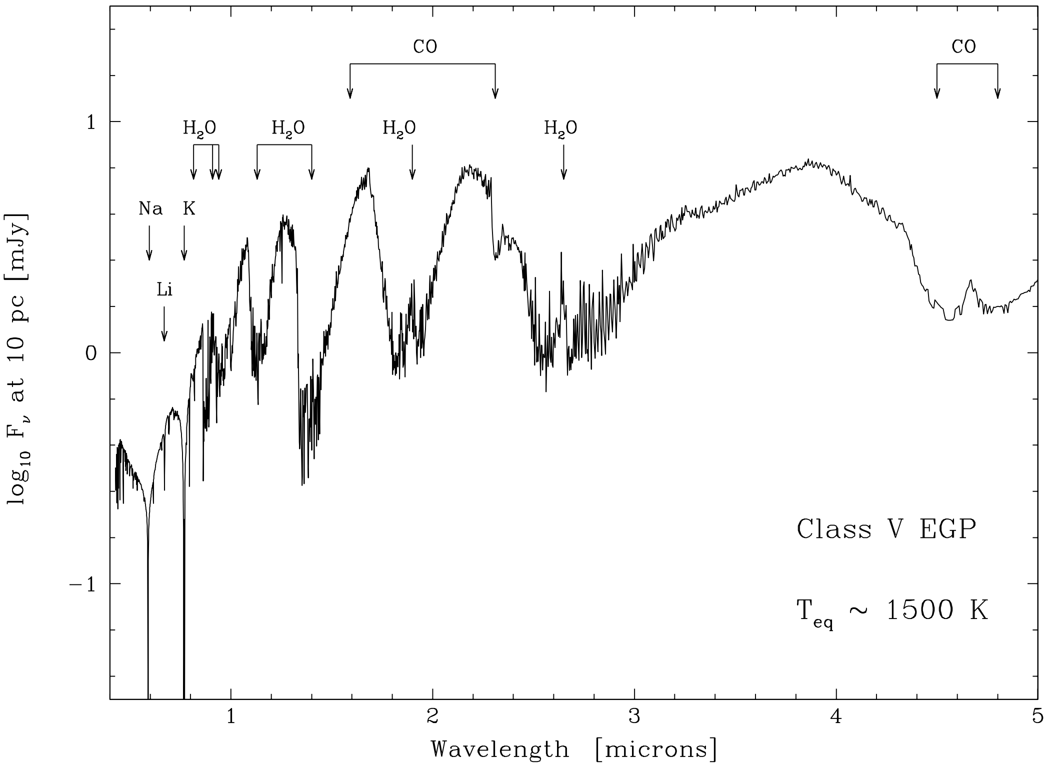

Fig. 11.— Emergent spectrum of a Class V EGP (a "roaster"; ~ 0.05 AU). Like Class IV objects, these EGPs have strong alkali lines, but scattering and absorption by silicate and iron grains high in the atmosphere alter the character of the spectrum. Furthermore, nearly all of the carbon resides in carbon monoxide, so methane features are very weak or nonexistent.

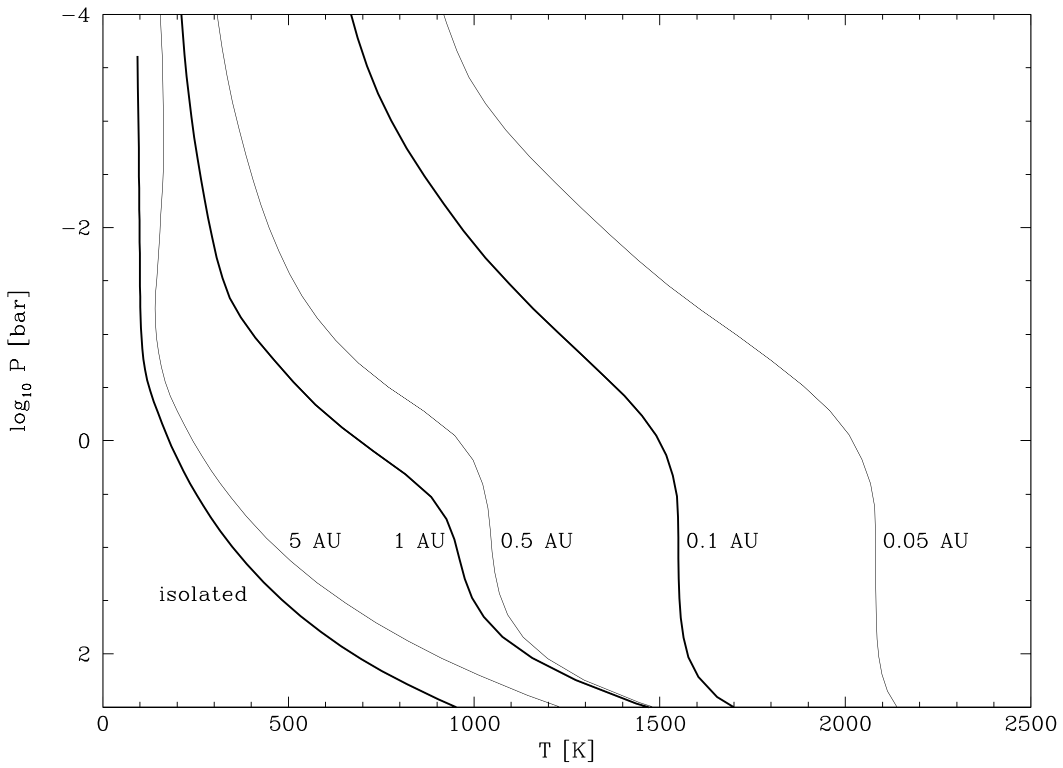

Fig. 12.— Cloud-free EGP T-P profiles as a function of orbital distance from a G0V primary. From right to left, the orbital distance is 0.05 AU, 0.1 AU, 0.5 AU, 1 AU, and 5 AU. Additionally, the leftmost profile (thick curve) is that of an isolated EGP/brown dwarf. In all cases, the gravity is 3×10^3 cm s^{-2} and the inner boundary flux is set equal to that of an isolated object with $T_{\rm eff}$ = 125 K. (Note that we have alternated between thin and thick line types in order to facilitate a correspondence with the spectra in Figures 13 and 15.)

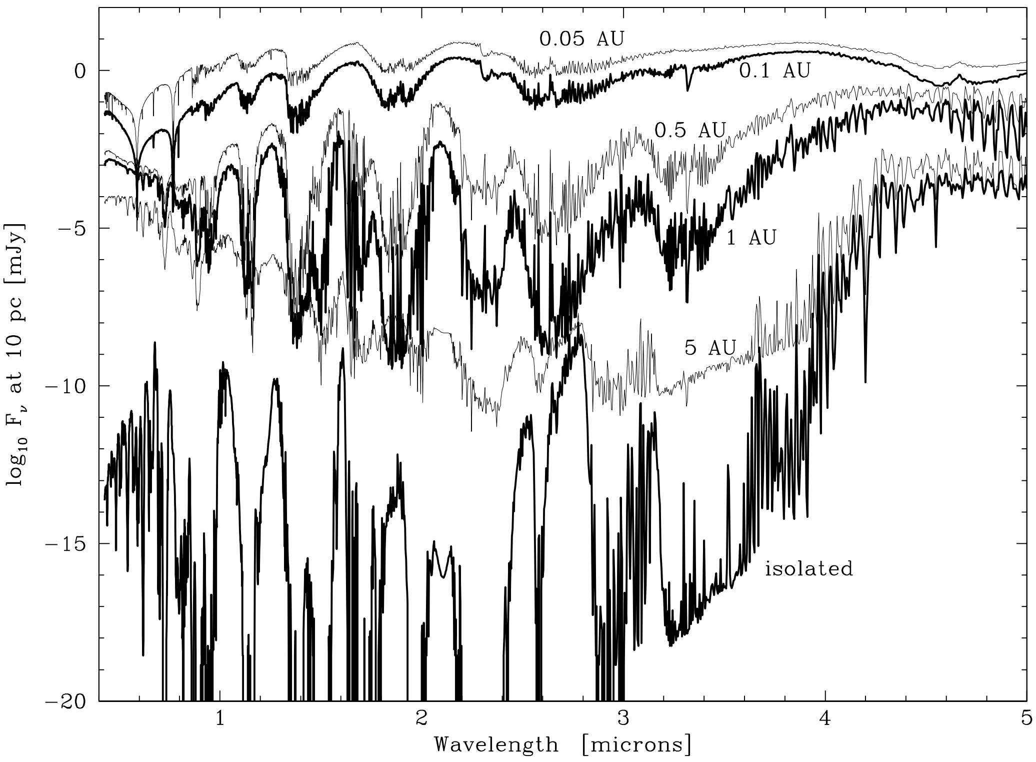

Fig. 13.— Cloud-free EGP emergent spectra as a function of orbital distance from a G0V primary. From top to bottom, the orbital distance is 0.05 AU, 0.1 AU, 0.5 AU, 1 AU, and 5 AU. Additionally, the bottom curve is that of an isolated EGP/brown dwarf. In all cases, the gravity is 3×10^3 cm s^{-2} and the lower boundary flux is set equal to that of an isolated object with $T_{\rm eff}$ = 125 K. (Note that we have alternated between thin and thick line types in order to facilitate a correspondence with the profiles in Figure 12.)

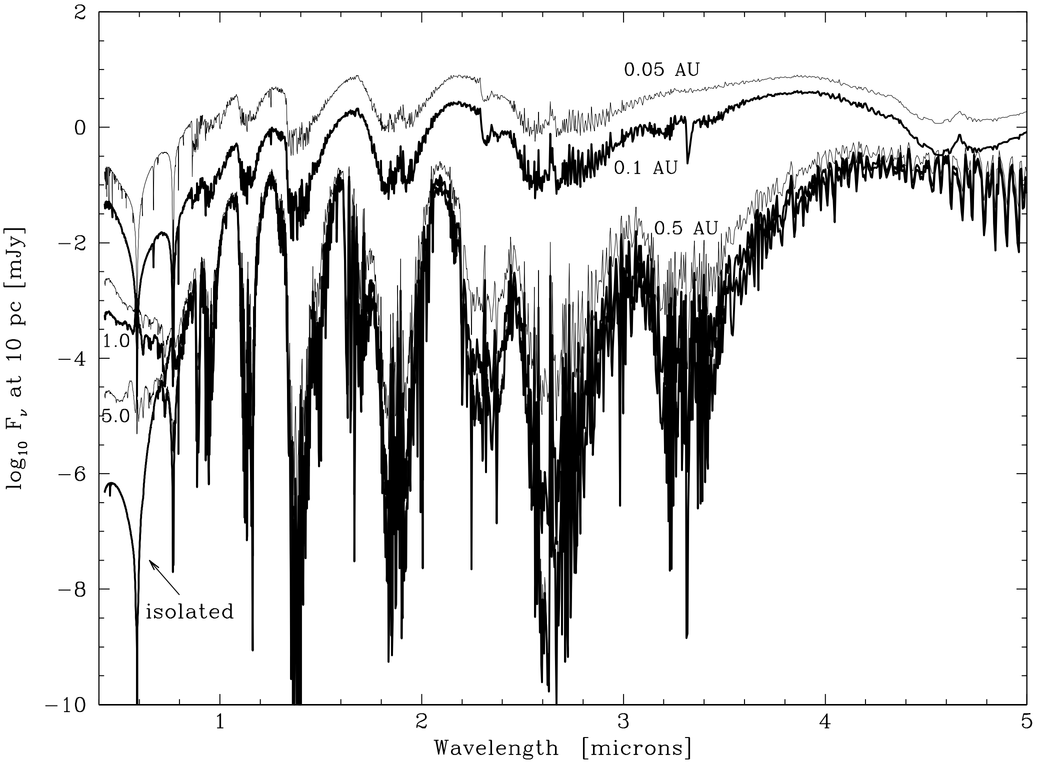

Fig. 14.— Same as Figure 13, but for an inner boundary flux characteristic of an effective temperature of 500 K. From top to bottom, the orbital distance is 0.05 AU, 0.1 AU, 0.5 AU, 1 AU, and 5 AU. The bottom curve is that for an isolated 500 K EGP/brown dwarf. In all cases, the gravity is 3×10^3 cm s^{-2}. Rayleigh scattering of the incident stellar radiation keeps the EGP emergent flux in the visible significantly above that of the isolated EGP/brown dwarf, but the high inner boundary flux causes the spectrum in the near and mid-infrared to be roughly independent of distance exterior to $\sim$0.5 AU. This sequence shows our approximate expectations for an irradiated brown dwarf and stands in marked contrast with Fig. 13.

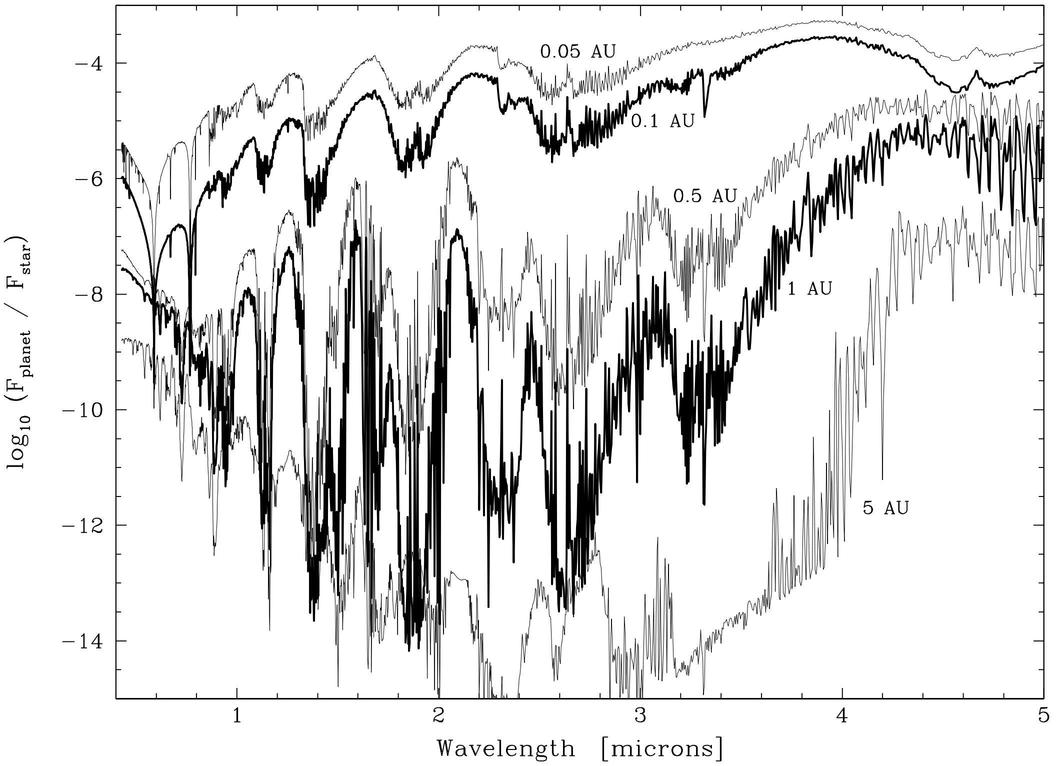

Fig. 15.— The phase-averaged planet-to-star flux contrast as a function of wavelength and orbital distance for the models portrayed in Figure 13. The inner boundary flux is characteristic of an effective temperature of 125 K, the planet models are cloud-free, and the primary star is of subtype G0V. From top to bottom, the orbital distance is 0.05 AU, 0.1 AU, 0.5 AU, 1 AU, and 5 AU. In all cases, the gravity is 3×10^3 cm s^{-2}. See text for details.

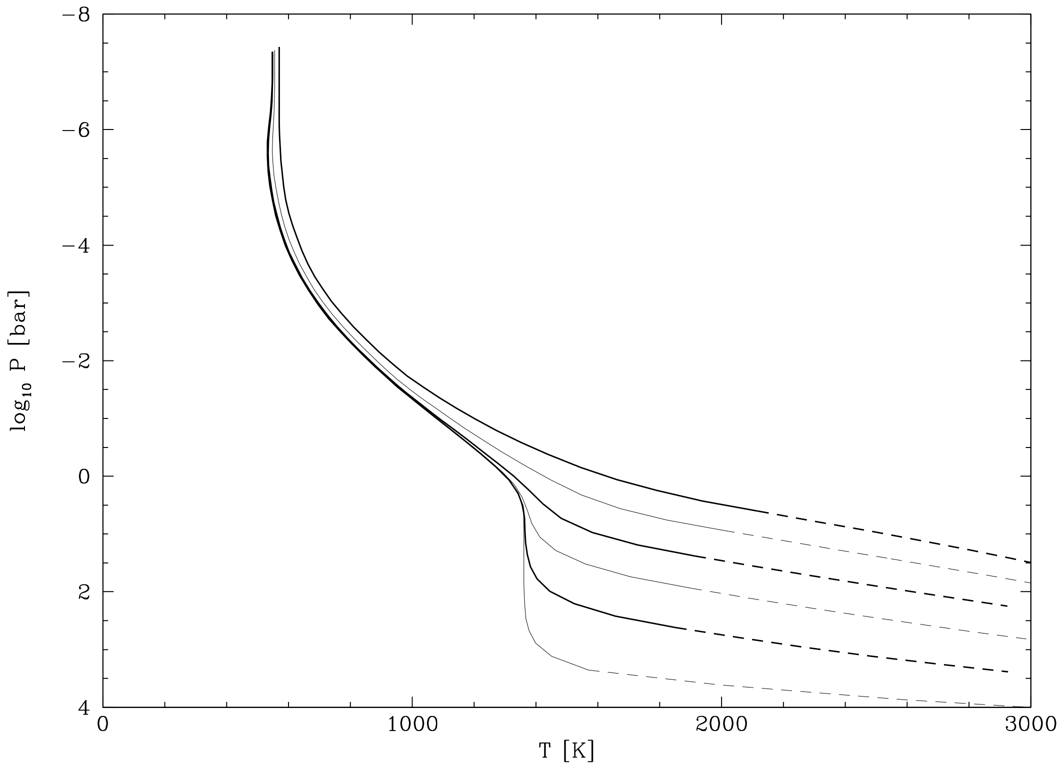

Fig. 16.— EGP T-P structure as a function of inner boundary flux. The inner boundary flux of a cloud-free Class IV model is varied. From the top profile to the bottom profile, models with inner boundary fluxes ($=\sigma T_{\rm eff}{}^4$) corresponding to $T_{\rm eff}=$ 1000 K, 750 K, 500 K, 300 K, 150 K, and 50 K are shown. (Note that we have alternated between thin and thick line types in order to facilitate a correspondence with the spectra in Figure 17.)

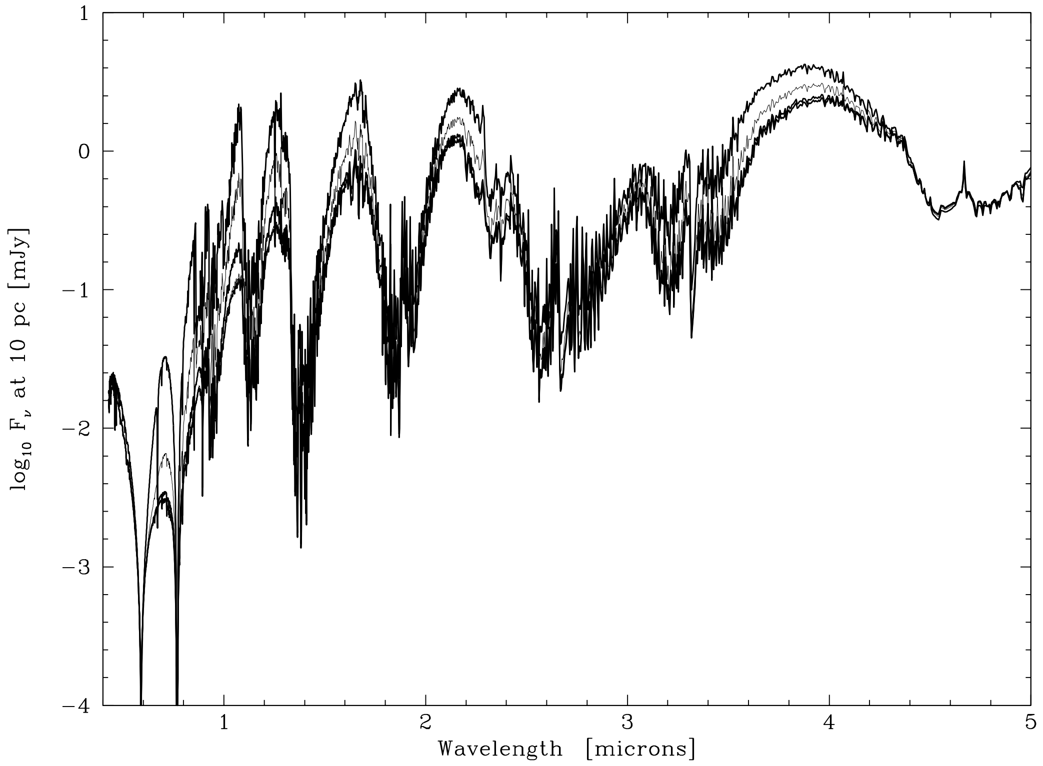

Fig. 17.— Class IV EGP emergent spectra as a function of inner boundary flux. Each spectral curve corresponds to each of the models depicted in Figure 16, from 1000 K (top curve) to 50 K (bottom curve, overlapping with that of 150 K and 300 K).

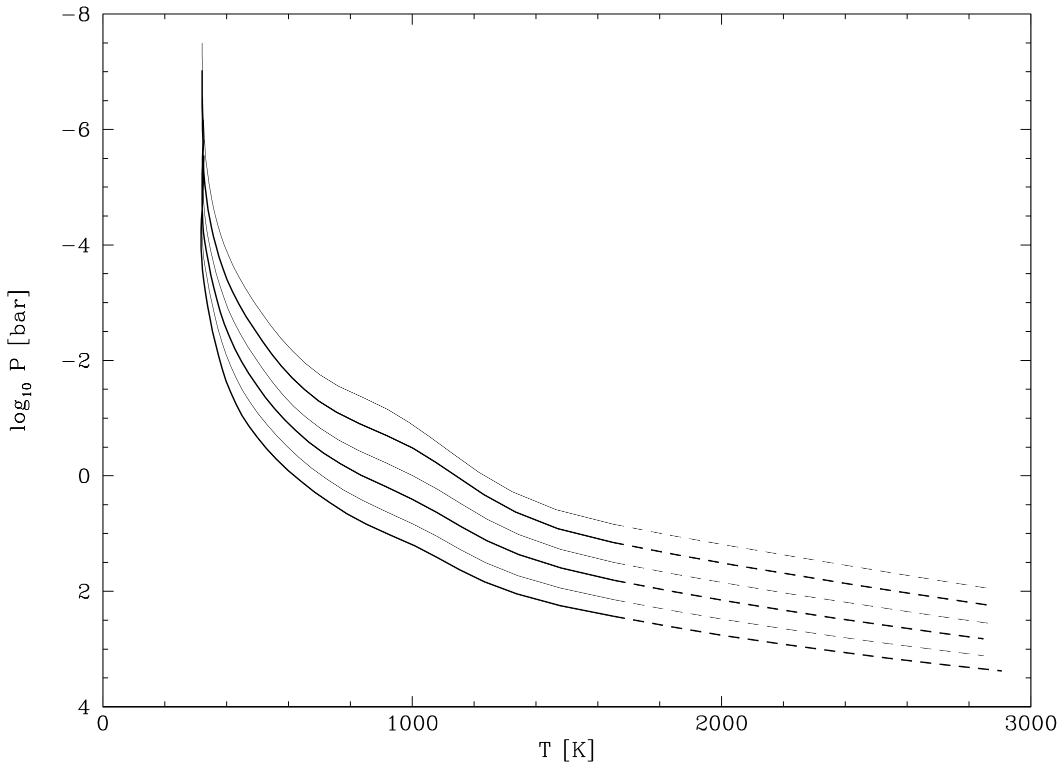

Fig. 18.— EGP T-P structure as a function of surface gravity. The surface gravity of a Class III model is varied from 10^3 cm s^{-2} (top curve) to 3×10^5 cm s^{-2} (a massive brown dwarf; bottom curve) in intervals of 1/2 dex. (Note that we have alternated between thin and thick line types in order to facilitate a correspondence with the spectra in Figure 19.)

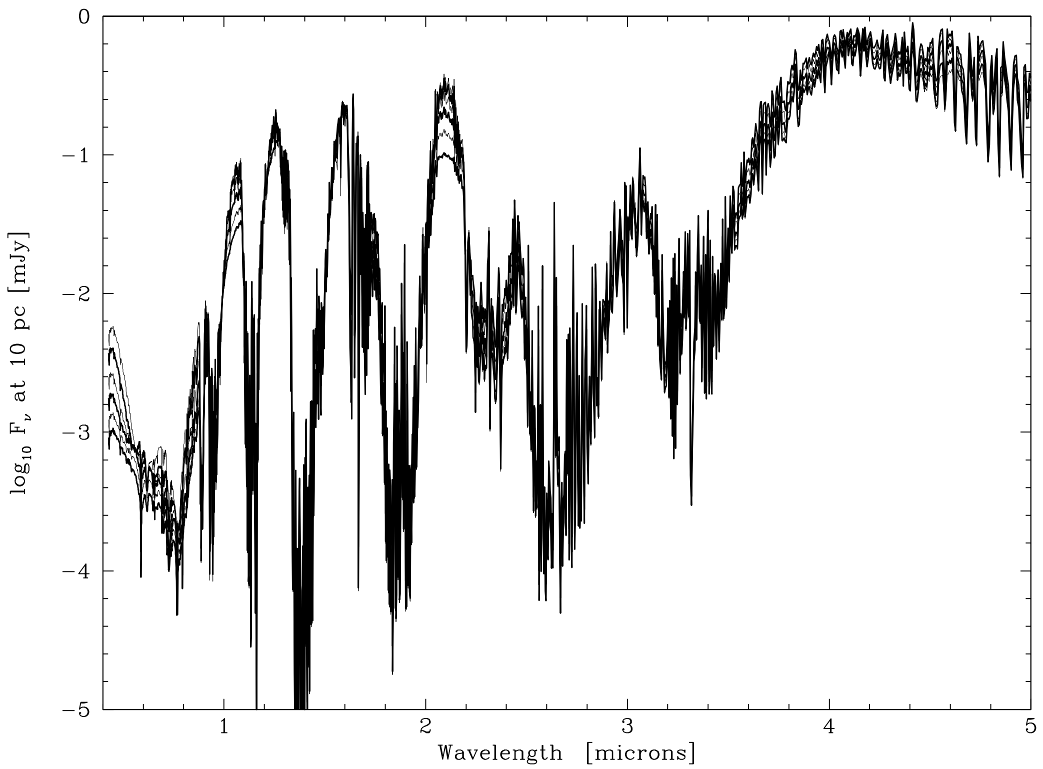

Fig. 19.— Class III EGP emergent spectra as a function of surface gravity. Each spectrum corresponds to each of the models depicted in Figure 18. For these models, an increase in gravity results in a general decrease in flux shortward of $\sim$2.2 μm, and an increase longward. Additionally, a larger gravity tends to reduce the peak-to-trough variations throughout the spectrum.

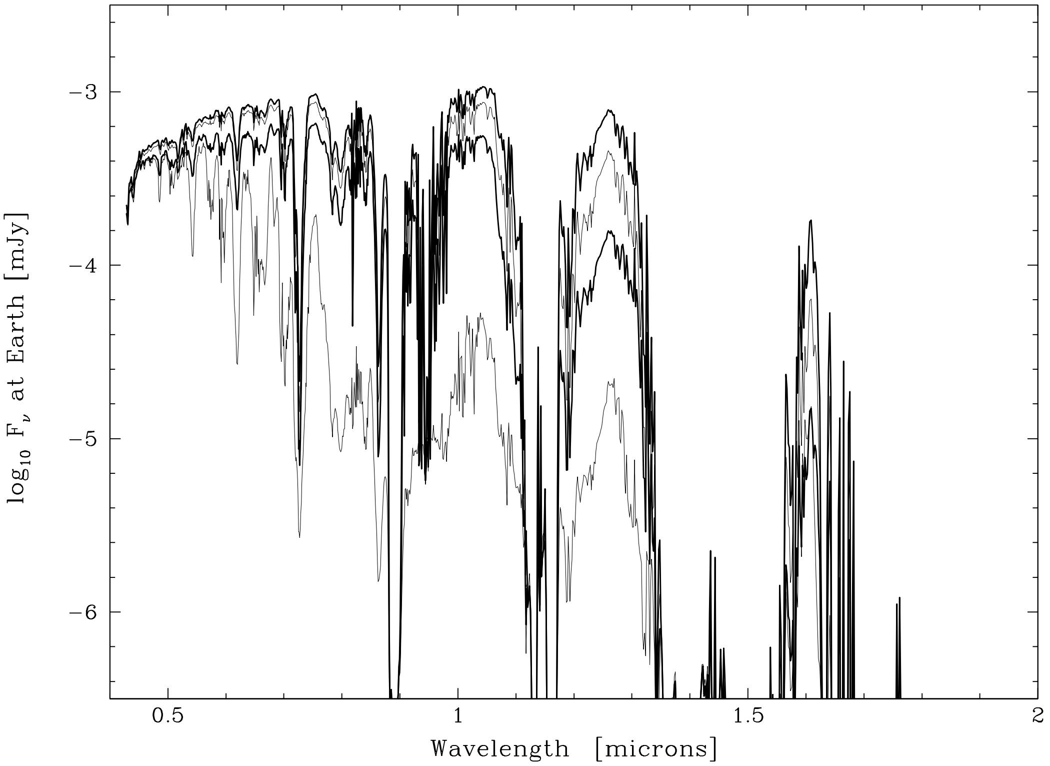

Fig. 20.— Effects of cloud particle size variation on the emergent spectrum of a Class II EGP, such as ϵ Eridani b. The resulting emergent spectra are shown for EGPs with three different median ice particle sizes, along with a cloud-free model of the same object. From top to bottom, the curves correspond to a size distribution peaked at 0.5 μm, one peaked at 5 μm, and another at 50 μm. In each case, 10% of the available H_2O was assumed to condense. The bottom curve is that of the cloud-free model.

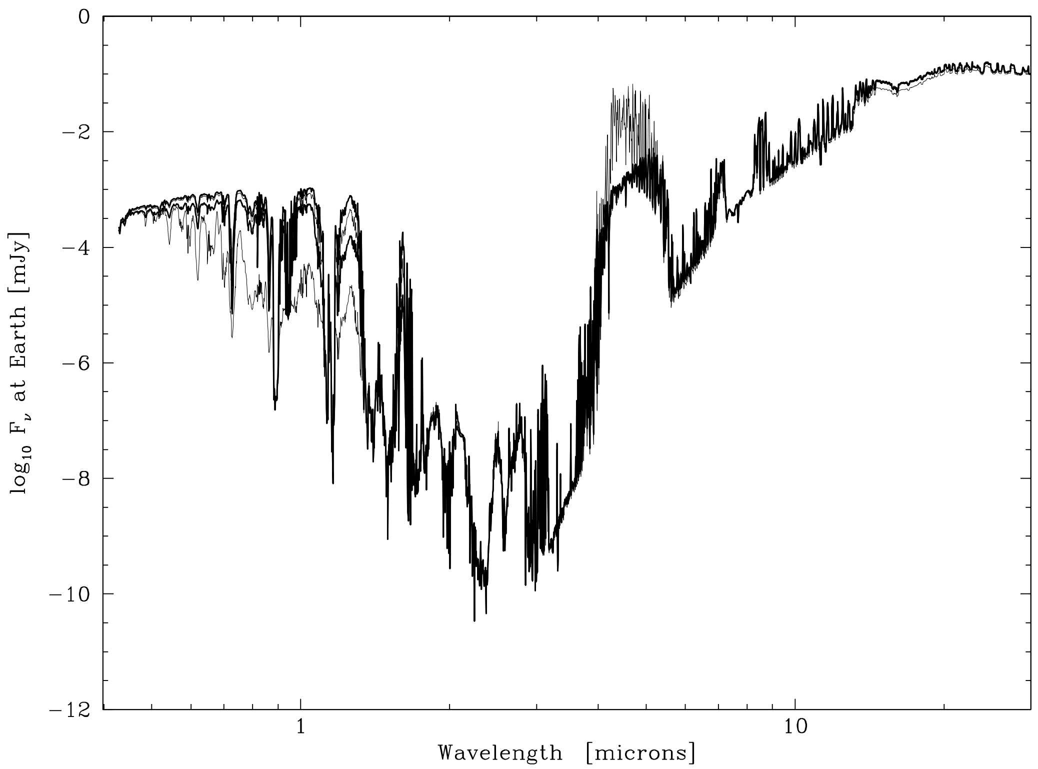

Fig. 21.— Effects of cloud particle size variation on the emergent spectrum of a Class II EGP, such as ϵ Eridani b, out to 30 μm. Models are the same as depicted in Figure 20. In the 4-5 micron opacity window, the cloud-free model flux is up to 2 orders of magnitude greater than those that include clouds of any particle size.

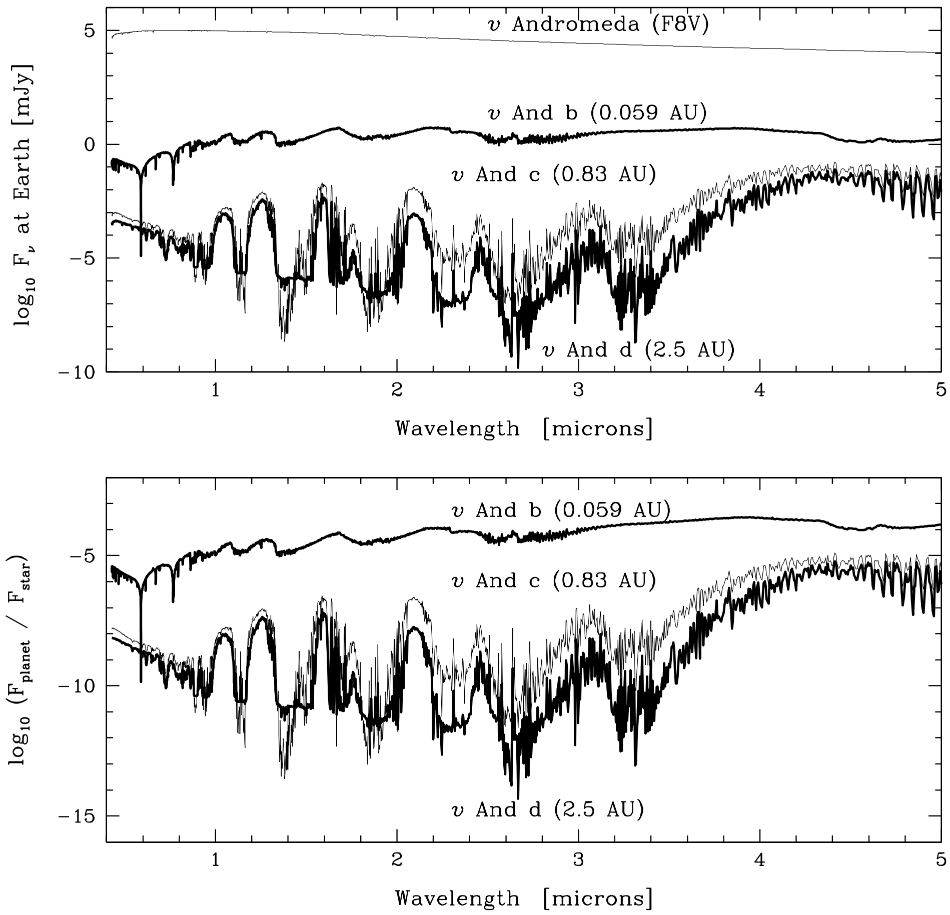

Fig. 22.— *Upper panel*: Visible and near-infrared spectra of υ And b, c, and d. An assumed spectrum of the primary (a scaled Kurucz model) is also depicted. υ And b, c, and d are Class V, III, and II EGPs, respectively. *Lower panel*: Wavelength-dependent, phase-averaged planet-to-star flux ratios for υ And b, c, and d.

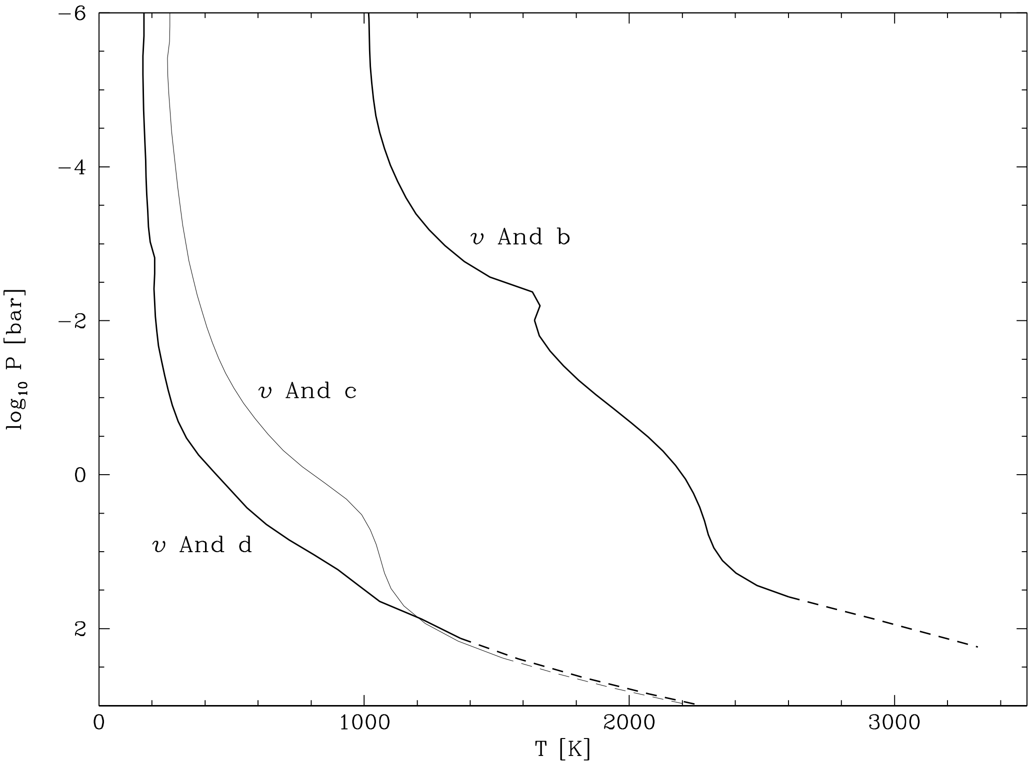

Fig. 23.— T-P profiles of υ And b, c, and d. The dashed portions of the profiles indicate convective regions.

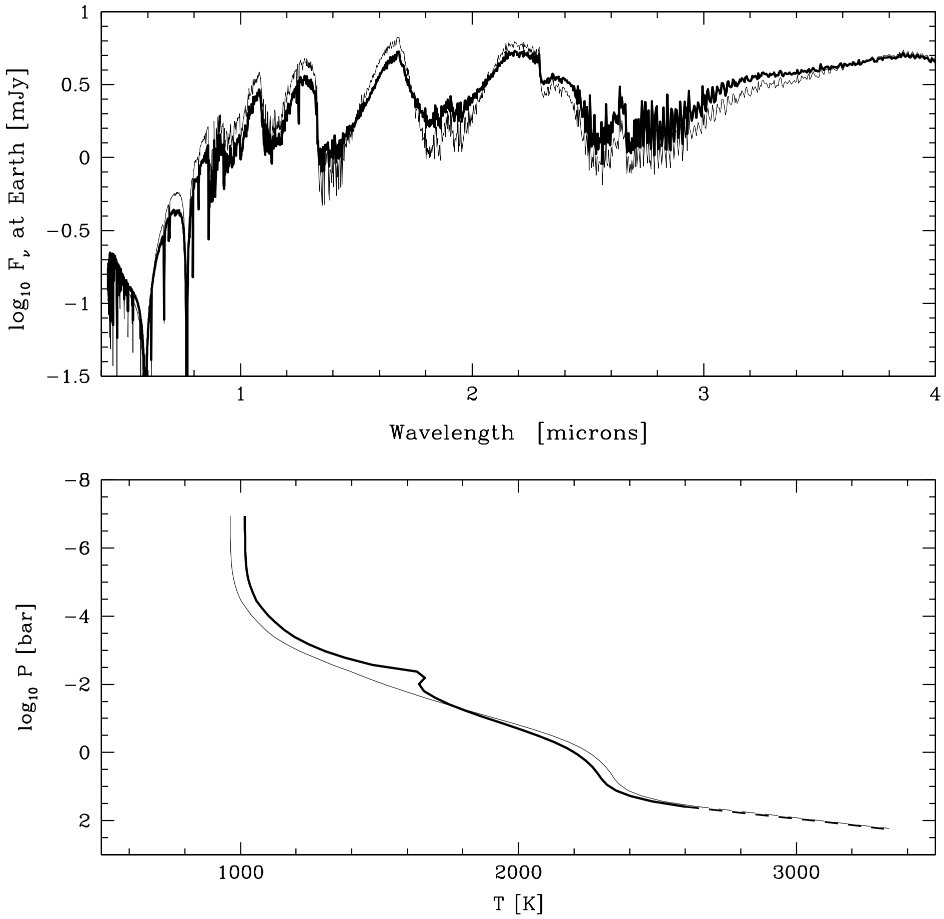

Fig. 24.— *Upper Panel*: Fiducial model spectrum of υ And b (thick curve) versus that of a cloud-free model (thin curve). The removal of the clouds results in a wider variation from peak to trough throughout most of the spectrum. *Lower panel*: Fiducial T-P profile of υ And b (thick curve) versus that of a cloud-free model (thin curve). Removing the iron and silicate clouds results in a cooler outer atmosphere, but a hotter deeper atmosphere. At large pressures ($\gtrsim$ 50 bars), the high clouds appear to have essentially no effect on the T-P profile.

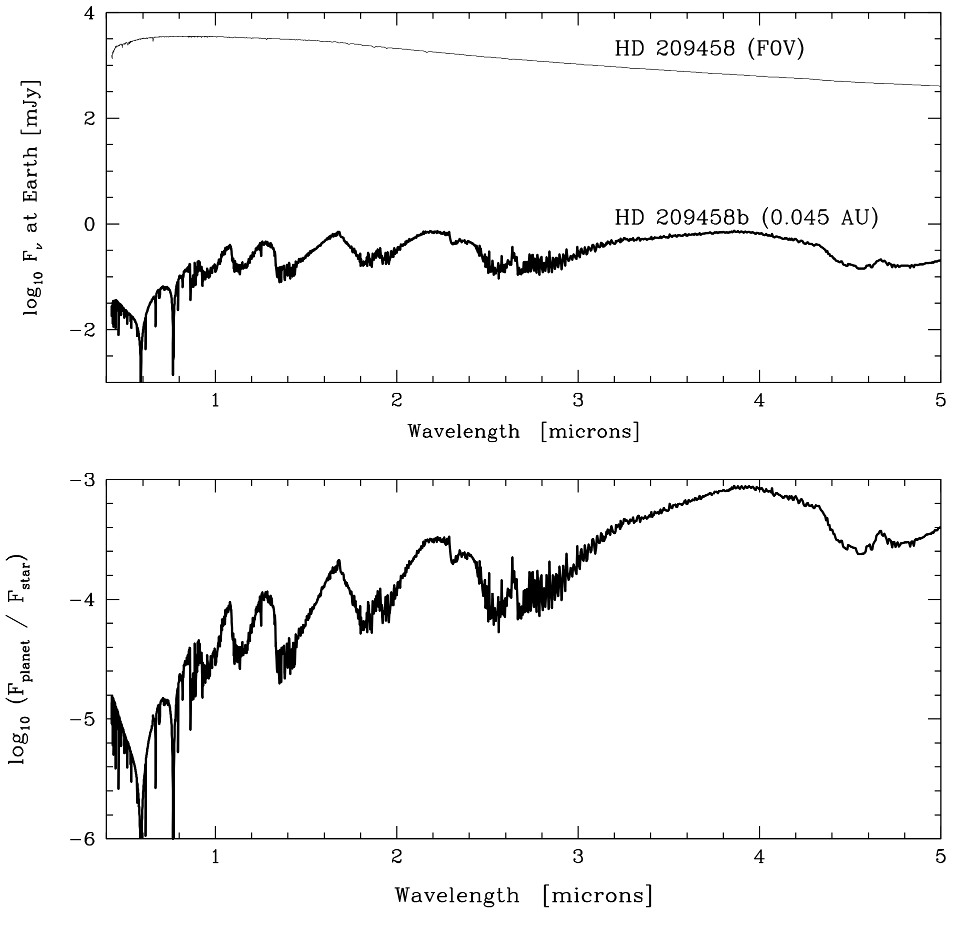

Fig. 25.— *Upper panel*: Visible and near-infrared spectrum of HD 209458b along with an assumed spectrum of its primary (a scaled Kurucz model). These fluxes were calculated using the planetary radius of 1.35 R_J. *Lower panel*: Wavelength-dependent, phase-averaged planet-to-star flux ratio of HD 209458b.

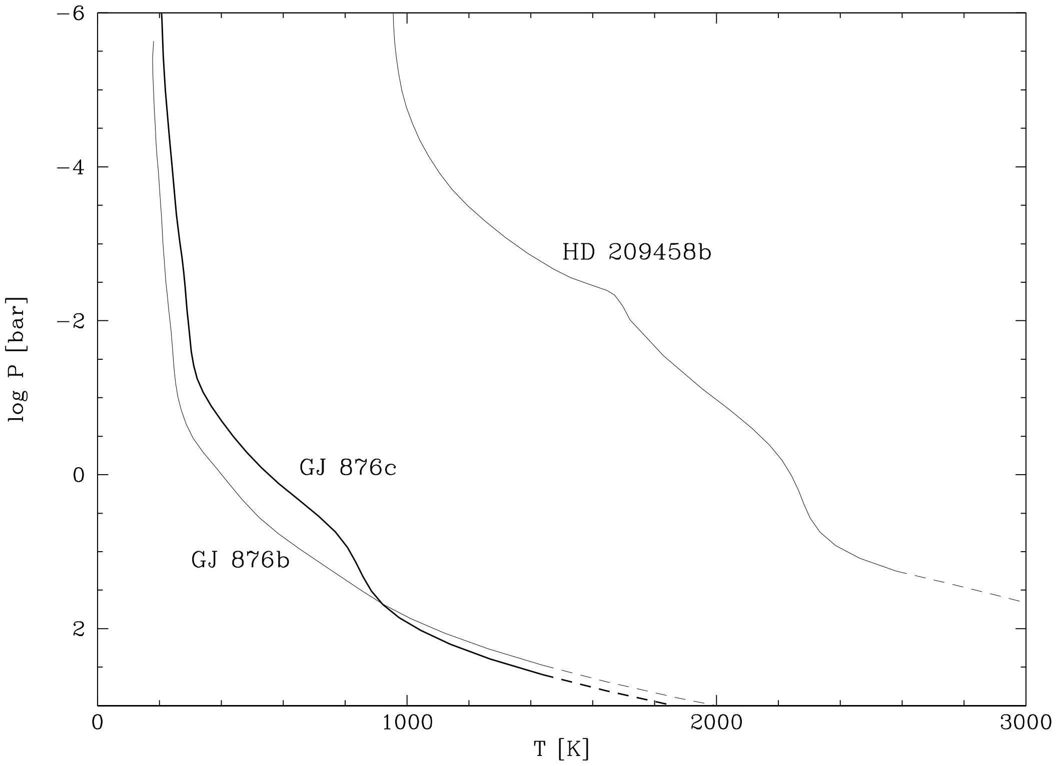

Fig. 26.— T-P profiles of HD 209458b, GJ 876b and GJ 876c. The dashed portions of the profiles indicate convective regions.

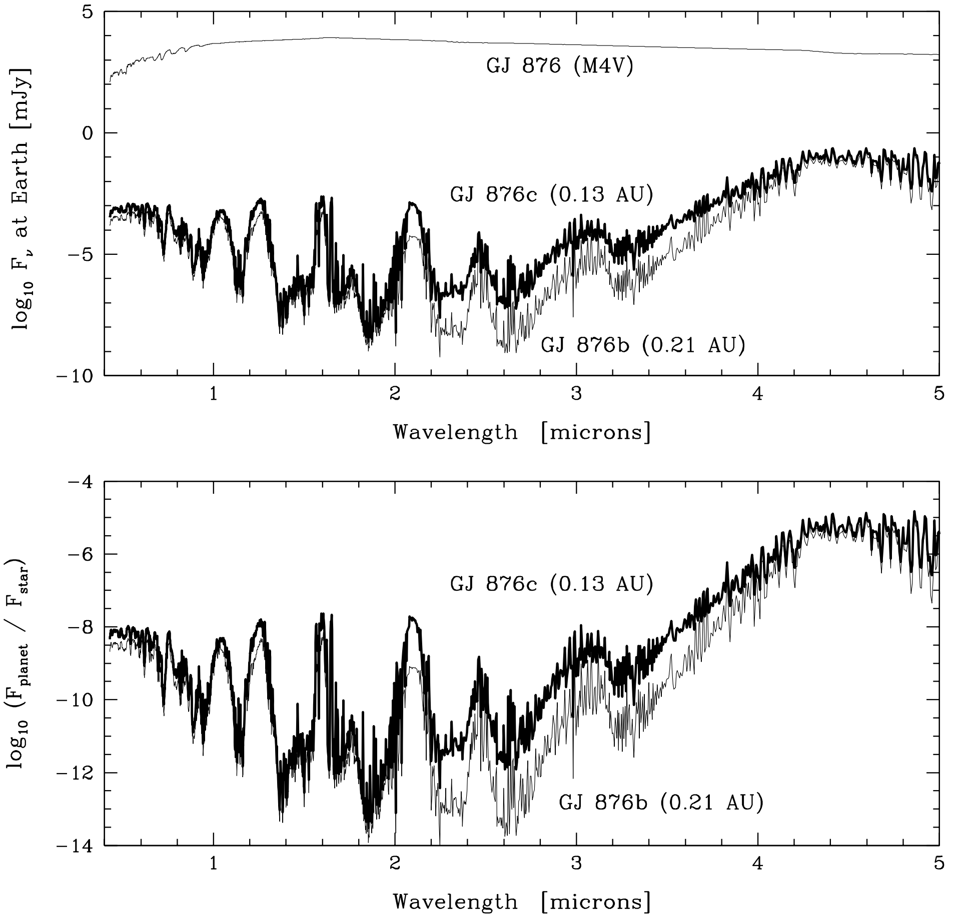

Fig. 27.— *Upper panel*: Visible and near-infrared spectra of GJ 876b and c. An assumed spectrum of the primary (a scaled Kurucz model) is also depicted. Both GJ 876b and c are Class III EGPs. *Lower panel*: Wavelength-dependent, phase-averaged planet-to-star flux ratios for GJ 876 b and c.

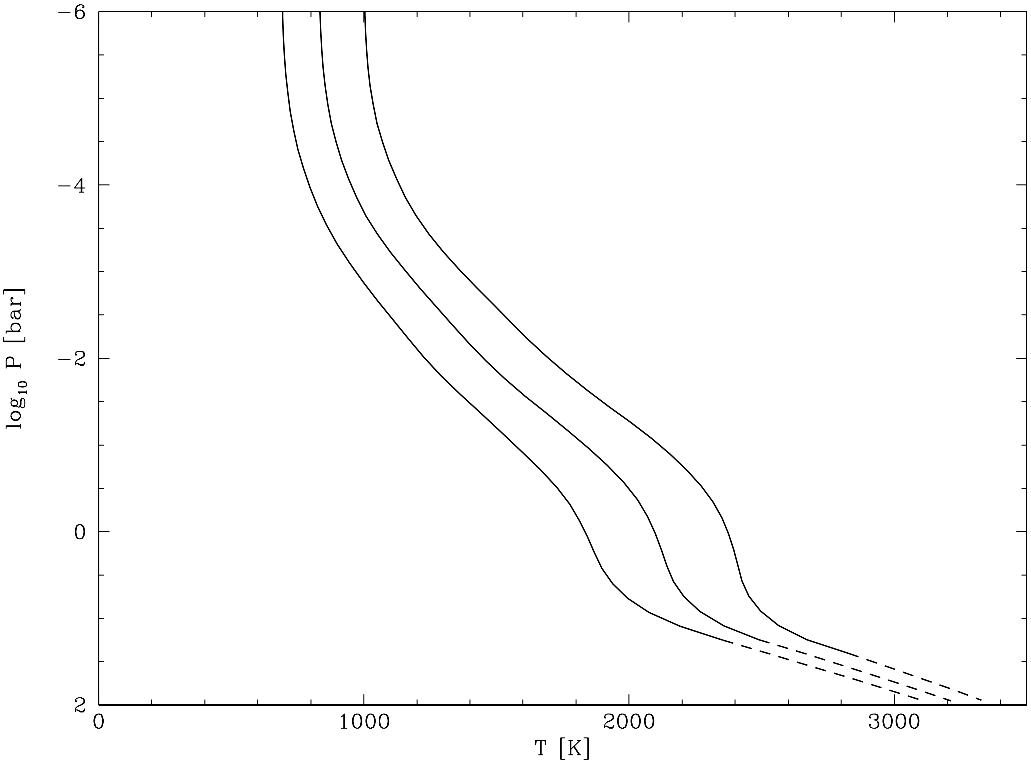

Fig. 28.— Cloud-free 51 Peg b T-P profiles with incident flux weighting of 1/4, 1/2, and 1. The coolest model shown has the flux weighting of 1/4. See text for details.

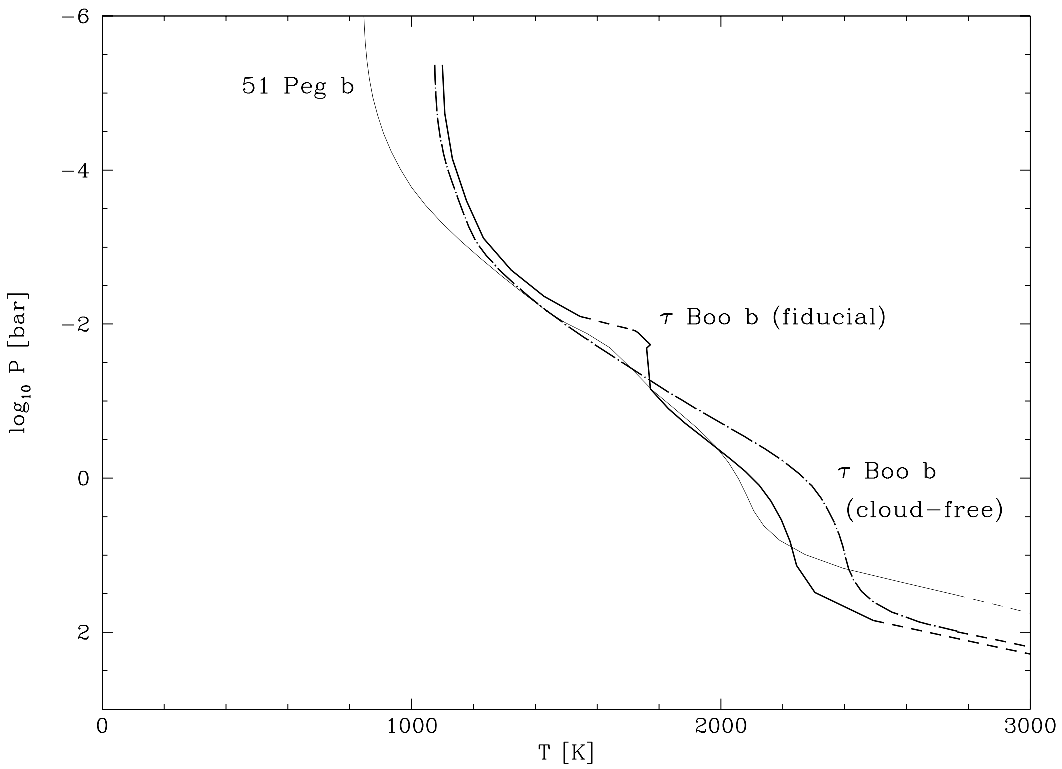

Fig. 29.— T-P profiles of τ Boo b and 51 Peg b. The dashed portions of the profiles indicate convective regions, and the fiducial model of τ Boo b is convective at low pressures, toward the top of the silicate cloud layer. Note that in order to achieve numerical convergence, the silicate and iron cloud layers of 51 Peg b have been attenuated to 10% of the elemental abundances of magnesium and iron, respectively.

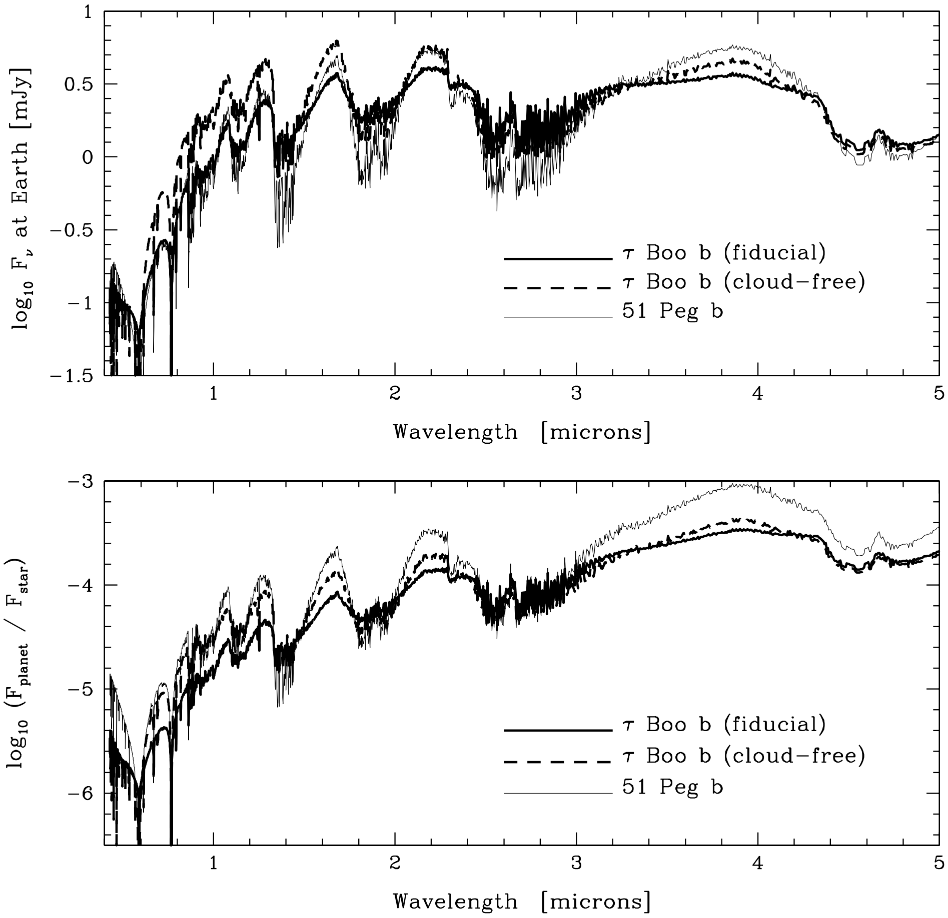

Fig. 30.— *Upper panel*: Visible and near-infrared spectra of τ Boo b and 51 Peg b. (Note that in order to achieve numerical convergence, the silicate and iron cloud layers of 51 Peg b have been attenuated to 10% of the elemental abundances of magnesium and iron, respectively, which may yield higher than actual fluxes in some spectral regions.) *Lower panel*: Wavelength-dependent planet-to-star flux ratios for τ Boo b and 51 Peg b.

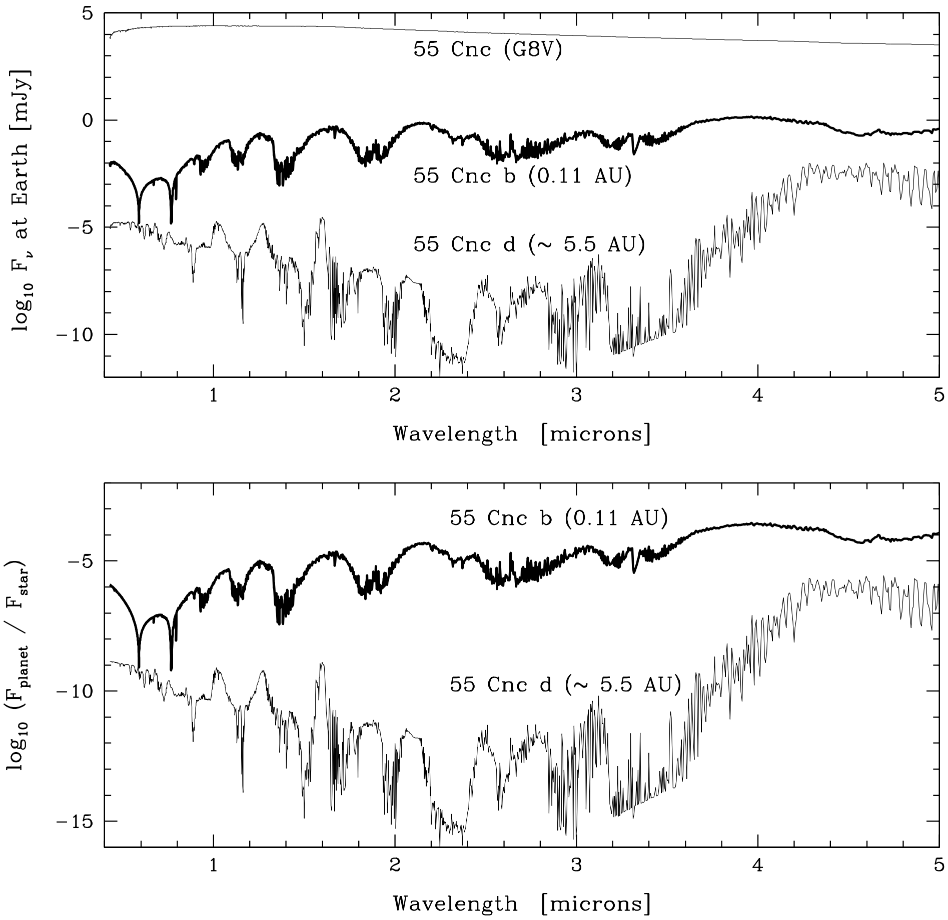

Fig. 31.— *Upper panel*: Visible and near-infrared spectra of 55 Cancri b and d from 0.4 to 5 μm. An assumed spectrum of the primary (a scaled Kurucz model) is also depicted. 55 Cnc b and d are Class IV and II EGPs, respectively. *Lower panel*: Wavelength-dependent, phase-averaged planet-to-star flux ratios for 55 Cnc b and d.

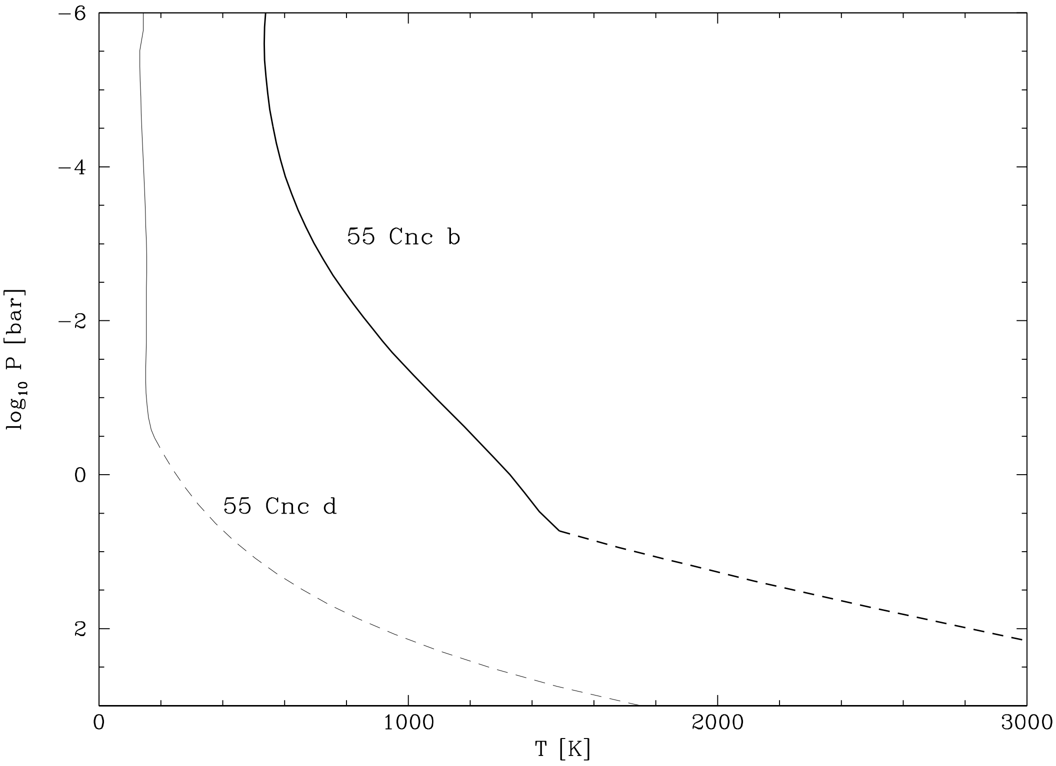

Fig. 32.— T-P profiles of 55 Cancri And b and d. The dashed portions of the profiles indicate convective regions.

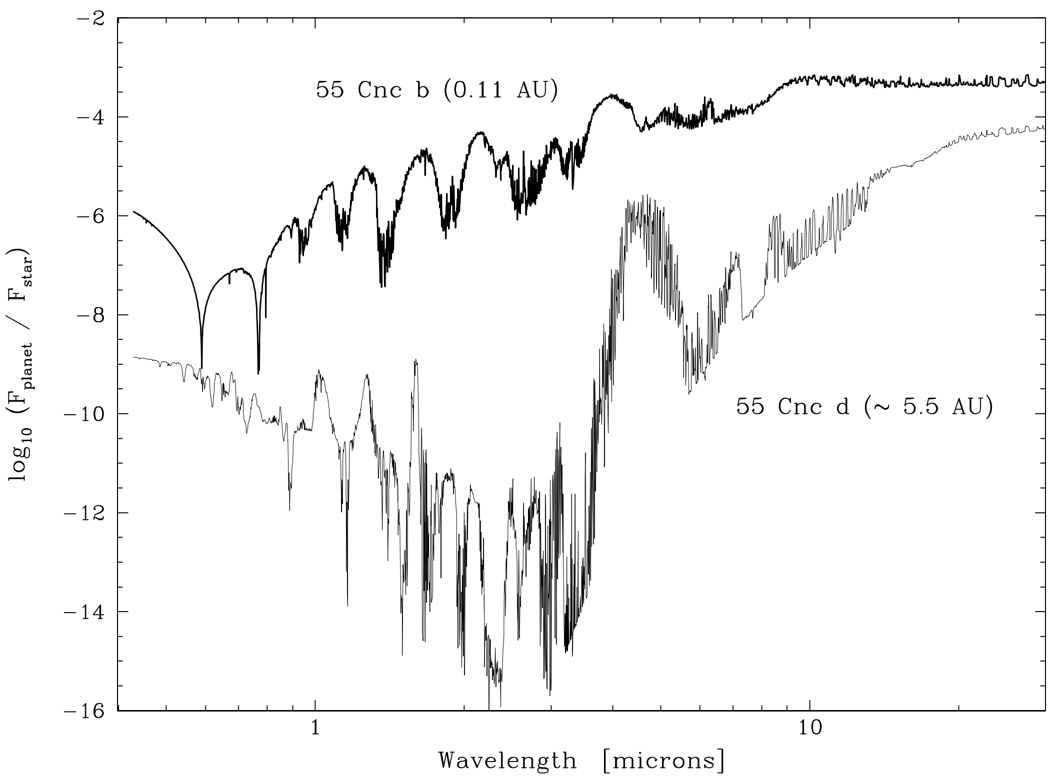

Fig. 33.— Wavelength-dependent, phase-averaged planet-to-star flux ratios for 55 Cnc b and d from 0.4 to 30 μm.

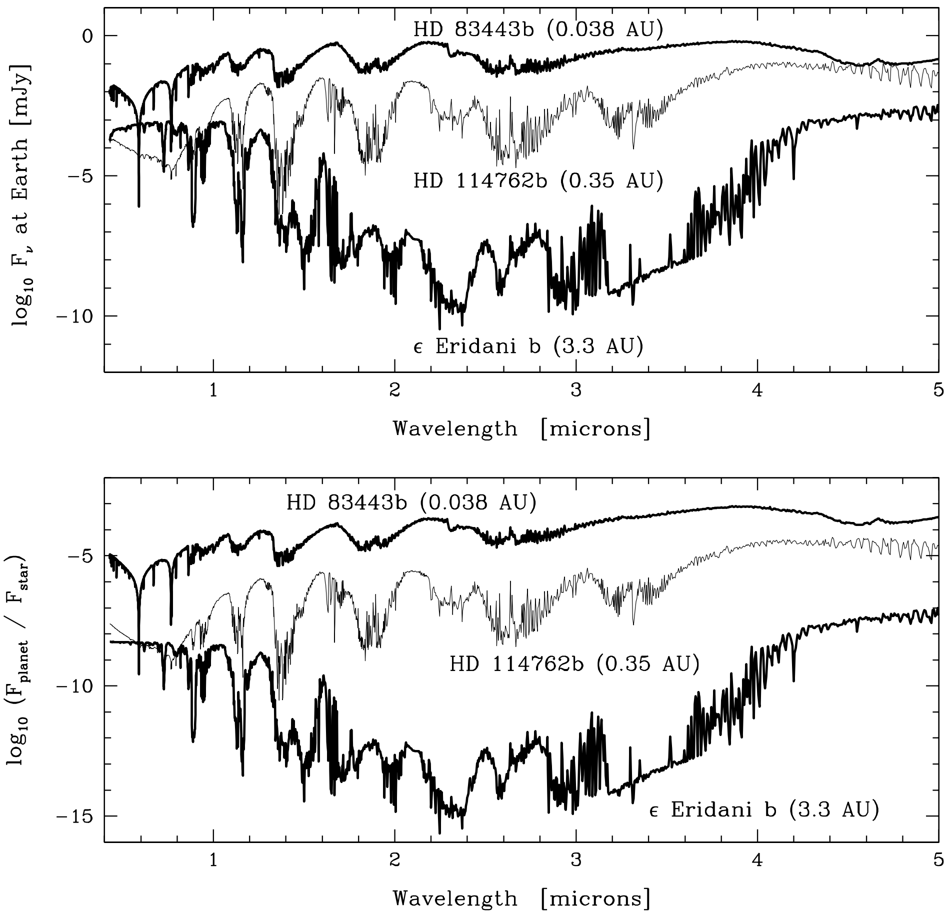

Fig. 34.— *Upper panel*: Visible and near-infrared spectra of HD 83443b, HD 114762b, and ϵ Eri b. These planets are Class V, III, and II EGPs, respectively. *Lower panel*: Wavelength-dependent planet-to-star flux ratios for HD 83443b, HD 114762b, and ϵ Eri b.

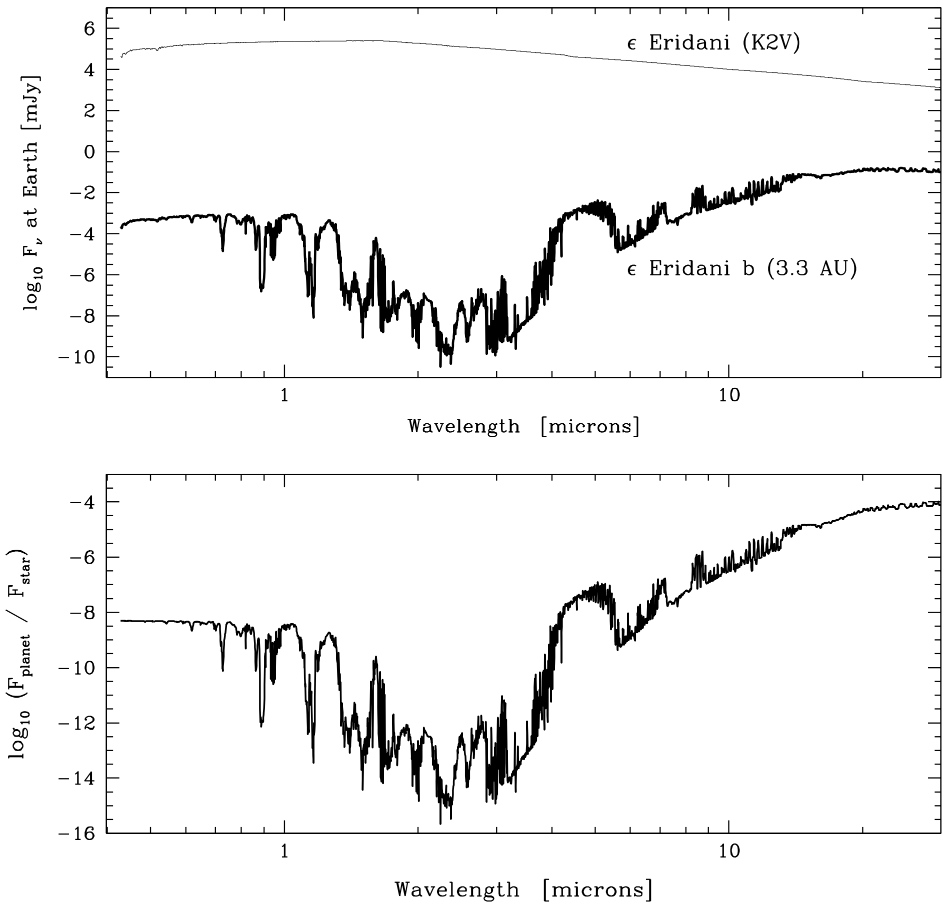

Fig. 35.— *Upper panel*: Model spectrum of ϵ Eri b from 0.4 to 30 μm. ϵ Eri b is a Class II EGP with a water cloud layer near a pressure of 1 bar. For this fiducial model, a cloud particle size distribution peaked at 5 μm is used, and 10% of the available H_2O is assumed to condense. *Lower panel*: Wavelength-dependent planet-to-star flux ratios for ϵ Eri b.

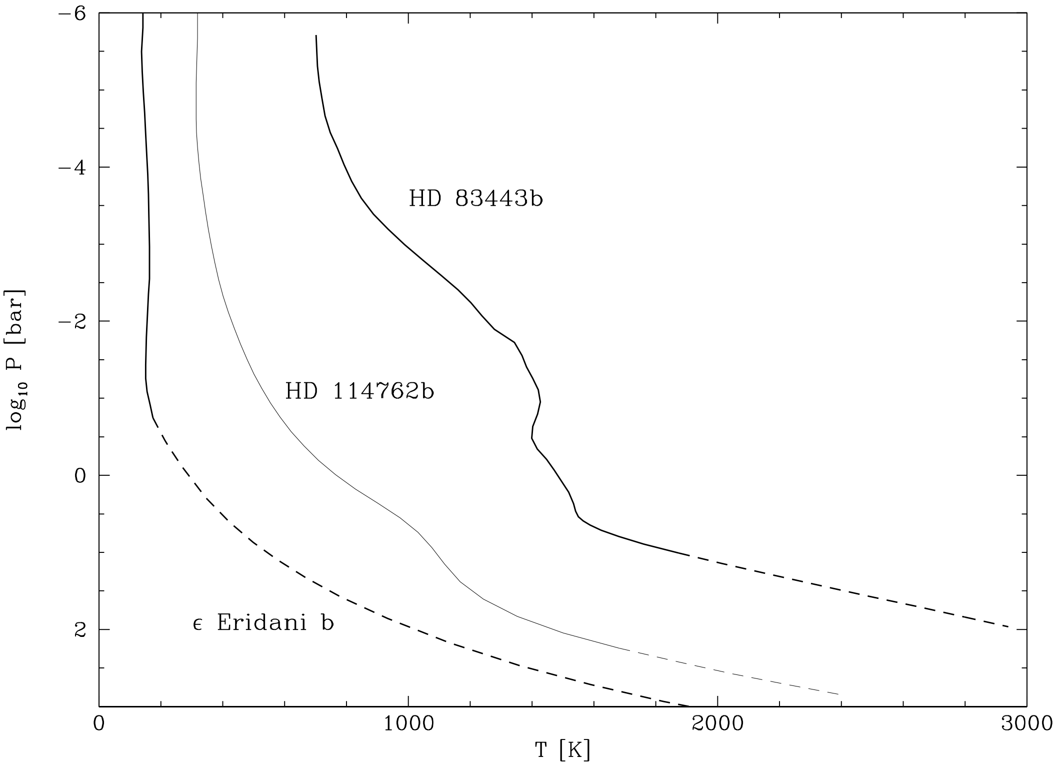

Fig. 36.— T-P profiles of HD 83443b, HD 114762b, and ϵ Eri b. The dashed portions of the profiles indicate convective regions.